ABSTRACT

Title: SOOT OXIDATION IN HYDROCARBON-FREE FLAMES

Haiqing Guo, Doctor of Philosophy, 2015

Directed by: Associate Professor Peter B. Sunderland

Department of Fire Protection Engineering

There are high uncertainties in the existing models of soot oxidation rates. To ameliorate this, soot oxidation in flames was examined using a novel ternary flame system, advanced diagnostics, and a detailed examination of past studies. The ternary flame system comprises a coflowing propylene/air diffusion flame to generate a steady soot column that flows into a hydrogen ring flame. The soot is thereby oxidized in a region far separated from soot formation, which is unlike any past study of soot oxidation in diffusion flames. Nonintrusive optical diagnostics were developed using a digital color camera to measure temperature and soot volume fraction. These diagnostics were validated using a steady laminar ethylene/air diffusion flame and were then applied to the

ternary flame. Also measured in the soot flame were velocity, soot primary particle diameter, and stable species concentrations along an axial distance of 45 mm. Temperatures were between 1500 to 1750 K, and O_2 partial pressures were between 10^{-2} to 10^{-1} bar. The soot flame was found to be lean, and its OH (with partial pressures between 10^{-4} to 10^{-3} bar) was expected to be equilibrated owing to the catalyzed radical recombination in the presence of soot. Soot flux and soot oxidation rates (0.5 to 6 g/m^2-s) were determined. Soot burnout was 90% at 55 mm height. New soot oxidation mechanisms for O_2 and OH were developed from a large body of published soot oxidation measurements. The resulting O_2 mechanism has an activation energy of 195 kJ/mol, and the OH mechanism has a collision efficiency of 0.10. Predictions using the new mechanisms are within ±80% of the present measurements in the ternary flame system.

SOOT OXIDATION IN HYDROCARBON-FREE FLAMES

by

Haiqing Guo

Dissertation submitted to the Faculty of the Graduate School of the
University of Maryland, College Park in partial fulfillment
of the requirements for the degree of
Doctor of Philosophy
2015

Advisory Committee:
Associate Professor Peter B. Sunderland, Chair
Associate Professor Christopher Cadou, Dean's representative
Assistant Professor Stanislav I. Stoliarov
Professor Arnaud Trouvé
Professor Michael Zachariah

Acknowledgements

This work was supported by the National Science Foundation. Research and Teaching Assistantship support was provided by the Department of Fire Protection Engineering.

First and foremost I'd like to thank my advisor, Professor Peter Sunderland, for his guidance and advice to help me to complete this work. It has been a pleasure to work with him and to learn from him. I would also like to thank my committee members, Dr. Christopher Cadou, Dr. Stanislav I. Stoliarov, Dr. Arnaud Trouvé, and Dr. Michael Zachariah for their invaluable suggestions.

I would like to specially thank my project partner Paul Anderson, for sharing the ideas and data during the past years. Paul is taking charge of the velocity and soot diameter characterization. I am deeply impressed by his passion and enthusiasm toward research and life. I would also like to thank all the other students and interns who have contributed to this project.

I would also like to thank all my friends in the department of fire protection engineering for their assistance and encouragement during my study. Special thanks to Ning Ren, Yinghui Zheng, Vivien Lecoustre, Yi Zhang, and Ajay Singh for their suggestions on this project.

Table of Contents

List of Tables

List of Figures

Nomenclature

Physical Constants

c	Speed of light in vacuum ($c = 3 \times 10^{8}$ m/s)
h	Planck constant ($h = 6.63 \times 10^{-34}$ J-s)
k	Boltzmann constant ($k = 1.38 \times 10^{-23}$ J/K)
R_u	Ideal gas constant ($R_u = 8.314$ J/mol-K)

Roman Symbols

a	Blackbody calibration constant
A	Pre-exponential factor
A_b	Abel transform operator
A_D	Combined optical constants
A_l	Area of lens aperture
B	Blackbody spectral radiance
C	Bandpass filter optical constant
d_p	Soot primary particle diameter
D_k	Blackbody aperture diameter
D_i	Diameter of image
e	Incident energy passing through camera lens
E	Total power from the blackbody aperture
E_A	Activation energy
$E(m)$	Refractive index absorption function
f	Probability function

f_s	Soot volume fraction
F	Local property in deconvolution
F_S	Integrated soot volume fraction
GS	Normalized grayscale
I	Irradiance incident on sensor
k_A	Kinetic constant for surface A
k_B	Kinetic constant for surface B
k_T	Kinetic constant for temperature
k_z	Kinetic constant for O_2 partial pressure
K	Reaction equilibrium constant
K_{abs}	Coefficient of absorption
K_c	Camera coefficient of detection
K_{ext}	Coefficient of extinction
l_f	Focal distance
l_i	Image distance
l_o	Object distance
L	Lower integration limit boundary
m	Refractive index
$\dot{m}_s$	Soot mass flux
m_c	Mass of carbon removed per collision
MW	Molecular weight
n_p	Soot primary particle number density
p	Pressure

P Projected property in deconvolution

r Radial coordinate

R Soot column radius

s Onion peeling reconstruction matrix

S Soot surface area per unit volume

$\bar{S}$ Total soot surface area

t Time

T Temperature

u Flame axial velocity

$\bar{u}$ Mean molecular velocity

$\dot{w}_{ox}$ Soot oxidation rate

W Soot spectral radiance

x Horizontal coordinate in the object plane

y Horizontal coordinate perpendicular to the object plane

Greek Symbols

ε Soot emissivity

ζ Radial location between two adjacent rings

η Collision efficiency

λ Wavelength

ρ Gas density

ρ_s Soot density

τ Bandpass filter transmittance

χ	Fraction of surface
Φ	Local equivalence ratio
α	Dispersion coefficient
σ	Soot diameter standard deviation
ξ	Camera lens optical constant

Chapter 1: Introduction

Soot is impure carbon particles resulting from the incomplete combustion from coal burning, internal combustion engines, boilers, furnaces, etc. Soot is a major contributor to climate change. It is also hazardous to people due to its association with respiratory disease and cancer. Soot in engines, especially in diesel engines, increases radiative loading, impedes oil flow, abrades oil rings, increases engine wear, and in many cases must be removed from the exhaust stream. Soot in unwanted fires increases radiation, fire spread rates, and carbon monoxide emissions. Unfortunately, soot remains one of the least understood subjects in combustion. There are particularly large gaps in understanding soot oxidation processes. This chapter introduces the motivation for this project, reviews the previous work, and presents the objectives for this study.

1.1. Motivation

There are several detailed numerical models [1-7] of soot formation and oxidation in flames. Soot surface oxidation is generally attributed mostly to attack by molecular O_2 and OH radicals. These generally have been validated with experiments in laminar flames. Kazakov et al. [2] considered four ethylene/air laminar premixed flames and compared the predicted soot volume fractions with the experimental results. The shape of the experimental soot volume fractions for all of the flames generally agrees with the results predicted by the model. However, the agreement deteriorates in leaner flames where the soot oxidation in the post-flame zone is not well predicted. Appel et al. [3] examined nine laminar premixed flames of different fuels. Their model predictions agreed with the

experimentals generally within a factor of 3. Mehta et al. [5] compared the predictions of 36 detailed models of gas and soot kinetics with measurements from eight laminar premixed and diffusion flames. Interactions between soot particles and gas species (nucleation, surface growth and oxidation) and interactions between soot particles (coagulation and aggregation) were considered. They found that no model predicted the soot volume fraction within a factor of 5 from experimental values for all eight flames.

An improved understanding of soot oxidation kinetics might also contribute to an improved understanding of soot formation models due to the competing mechanism between soot oxidation and soot formation in flames. In addition, it is not only important for understanding combustion of hydrocarbons (such as natural gas, diesel, jet fuel, and biofuels), but also for understanding coal combustion owing to chemical similarities between soot and coal.

1.2. Background

Past work in soot oxidation studies is summarized in the reviews of Howard [8], Kennedy [9], and Stanmore et al. [10]. Molecular oxygen (O_2) and hydroxyl radical (OH) are believed to be the main soot oxidants in most flames. The current leading soot oxidation mechanisms were by Nagle and Strickland-Constable (NSC) [11] for O_2 mechanism and by Neoh et al. [12-14] for OH mechanism. Other possible soot oxidizers in flames include: oxygen atom (O), carbon dioxide (CO_2), and water (H_2O). It is generally agreed that in flames, the soot particle diameter is so small (20 – 50 nm in diameter) that the oxidation mechanism is not limited by diffusion of gases [12].

Therefore, soot oxidation can be interpreted as controlled by the heterogeneous chemical reaction at the particle surface. The soot oxidation reactions most commonly considered are as follows:

$$C_{soot} + O_2 \rightarrow 2CO + \text{products}, \tag{1-1}$$

$$C_{soot} + OH \rightarrow CO + \text{products}, \tag{1-2}$$

$$C_{soot} + O \rightarrow CO + \text{products}, \tag{1-3}$$

$$C_{soot} + CO_2 \rightarrow 2CO + \text{products}, \tag{1-4}$$

$$C_{soot} + H_2O \rightarrow CO + \text{products}. \tag{1-5}$$

For O_2, Nagle and Strickland-Constable [11] considered the oxidation of various forms of carbon rods at temperatures of 1000 – 2000 ℃ and at O_2 partial pressures of 0.1 – 0.6 bar. The oxidation rate was determined by measuring the carbon surface position as carbon was removed by the high velocity oxidizer. However, the experiment bore little resemblance to soot oxidation in flames, and yielded no information on oxidants other than O_2.

The NSC [11] correlation formula is:

$$\dot{w}_{ox} = 1.2 \times 10^5 \left[\left(\frac{k_A p_{O_2}}{1 + k_z p_{O_2}} \right) \chi + k_B p_{O_2} (1 - \chi) \right], \tag{1-6}$$

where $\chi = \left[1 + k_T / \left(k_B p_{O_2} \right) \right]^{-1}$, is fraction of surface covered by site A, k_A, k_B, k_T, and k_z are all well adopted kinetic constants to fit the experiments. p_{O2} is the oxygen partial pressure in bar, T is temperature in Kelvin, and $\dot{w}_{ox}$ is soot oxidation rate in g/m^2-s.

$k_A = 2\times10^5 \exp(-15100/T)$, (g/m^2-s-bar)

$k_B = 44.6\exp(-7640/T)$, (g/m^2-s-bar)

$k_T = 1.51\times10^9 \exp(-48800/T)$, (g/m^2-s)

$k_z = 21.3\exp(2060/T)$, (1/bar)

The NSC expression is often misleading because the oxidation rate is expressed in g-atoms carbon/m^2-s, which equals to 12 g/m^2-s. This confusion led to the mistakes in the works of Puri et al. [15, 16], and of Echavarria et al. [17].

Park et al. [18] measured soot oxidation rates in shock tubes. They found these to agree with the NSC expression at temperatures between 1500 – 2000 K, and therefore advocated the implementation of NSC expression in the soot oxidation study. However, the NSC expression tends to underpredict the oxidation rates at temperatures between 2000 – 4000 K. The test times are short and the temperatures are significantly higher than in typical flames.

Another widely used correlation for O_2 oxidation is that of Lee et al. [19]. They measured soot oxidation rates in diffusion flames and obtained Arrhenius rate expressions with first-order O_2 dependence. Soot oxidation was observed in the lean regions of a gas jet diffusion flame. Unfortunately, O_2 was considered as the only oxidizer. Only a limited range of O_2 partial pressure (0.05 – 0.1 bar) was explored. In addition, possible soot formation in the post flame region was not discussed.

The Lee correlation is:

$$\dot{w}_{ox} = 1.085 \times 10^{8} \frac{p_{O_2}}{T^{1/2}} \exp\left(-\frac{19780}{T}\right), \tag{1-7}$$

where p_{O2}, T, and $\dot{w}_{ox}$ were defined in the NSC expression.

Chan et al. [20] used a similar experiment setup and studied the soot oxidation due to O_2 in the post flame region; and in the thermogravimetric analysis (TGA) condition. Their measured soot oxidation rates are in reasonable agreement with those obtained by other workers [19].

Higgins et al. [21] studied the oxidation of soot by O_2 at temperatures between 1100 – 1400 K in a flow reactor. Soot from a hydrocarbon diffusion flame passed into a flow reactor, where the soot mobility diameters at the inlet and the exit of the reactor were measured with a differential mobility analyzer (DMA). Constant number density of the soot particles had to be assumed for calculating of the oxidation rate.

Wang and coworkers [22] used a similar experimental setup to study the oxidation of nascent soot by O_2 at about 1000 K for O_2 concentrations of 0.1 – 0.8%. The measured oxidation rates were an order of magnitude larger than those predicted by the correlation of Ref. [11], suggesting a more reactive surface of nascent soot than graphite or graphitized soot. The same authors pointed out that nascent soot are liquid-like and far from carbonized [23].

Soot oxidation has also been studied with thermogravimetric analysis (TGA) [24-29]. In Ref. [24], soot was collected from a hydrocarbon flame with a stabilization plate and was crushed into a powder. The powder was then delivered to a high-pressure TGA.

The pressure effect on soot porosity was analyzed with a high-resolution TEM. Soot surface area during the test was not measured; and the porosity effect on the soot surface area was not discussed. Unfortunately, TGA provides a test environment very different from that of real flames. The temperatures had a limited range between 700 – 1000 K. The O_2 concentrations varied between 10 – 21%.

For OH, Fenimore and Jones [30] considered a two-stage burner where the soot-laden combustion gases from the first stage were mixed with air and burned in the second stage. They postulated that their flames possessed an additional mechanism besides oxidation by O_2; and advocated the importance of OH in soot oxidation. They measure an OH collision efficiency of 0.1.

Neoh et al. [12-14] considered a similar experimental setup but used different equivalence ratios. OH was found to be the primary oxidizer. Soot oxidation by O_2, as predicted by the mechanism of NSC [11], had to be subtracted from the measured oxidation rate. The flame was assumed to be one dimensional. Unfortunately, soot deposition prevented the observation of long-term steady flames. Soot oxidation was only measured across a height of 5 mm, requiring high spatial resolution. Flame velocities were not measured. They found an OH collision efficiency of 0.28 when soot diameter was determined from optical scattering, or 0.13 when soot diameter was determined with transmission electron microscopy (TEM).

In contrast to Lee's [19] expression for soot oxidation by O_2, Neoh et al. [12] assumed the activation energy of OH is negligible. Their OH soot oxidation expression is:

$$\dot{w}_{ox} = 1.29 \times 10^6 \eta_{OH} \frac{p_{OH}}{T^{1/2}}, \quad (1\text{-}8)$$

where η_{OH} is the OH collision efficiency, and p_{OH} is the partial pressure of OH in bar.

Neoh et al. also examined possible internal burnings due to O_2 and OH from the calculated effectiveness factor. Their results suggest that soot might be subject to some O_2 internal burning due to its lower reactivity. However, this calculation is based on the Thiele modulus from the burning of coal chars, which have diameters at least one order of magnitude higher than those of soot. Its accuracy is also affected by the reaction kinetics which is not sufficiently understood.

Echavarria et al. [17, 31] used a similar setup for studies of soot oxidation and fragmentation. The breakup of the bridges connecting primary particles, and the presence of fragments were observed with a high-resolution TEM. Besides calculating the effectiveness factors similar to Neoh et al. [12], Echavarria et al. [31] also observed nearly 50% increase in soot surface area (m^2/g soot) during oxidation. They attribute this increase in surface area to internal burning. However, a decrease in soot primary particle diameter due to surface reaction, particle fragmentation, reduced bridging, or an increase in surface roughness could all lead to the surface area increase per unit soot mass, and their contributions were not discussed.

For O atom, Rosner et al. [32] compared the oxidation of pyrolytic and isotropic graphite by O and O_2 at high temperatures. Wright et al. [33] studied the soot oxidation due to O attack at the gravimetric condition with temperatures between 300 – 900 K. They reported O atom collision efficiency with soot of 0.036, at temperature of 825 K

and O partial pressure of 3.3 $\times 10^{-5}$ bar. In typical flames, O concentrations are typically more than an order of magnitude lower than those of OH [33, 34]. Thus in most flames oxidation by O atom is negligible compared with that of OH and O_2.

Tesner et al. [35] studied soot oxidation by CO_2 in a laminar diffusion flame. For temperatures between 1800 – 1940 K, they obtained the oxidation expression due to CO_2 as follows:

$$\dot{w}_{ox} = 1.15 \times 10^{9}\, p_{CO_2} \exp\left(-\frac{37745}{T}\right), \tag{1-9}$$

where p_{CO2} is the partial pressure of CO_2 in bar. This activation energy is much higher than the activation energy obtained from Lee et al. [19] for O_2 oxidation. In typical flames the resulting oxidation rate due to CO_2 attack is negligible [12].

Similarly, the reaction between carbon and H_2O has been discussed in Refs. [36, 37]. Although there is considerable H_2O in most flames, its contribution to soot oxidation is generally negligible [38].

Soot oxidation was also studied in hydrocarbon diffusion flames [15, 16, 34, 39-41]. They compared their measured oxidation rates with the predictions using the expression of NSC [11] for O_2 and of Neoh et al. [12] for OH. Garo et al. [39] used a methane diffusion flame and were only able to observe soot oxidation within a height of 5 mm. Puri et al. [15, 16] observed the soot oxidation in methane, methane/butane, and methane/butene flames. Soot oxidation was also subsequently observed in a variety of hydrocarbon diffusion flames at pressures from 0.1 – 8.0 bar [34, 40, 41]. Similar to Lee

et al. [19], all these flames involved soot oxidation in the presence of hydrocarbons, requiring corrections for effects of soot surface growth. Unfortunately, soot surface growth models also have significant uncertainties. An estimation of soot surface growth using models by Frenklach et al. [42], Colket et al. [43], and Kim et al. [40] for flames in Ref. [34] shows a maximum difference by factor of 3. The oxidation rate expressions of Refs. [11, 12] for O_2 and OH were only able to explain a portion of their measurements. This level of discrepancy can be caused by the uncertainties either in soot oxidation mechanism in diffusion flames, or in soot growth correction. It would be beneficial, therefore, to avoid such soot growth in soot oxidation studies.

Soot oxidation has been included in several numerical models with detailed reaction kinetics. The leading numerical model of soot formation and oxidation is that by Appel, Bockhorn, and Frenklach (ABF) [2, 3, 42]. ABF includes an OH collision efficiency of 0.13 and Arrhenius O_2 oxidation rates of surface radical sites from low temperature shock tube studies of phenyl (C_6H_5) oxidation by Lin and Lin [44]. The OH is assumed to directly react with the arm-chair site on the soot particle surface C_{soot}-H, while the O_2 is assumed to only react with the corresponding radical C_{soot}•. The fraction, χ of the soot radical site is determined from:

$$\chi_{C_{soot}\bullet} = \frac{k_8[\mathrm{H}]}{k_{-8}[\mathrm{H_2}] + k_9[\mathrm{H}] + k_{10}[\mathrm{C_2H_2}] + k_{11}[\mathrm{O_2}]} \chi_{C_{soot}-H}, \tag{1-10}$$

where k_i is the reaction rate constant from Refs. [2, 42]. The above conversion assumes that soot growth is through the hydrogen abstraction and acetylene addition progress.

Other widely used soot models use disparate soot oxidation rates. Leung et al. [1] included only O_2 as a soot oxidant and used a rate 8 times higher than Lee et al. [19], which they admitted was a weakness. Liu et al. [4] included soot oxidation by OH and O_2 and found that correction factors (between 0 – 1) were required for both the OH mechanism of Neoh et al. [12] and the O_2 mechanism of NSC. Connelly et al. [45] considered soot oxidation by OH (with a collision efficiency of 0.13) and O_2 (using the NSC mechanism). Bhatt and Lindstedt [6] invoked oxidation rate expressions for OH, O (with collision efficiencies of 0.05 and 0.2, respectively) and O_2, all attributed to the shock-tube studies of Roth et al. [46]. Celnik et al. [7] introduced soot oxidation rates based on density function theory simulations that were first order in O_2 with Arrhenius behavior. Their oxidation model predicts much lower soot oxidation rates by O_2 than ABF and it neglects oxidation by OH.

The diversity in soot oxidation rate expressions that exist in the leading models attests to the associated uncertainties. If the soot oxidation kinetics in ABF and the other soot models are inaccurate, then there remains substantial room for improvement. It is concerning that all these models neglect soot oxidation by CO_2 and H_2O (which have volume fractions on the order of 0.1 in hydrocarbon/air flames). Furthermore, any inaccuracies in the chosen soot oxidation models have probably contributed to inaccuracies in soot formation models, because soot formation and oxidation compete in the flames used to validate ABF and the other detailed soot models. Uncertainties in soot oxidation are a major weakness of soot modeling and amply motivate the study proposed here.

1.3. Objectives

The study will focus on improving and validating the soot oxidation kinetics with a flame system where soot oxidation and soot formation regions are far separated. Six main objectives have been established in this study to advance understanding of soot oxidation kinetics. This research seeks to:

1) Develop a ternary flame system where the soot oxidation and soot formation regions are separated. A ternary flame system is considered that directs a buoyant soot column into a hydrogen diffusion flame, producing a soot flame.
2) Develop optical diagnostics to measure soot temperature and soot volume fraction in steady axisymmetric flames.
3) Measure detailed properties of the soot flame: soot temperature, soot volume fraction, velocity, soot primary particle diameter, and major species concentrations (H_2, O_2, N_2, CO, CO_2, and H_2O).
4) Estimate the radical concentrations particularly OH, but also O and H.
5) Evaluate existing soot oxidation kinetics expressions and develop improved expressions for O_2 and OH.
6) Develop improved expressions for soot flux and soot oxidation rate, and obtain the soot oxidation rate from the measurements.

It is hoped that this work will lead to improved models of soot oxidation by O_2 and OH. This, in turn, could lead to improved models of soot growth by allowing better oxidation corrections in soot growth measurements.

Chapter 2: Soot Flame Development

A ternary flame system is presented that allows observations of soot oxidation in a hydrogen diffusion flame in the absence of hydrocarbons. A propylene/air laminar jet diffusion flame emits a soot column that passes through a ring burner supporting a hydrogen diffusion flame. The soot oxidizes in a region with a diameter and length of 3 and 60 mm, respectively. This region is laminar, steady, axisymmetric, and freely accessible for optical and sampling diagnostics. Temperatures and soot loading can be controlled nearly independently and a broad range of mixture fractions are encountered without interference from soot formation.

2.1. Flame Development Introduction

An improved understanding of pollutant and radiative emissions from flames and fires will require an improved understanding of soot nucleation, growth, and oxidation. A recent study [5] compared the predictions of 36 detailed gas and soot kinetic models with measurements from eight laminar diffusion and premixed flames. No model matched the peak soot volume fractions within a factor of 5 for all eight flames.

Improved soot oxidation measurements could lead to improved models of not only soot oxidation but also soot growth. Most soot growth models are based on measurements for which significant soot oxidation corrections have been made, e.g., Refs. [47-49]. This may have contributed to the large variations in predicted and measured soot growth rates [5].

One of the most widely used models of soot oxidation rates is questionable because it did not consider soot or aerosols. Nagle and Strickland-Constable [11] instead inferred soot oxidation rates by O_2 by observing the oxidation of various heated carbon rods in oxygen jets. This model disagrees with many soot aerosol measurements; for example, it overpredicts the measurements of Ref. [15, 16, 19] while underpredicting those of Ref. [18, 22]. Soot oxidation by O_2 has also been studied using thermogravimetic analysis [24, 28, 29], but this environment too is very different from a flame and temperatures were below 1000 K.

A full understanding of soot oxidation will require its study in both premixed and diffusion flames. Neoh et al. [12, 14] considered a two-stage premixed flame system. After correcting for O_2 soot oxidation as predicted by Ref. [11], OH was found to be the principal soot oxidizer, with an average collision efficiency of 0.13. Echavarria et al. [17, 31] used a similar premixed flame setup, but did not examine soot oxidation kinetics. In both studies soot deposition prevented the observation of long-term steady flames and high spatial resolution was required to resolve the 5 mm soot oxidation region.

Soot oxidation rates have been measured in many hydrocarbon diffusion flames [15, 16, 34, 39-41]. Most these measurements were in the presence of hydrocarbons, requiring significant corrections for soot nucleation and growth. Some of the measurements were in very lean regions without hydrocarbons, but these involved low temperatures, low soot loadings, and late-stage soot that may not represent typical soot in diffusion flames.

Thus motivated, the objective of this study is to develop a ternary flame system that allows soot oxidation to be observed in a diffusion flame in the absence of soot formation. Detailed measurements in this system could lead to improved soot oxidation models.

2.2. Flame Development Experimental

The ternary flame system developed here involves three flames burning in air at 1.01 bar: a propylene diffusion flame, a hydrogen diffusion flame, and a soot flame. A sooting propylene/air laminar jet diffusion flame was established on a coflow burner [50], consisting of concentric brass tubes with inner diameters of 14 and 101.6 mm. The sketch of the coflow burner is shown in Fig. 2-1. The flow of propylene (2.1 mg/s, 99.5% purity) through the inner tube was surrounded by coflowing air (1.18 g/s). The propylene flame exhibited a steady luminous length of 50 mm and emitted soot in a vertical column.

A ring burner was fabricated as shown in Fig. 2-2. A round brass rod was cut to length and drilled on center. The plenum groove was milled, and 41 jet holes and the tapered port were drilled. A short section of the brass rod was drilled on center and welded in place to complete the plenum. The calculated pressure drop through the holes is at least 10 times that within the plenum. The ring burner was positioned with its upper face 80 mm above the coflow burner and on the same axis. Hydrogen (1.48 mg/s, 99.9995% purity) was delivered to the ring burner. The hydrogen flow (like that of the propylene and the air) was controlled with a pressure regulator and a needle valve, and measured with a rotameter that was calibrated with a soap bubble meter.

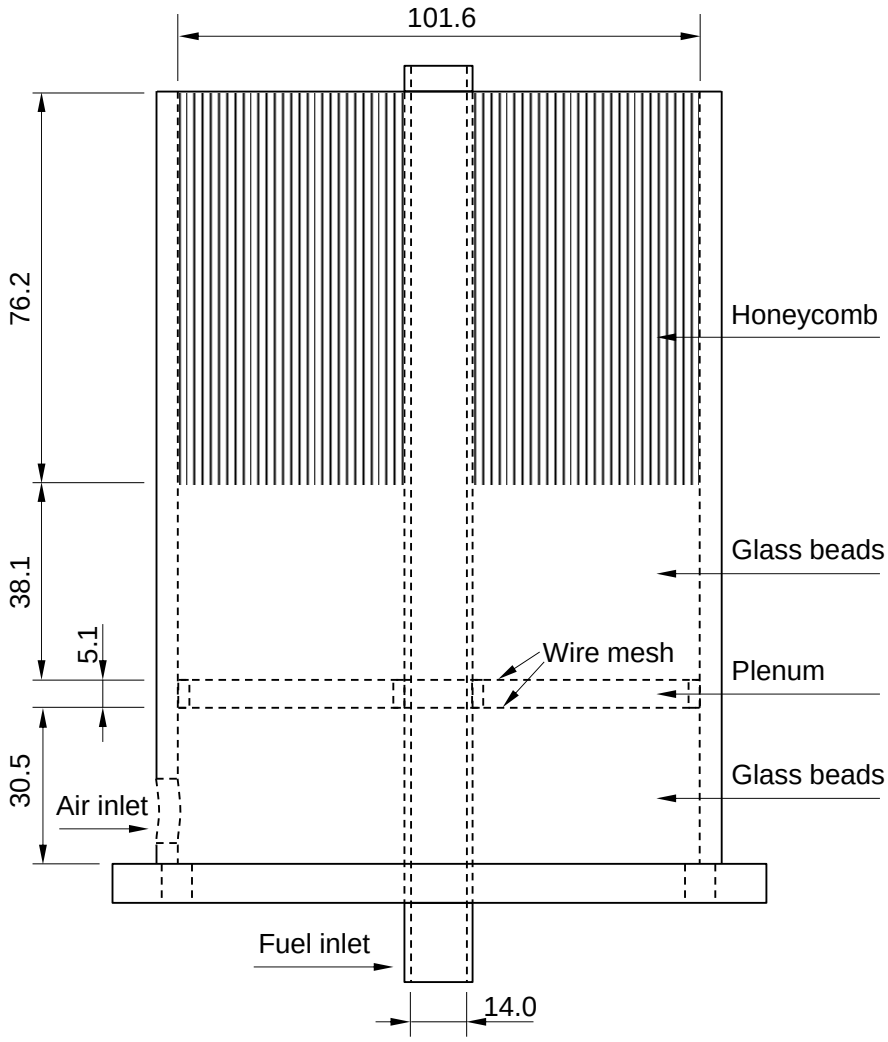

Figure 2-1 Sketch of the brass coflow burner, with dimensions in mm.

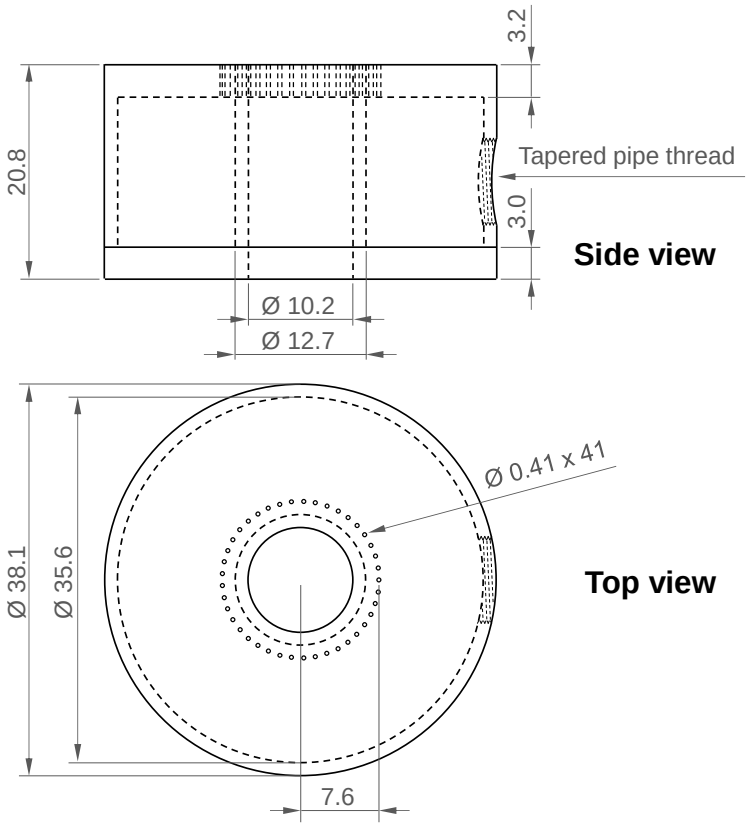

Figure 2-2 Sketch of the brass ring burner, with dimensions in mm.

2.3. Flame Development Results and Discussion

The performance of the ring burner alone was tested with hydrogen, and with methane for improved flame visibility. Ring flames shorter than 10 mm were not axisymmetric and those longer than 70 mm flickered, however those between 10 – 70 mm were both steady and axisymmetric. Flames longer than 25 mm had stoichiometric regions that extended to the burner axis. The stoichiometric length of the hydrogen flame used in the ternary flame system was approximately 30 mm, but a precise determination is difficult owing to the dim and broadened reaction zones of hydrogen diffusion flames.

Figure 2-3 is a color image of the ternary flame system. The soot flame became luminous at a height of 8 mm above the ring burner face and remained steady for 60 mm. The soot column reached a maximum diameter of 3.3 mm at a height of 13 mm and then narrowed. The soot flame was found to be steady, laminar, axisymmetric and optically thin. The openly accessible soot flame facilitates soot and gas sampling, as well as optical diagnostics. It allows the observation of soot oxidation in a diffusion flame far separated from soot formation regions.

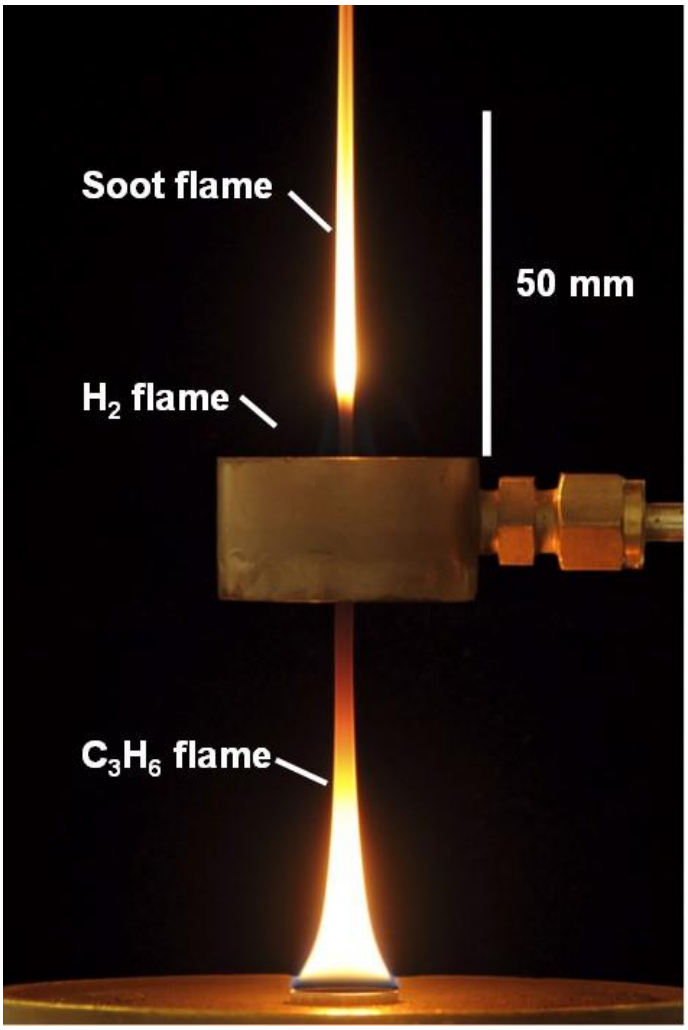

Figure 2-3 Color image of the ternary flame system.

Temperatures measured with a K-type thermocouple on the flame axis at the entrance to the ring burner were below 600 K, indicating that most of the gaseous products of the propylene diffusion flame had been replaced by N_2 and O_2. This reduced the hydrocarbon and CO_2 concentrations in the soot flame, which otherwise would have contributed to soot formation and oxidation. The detailed diagram of the ternary flame system in Fig. 2-3 was shown in Fig. 2-4.

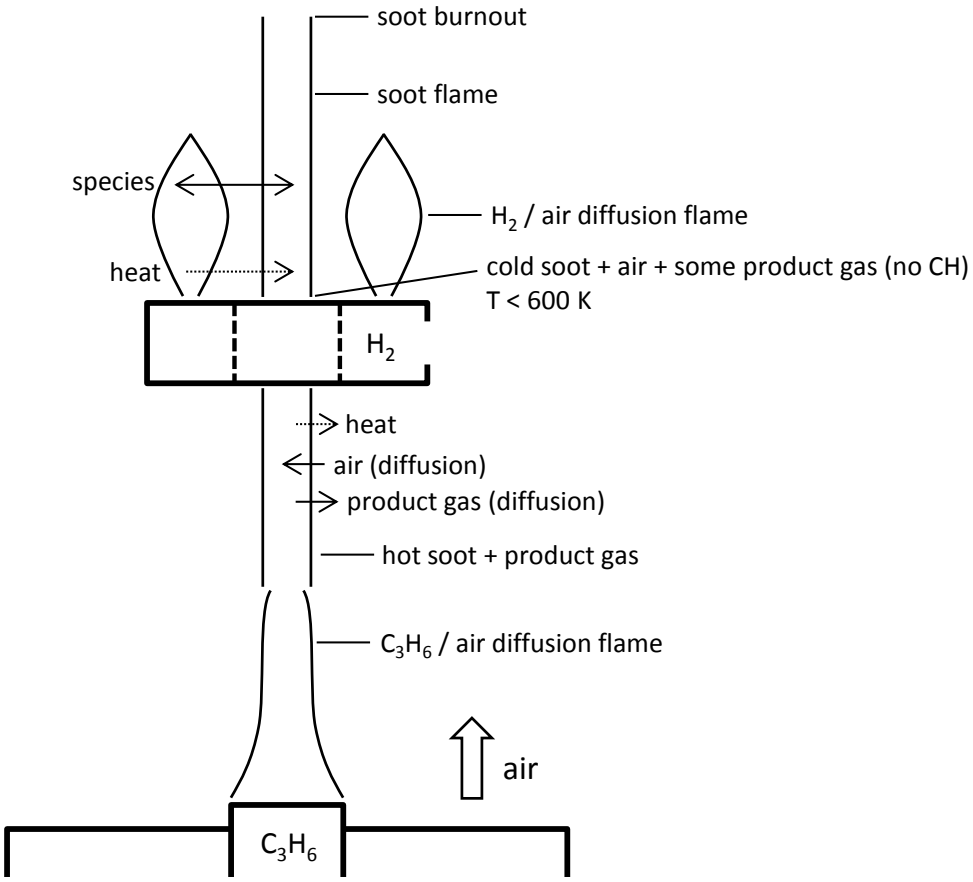

Figure 2-4 Diagram of the ternary flame system.

Soot loading and temperature can be controlled independently in the soot flame. Soot loading can be adjusted by changing the propylene flow rate or by using a different fuel. Temperature can be adjusted by changing the hydrogen flow rate or by introducing oxygen or diluent into the coflow or hydrogen stream. Modifications to this flame system might allow it to be used for studies of soot growth, nanoparticle processing, or other aerosol physics experiments.

2.4. Other Ternary Flames

Other tested ternary flames, flame (1) and (2), developed with similar experiment setup are shown in Fig. 2-5. These two flames demonstrate the ability of the current flame design to independently control the soot loading and temperature. The coflow burner has the same dimensions except that the fuel tube inner diameter is 11.1 mm. Acetylene has a higher sooting tendency, and the acetylene flame starts sooting at a lower fuel flow rate. It was therefore used as fuel for higher soot loading and shorter flame length. Coflowing air and the ring burner fuel were kept the same with varied flow rates. The ring burner upper surface was placed 87 mm above the coflow fuel port. The higher ring burner location allows more entrainment of air, more replacement of the gaseous product, and longer residence time to cool down. Flow rates of acetylene, hydrogen, and coflow air were maintained with manual metering valves and measured with rotameters, which were calibrated with soap bubble meters. Two flames are considered: flame (1) has a large ring flame with stoichiometric regions that cross the axis; flame (2) has a small ring flame with only lean conditions on the axis. The conditions are given in Table 2-1.

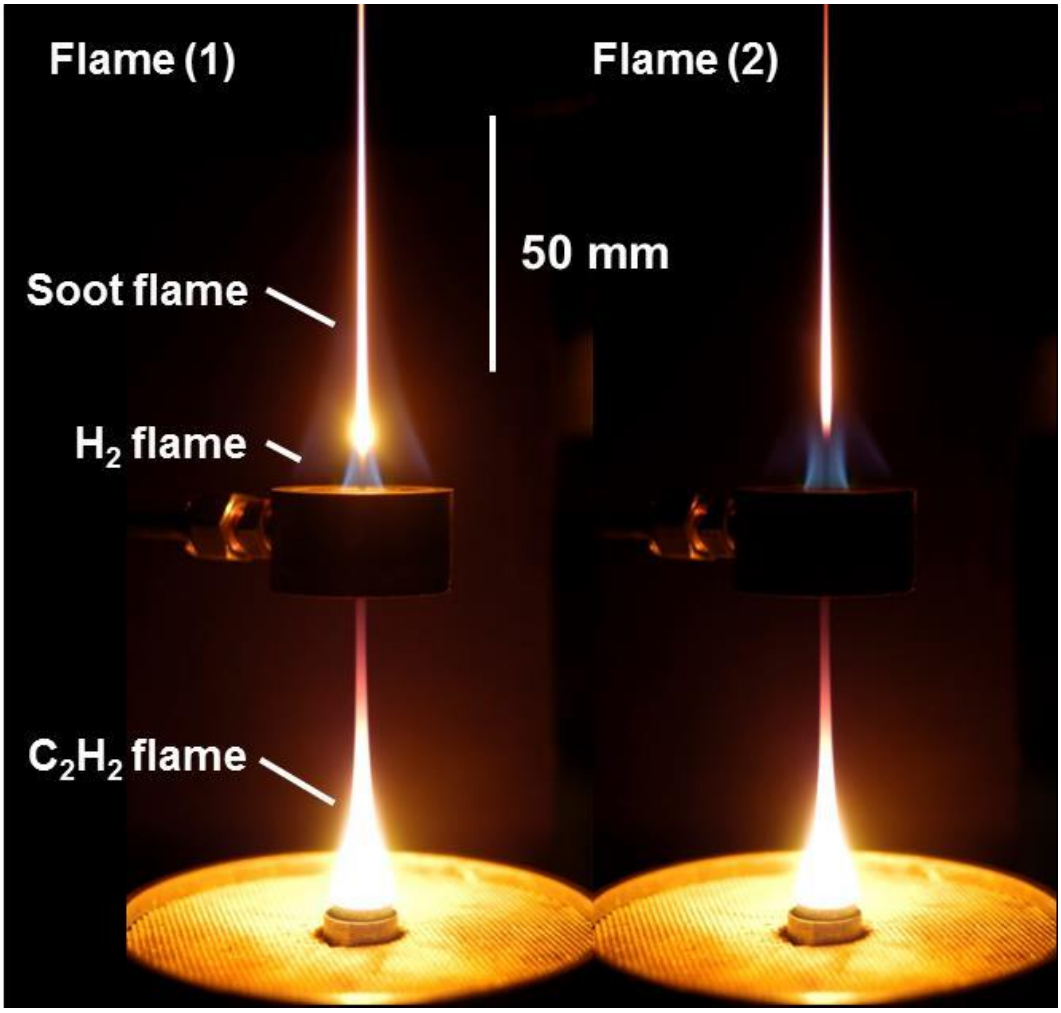

Figure 2-5 Color image of other ternary flames (1) and (2).

The lower flames are laminar, axisymmetric, optically thin, and have luminous lengths of about 75 mm. Emitted soot columns have a narrower diameter of about 2 mm before entering the ring burner. The soot columns are higher soot loading and radiate more heat, so that the soot columns entering the ring burner are cooler initially.

Table 2-1 Test conditions for flame (1) and (2).

	Flame (1) (mg/s)	Flame (2) (mg/s)
Acetylene	2.60	2.21
Hydrogen	2.22	1.50
Air	1183	1183

The hydrogen flow rate in flame (2) is similar to that used in the finalized flame design in Fig. 2-3, and its stoichiometric regions do not cross the axis. The higher hydrogen flow rate in flame (1) increases the soot flame temperature. More soot irradiance was detected at heights between 10 – 30 mm, as shown in Fig. 2-5. However, soot oxidation here is too small to be accurately detected (estimated < 0.1 g/m^2-s). Though the flame temperature is much higher, the major oxidants concentration (O_2 and OH) are estimated to be low at the rich condition to allow sufficient soot oxidation.

High soot loading in these flames prevented steady isokinetic sampling and accurate major species analysis in the interested regions. However, the range of temperatures, soot loading, and stoichiometric conditions achieved are of particular interest, as it facilitates the soot oxidation study in widely varied test conditions.

2.5. Flame Development Summary

To improve the understanding of soot oxidation, a novel ternary flame system was developed to allow soot oxidation observed in a hydrogen diffusion flame in the absence of hydrocarbons. The ternary flame system comprises a coflowing propylene/air diffusion flame to generate a steady soot column that flows into a hydrogen ring flame. The soot is

thereby oxidized in a region far separated from soot formation. The soot flame was found to be laminar, steady, axisymmetric, and optically thin. With this flame system design, temperature and soot loading are able to be controlled nearly independently, and a broad range of mixture fractions can also be achieved.

Chapter 3: Optical Diagnostics for Temperature and Soot Volume Fraction

New diagnostics are presented that use a digital camera to measure full-field soot temperatures and soot volume fractions in axisymmetric flames. The camera is a Nikon D700 with 12 megapixels and 14 bit depth in each color plane, and was modified by removing the infrared and anti-aliasing filters. The diagnostics were calibrated with a blackbody furnace. The flame considered here was an 88 mm long ethylene/air coflowing laminar jet diffusion flame on a round 11.1 mm burner. The resolution in the flame plane is estimated to be between $0.1 - 0.7$ mm. Soot temperatures were measured from soot radiative emissions, using ratio pyrometry at 450, 650, and 900 nm following deconvolution. These had a range of $1600 - 1850$ K, temporal resolutions of 125 ms, and an estimated uncertainty of ± 50 K. Soot volume fractions were measured two different ways: from soot radiative emissions and from soot laser extinction at 632.8 nm, both following deconvolution. Soot volume fractions determined from emissions had a range of $0.1 - 10$ ppm, temporal resolutions of 125 ms, and an estimated uncertainty of $\pm 30\%$. Soot volume fractions determined from laser extinction had a range of $0.2 - 10$ ppm, similar temporal resolutions, and an estimated uncertainty of $\pm 10\%$. The present measurements agree with past measurements in this flame using traversing optics and probes, but they avoid the long test times and other complications of such traditional methods.

3.1. Optical Diagnostics Introduction

Accurate measurements of soot temperature and soot concentration in flames are essential for gaining insight into many combustion processes. These measurements can be performed optically and nonintrusively in flames. Many flames of interest are axisymmetric and optically thin, which simplifies the measurements significantly.

Several studies have performed soot pyrometry following deconvolution in axisymmetric flames based on soot radiative emissions. Sunderland et al. [47, 48] used ratio pyrometry with a photomultiplier tube at 600, 700, 750, and 830 nm, but this required traversing the optics across the flame at each height and wavelength. Gulder and co-workers [51-53] used ratio pyrometry with a spectrometer and imaged the spectra with a charge coupled device (CCD). Again, traversing the burner horizontally at each height was required. Faeth and co-workers [54, 55] used grayscale CCD video cameras to perform ratio pyrometry (at 650 and 850 nm) in microgravity flames, but the cameras had a low bit depth (8 bits per color plane) and a low pixel count (0.1 megapixels). Long and co-workers [56, 57] used more modern color digital cameras without external bandpass filters for three-color ratio pyrometry. Unfortunately, the uncertainties were greater than in narrow-band methods [58].

Soot volume fractions can also be found from soot radiative emissions [53, 56, 57, 59, 60], with instrument setups similar to those used in the ratio pyrometry. Temperatures are determined using soot pyrometry and then these temperatures are considered with the soot radiative emissions to determine soot volume fractions. Unfortunately, the resulting

uncertainties in soot volume fraction increase exponentially with uncertainties in temperature.

Soot volume fractions have also been measured in axisymmetric flames using laser extinction and assuming Rayleigh scattering from soot. Santoro et al. [50, 61] did so in ethylene/air coflowing diffusion flames. As with the early work in soot pyrometry, single point detectors were used, requiring extensive traversing. Full-field soot volume fraction measurements with CCD cameras were reported in Refs. [54, 55, 62-64]. Faeth and co-workers [54, 55] used a laser diode at 632 nm, but, as in their soot pyrometry work, used a camera with a low bit depth and a low pixel count. Gulder and co-workers [64] used a mercury arc lamp and a more advanced camera. However, arc lamps introduce unsteadiness, collimation difficulties, and uncertainties in the soot extinction coefficient.

The use of still digital cameras for combustion diagnostics is increasing [56, 57, 65]. As digital camera technology improves, so too improve the measurements that can be performed. Recent advances in camera technology – including higher bit depth, higher pixel counts, larger sensor arrays, and decreased noise – allow nonintrusive full-field measurements in flames with increasing accuracy, speed, and spatial resolution.

This study involves the development of full-field diagnostics of soot temperature and soot volume fraction in a steady axisymmetric ethylene/air laminar diffusion flame using a digital single-lens reflex (SLR) camera. The results are compared with past measurements involving single point detectors and thermocouples [50, 61].

3.2. Optical Diagnostics Experimental

The flame considered here is an ethylene/air laminar jet diffusion flame. The burner replicates the coflow burner of Ref. [50]. It consists of concentric brass tubes of 11.1 and 101 mm inside diameters. For the coflow, 3 mm glass beads followed by 1.5 mm cell size ceramic honeycomb were used to obtain plug flow. The fuel tube extended 4 mm above the honeycomb. The ethylene and air flow rates were maintained at 4.35 and 856 mg/s (or 3.85 and 713 cm^3/s at laboratory conditions of 1.01 bar and 25 ℃). Rotameters (calibrated with soap bubble meters) were used to monitor the fuel and air flow rates. The visible flame height was 88 mm, as shown in Fig. 3-1. Measurements confirmed that the flame was steady, not soot emitting, optically thin, and axisymmetric.

A Nikon D700 color SLR camera with a 50 mm *f*/1.4 AF-D Nikkor lens was used for both soot temperature and soot volume fraction measurements. A 14 mm extension tube (Nikon PK-12) was used to obtain focus at a distance of 24 cm from the sensor. The camera contains a 36 × 24 mm complementary metal-oxide-semiconductor (CMOS) sensor with 12 megapixels (4256 × 2832 pixels) and 14 bit depth in each of the three color planes. The camera was modified by removing the infrared cut filter, allowing measurements at 900 nm. The anti-aliasing filter was also removed to improve focus. A long pass filter (Schott WG280) was added to maintain matched focusing at the CMOS and the eyepiece. All automatic exposure and image post-processing options were disabled. The aperture was set to *f*/4 (for a 10 mm depth of field), the ISO was 200, and the white balance setting was direct sunlight. Shutter speed was optimized for each image such that no pixels were saturated in any color plane. Each image recorded the entire

flame, and none of the results presented here use different images in different regions of the flame. The shutter was controlled remotely.

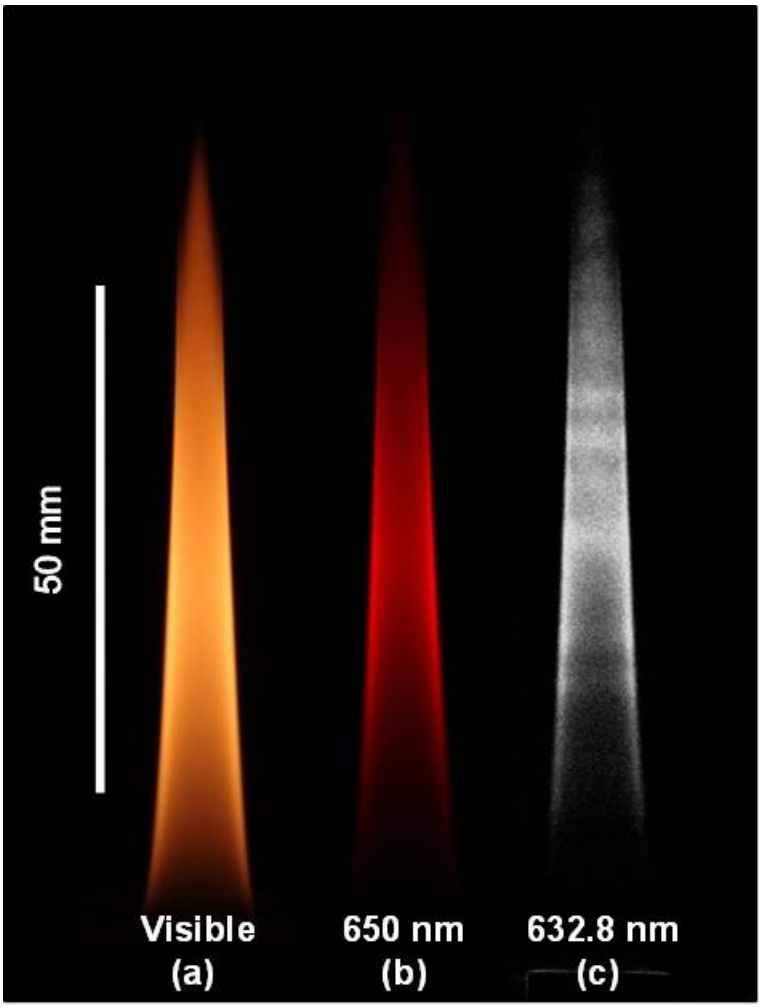

Figure 3-1 Flame images: (a) color flame image, (b) color flame image with 650 nm bandpass filter, and (c) flattened laser plus flame image following subtraction of flattened laser only image.

Images were initially saved in uncompressed Nikon-specific format. To avoid gamma corrections, the conversion to tif format was performed using Dcraw [66]. With the exceptions of "– 4" and "– *T*," only default settings were used. The three color planes were flattened to grayscale using arithmetic means.

A blackbody furnace (Oriel 67032) was used to calibrate the pyrometer and to confirm linear camera response. The furnace had a 25 mm cavity opening, an emissivity of $\varepsilon = 0.99 \pm 0.01$, and a temperature accuracy of ± 0.1 ℃ Furnace spectral radiance, W_λ, was obtained from Planck's law:

$$W_\lambda = \varepsilon B_\lambda = \frac{2hc^2\varepsilon}{\lambda^5\left[\exp(hc/\lambda kT)-1\right]}, \tag{3-1}$$

where B_λ is the ideal blackbody spectral radiance, c is the speed of light, h is Planck's constant, k is Boltzmann's constant, T is temperature, and λ is wavelength. The radiance has a unit of W/sr-m^3. For the conditions considered here the negative unity term in the denominator is negligible.

Images of the furnace at temperatures of 900 − 1200 ºC were recorded using the camera with each of the bandpass filters mounted to the front of the camera lens. These filters (Newport 20BPF10) were 50 mm square, had central wavelengths of 450, 650, and 900 nm, and had full width at half maximum (FWHM) bandwidths of 10 nm. The differences between the central wavelengths were much greater than the bandwidths, which simplified the pyrometry method as developed below. The lens was focused on the furnace opening, which was 24 cm from the CMOS sensor. The lens focus was adjusted slightly for each wavelength to account for chromatic aberrations.

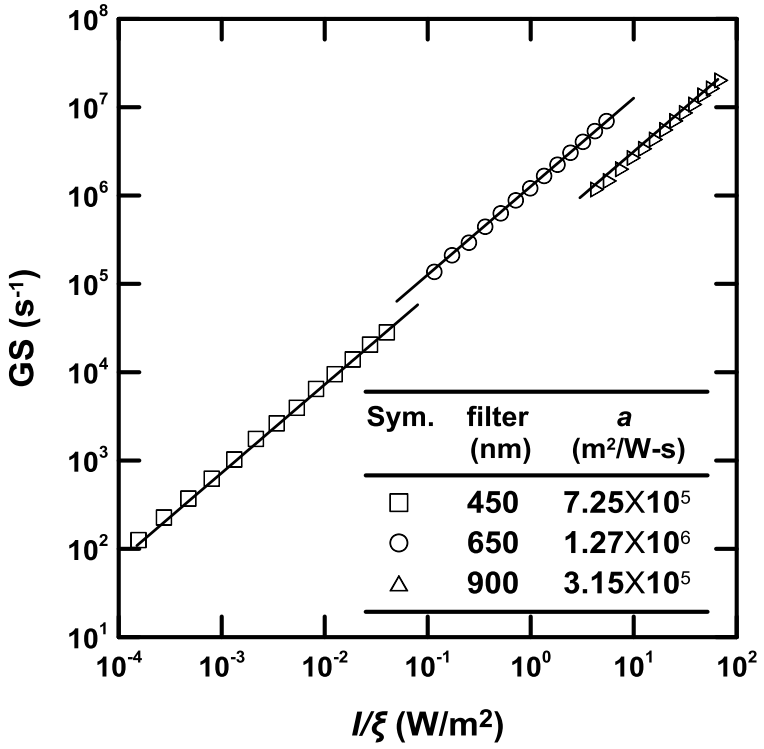

Figure 3-2 Grayscale/shutter time versus irradiance incident on the sensor for each bandpass filter, as determined by blackbody measurements.

The results of these blackbody tests are summarized in Fig. 3-2. The abscissa here is I / ξ, where I is the irradiance incident on the CMOS sensor and is defined as

$$I = \xi \int_0^\infty \tau_\lambda W_\lambda d\lambda \, . \tag{3-2}$$

Here W_λ is from Eq. (3-1), τ_λ is the bandpass filter transmissivity as provided by the manufacturer, and ξ is a constant (independent of wavelength) that accounts for magnification and light losses in the lens, and angular dependence. The integrations were performed in MATLAB. The ordinate of Fig. 3-2 is GS, defined as the grayscale indicated by the camera divided by the shutter time. For each filter considered, the symbols in Fig. 3-2 correspond to different blackbody temperatures (900 – 1200 ℃)

and/or shutter times (0.4 ms – 20 s). The measurements for each bandpass filter were fit according to

$$\mathrm{GS} = aI/\xi\,, \tag{3-3}$$

where *a* is a least-squares fitting constant for each filter with values given in Fig. 3-2. Constant *a* accounts for pixel size, pixel fill factor, and camera sensitivity at the wavelength of interest. The coefficient of determination (R^2) for each such fit is 0.998 or higher.

To obtain soot temperatures, and soot volume fractions from soot radiative emissions, images of the flame were recorded using the 450, 650, and 900 nm bandpass filters. Although both measurements can be performed with just two bandpass filters, this would increase the uncertainties by about 50%. Three filters yield three measurements at each point (instead of one) of both temperature and soot volume fraction. These can be used to obtain averages and to quickly identify regions where the measurements are divergent, and thus less reliable.

The camera was focused on the flame axis, which was 24 cm from the CMOS sensor. The lens focus was adjusted slightly for each wavelength to account for chromatic aberrations. Figure 3-1 (b) shows a representative image of the flame using the 650 nm filter.

With the lens aperture set to *f*/4, all rays imaging a point in the flame onto the CMOS sensor were parallel to within $\pm 2^{o}$. Parallel light collection was thus assumed. Smaller apertures and longer collection distances were tested to examine this assumption.

These resulted in temperature differences within the experimental error, but had drawbacks of longer exposure times and decreased spatial resolution, respectively.

Each image was flattened to grayscale and, to reduce noise, grayscales were averaged vertically across 20 pixels (0.46 mm in the object plane). This level of vertical smoothing was used because temperature and soot concentration gradients are small in the vertical direction. Smoothing in the radial direction was performed using Fourier transforms with a cutoff frequency of 0.05 pixel^{-1}.

For the soot emission measurements the pixel resolution in the object plane was 23 μm and the longest shutter time was 125 ms. Accounting for smoothing and non-parallel light in the flame plane, it is estimated that the vertical and radial resolution in the flame plane was 0.46 and 0.3 mm, respectively. The axis of the flame was precisely identified in each image. Because the flame was observed to be nearly axisymmetric, grayscales on both sides of the axis were averaged at each height to reduce noise.

The blackbody calibration of Eq. (3-3) was used to convert each measured GS to the line-of-sight integrated irradiance of soot on the CMOS sensor, I/ξ. This quantity is related to the flame properties along the line of sight according to [53]:

$$I(x)/\xi = \tau\Delta\lambda\int_{-R}^{R} K_{abs}(x,y)\, B_{\lambda}(x,y)\, \exp\left[-\int_{y}^{R} K_{ext}(x,y')\, dy'\right] dy\,, \tag{3-4}$$

where B_λ is defined in Eq. (3-1), K_{abs} and K_{ext} are the soot absorption and extinction coefficients, R is flame radius, x (and y) are the horizontal coordinates in (and perpendicular to) the object plane, primes denote the integration variable, and τ and $\Delta\lambda$ are the peak bandpass transmissivity and FWHM as provided by the manufacturer.

Because soot primary particles (approximately 30 nm in diameter) are smaller than the Rayleigh limit (approximately 200 nm at 632.8 nm), Rayleigh scattering by soot was assumed. It is also assumed here that K_{abs} and K_{ext} are equal [53, 59], such that

$$K_{abs} = 6\pi E(m) f_s / \lambda , \tag{3-5}$$

as used previously [47, 50], where $E(m)$ is the refractive index absorption function and f_s is the soot volume fraction. Equation (3-5) assumes soot emissivity is proportional to λ^{-1}. Although this is the most common assumption, other studies [56, 57, 59, 60] have proposed a soot emissivity proportional to $\lambda^{-\alpha}$, where α is a dispersion exponent between 0.95 – 1.38 and depends on wavelength and fuel type. Different values were tested here, but these resulted in temperature differences less than 50 K.

Negligible extinction of the soot radiative emissions was assumed, which yields:

$$\int_y^R K_{ext}(x, y')dy' \approx 0 . \tag{3-6}$$

This assumption was supported by the observation that the maximum extinction by the flame of any part of the 632.8 nm laser beam was 25%. For optically thick flames, corrections are required to compensate for this extinction [59, 67-69]. These corrections were tested here at a few representative heights, but are not included in the results below because they resulted in temperature differences of less than 10 K. Equation (3-6) leads to a considerable simplification of Eq. (3-4).

Abel deconvolutions were performed for the 450, 650, and 900 nm images at each height using MatLab to convert the line-of-sight projections to radial distributions assuming negligible extinction [70]

$$\mathrm{GS}(r) = A_b\left[\mathrm{GS}(x)\right], \tag{3-7}$$

where A_b is the Abel deconvolution operator and r is the radius with respect to the flame axis. Details about the deconvolution algorithms used here can be found in Appendix. Note that the units returned by A_b are the units of the operand divided by length. For any pairing of bandpass filters (denoted by subscripts 1 and 2), Eqs. (3-3, 3-4, and 3-7) can be combined to obtain the following expression for the local soot temperature,

$$T = \frac{hc\left(1/\lambda_1 - 1/\lambda_2\right)}{k\ln\left[C_1\mathrm{GS}_2(r)/C_2\mathrm{GS}_1(r)\right]}, \tag{3-8}$$

where λ is the filter central wavelength and $C = a\,\tau\,\Delta\lambda\,/\,\lambda^6$ is a constant for each filter that does not vary with temperature or soot emissivity. An advantage of this ratio pyrometry is that neither $E(m)$, i.e., soot refractive index, nor f_s appears in Eq. (3-8). For soot particles having a diameter range of 20 – 50 nm, the surface temperature is assumed to be equal to the gas temperature. This assumption is validated in some carbon particle studies [71, 72] where the thermal accommodation coefficient was found to be nearly unit. The uncertainty in the soot temperature measurements is estimated to be ± 50 K, with ± 0.1 K precision for relative temperatures.

Temperatures were also measured using a thermocouple in soot-free areas. The thermocouple was an uncoated B-type thermocouple (Pt-30% Rh versus Pt-6% Rh) with a wire diameter of 51 μm and a butt welded junction. Radiation corrections were performed as in Ref. [65] assuming a thermocouple emissivity of 0.2. Measurements were averaged over 10 s at each location. Uncertainty in the corrected thermocouple measurements is estimated to be ± 40 K.

Soot concentrations were measured using two independent methods. For the soot emission method, Eqs. (3-4), (3-5) and (3-8) are combined to obtain, for each bandpass filter,

$$f_s = \frac{\mathrm{GS}(r)\exp\left(hc/k\lambda T\right)}{12\pi^2 hc^2 E(m)C}. \tag{3-9}$$

A refractive index of $m = 1.57 - 0.56\,i$ was assumed [73], which yields a refractive index absorption function of $E(m) = 0.26$. Soot refractive index varies with soot morphology, soot age, and other conditions [74, 75] in ways that are not fully understood. Other commonly invoked values of soot refractive index would change each f_s reported here by a factor of 0.9 – 1.25. The results of Eq. (3-9) are averaged for the three bandpass filters, yielding an estimated uncertainty in f_s of $\pm 30\%$ and a precision of $\pm 4 \times 10^{-4}$ ppm for relative soot volume fractions. The uncertainty in f_s comes mainly from the uncertainty in T, upon which f_s has the exponential dependence shown in Eq. (3-9).

Soot concentrations were also measured with the laser extinction system depicted in Fig. 3-3. The light source was a 7 mW He-Ne laser (Melles Griot 25LHR171) operating at 632.8 nm. Motivated by Ref. [63], the beam was decollimated using two diffuser sets (Thorlabs DG20-220 and DG20-600), the first stationary and the second mounted to a pneumatic vibrator to reduce speckle. The vibrator had an amplitude of 2.5 mm and period of 50 ms. The beam was then collimated to 100 mm using an off-axis parabolic mirror with angle of $30\,°$ and a focal length of 30 cm. After the test section, the beam passed a laser line filter at 632.8 nm with 1 nm FWHM (Andover ANDV12564) and a decollimator with a focal length of 25 cm. A neutral density filter with optical

density of 2 was used to allow a shutter time (167 ms) much longer than the period of the vibrator. A 3.8 mm pinhole was used to provide a 0.5 ° acceptance angle on the optical axis. The camera lens focus was adjusted such that, with the laser turned off, the flame plane was imaged onto the CMOS sensor.

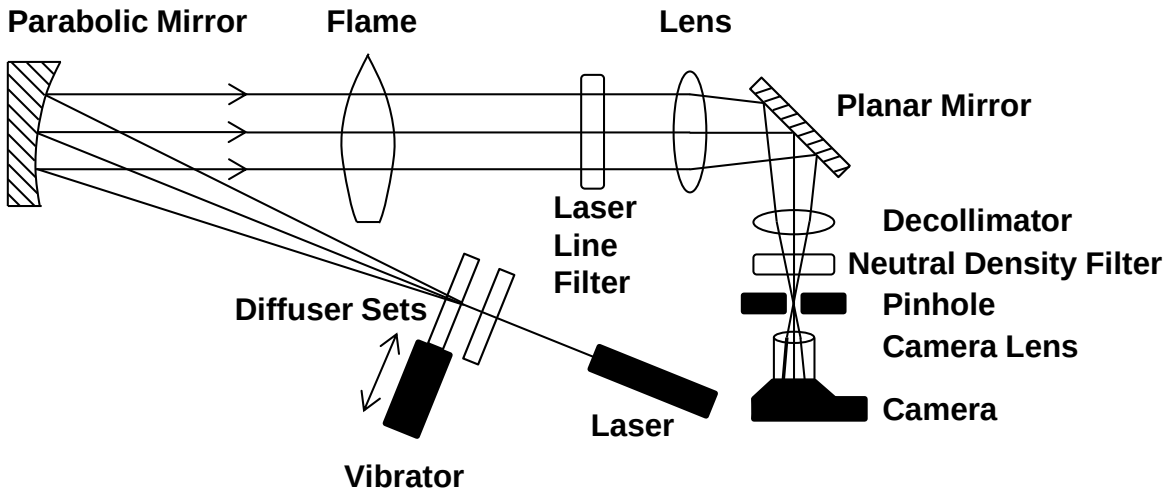

Figure 3-3 Schematic of the laser extinction system.

For the laser extinction measurements the pixel resolution in the object plane was 34 μm and the shutter time was 167 ms. Accounting for smoothing and non-parallel light in the flame plane, it is estimated that the vertical and radial resolution in the flame plane was 0.68 and 0.1 mm, respectively.

Using the laser extinction system, soot volume fraction was measured for the entire flame using two images: the flame image (with the flame and the laser on) and the reference image (with the flame off and the laser on). Some past studies [63] have also recorded and subtracted images with the flame on and the laser off, but such images here had negligible grayscales owing to the 1 nm laser line filter. Figure 3-1 (c) shows the reference image subtracted from the flame image followed by contrast enhancement. Dim

horizontal interference patterns are present as a result of the coherent light source. The negligible grayscales away from the flame arise from the good stability of the laser.

As before, shutter speed was optimized for each image such that no pixels were saturated in any color plane; the shutter was controlled remotely; images were initially saved in uncompressed Nikon-specific format; the conversion to tif format was performed using Dcraw [66]; the three color planes were flattened to grayscale using arithmetic means; grayscales were averaged vertically across 20 pixels (0.68 mm in the object plane); radial Fourier transforms were performed with a cutoff frequency of 0.05 pixel^{-1} for smoothing; and grayscales on both sides of the axis were averaged.

Similar to the pyrometry measurements, the flame and reference images were analyzed assuming Rayleigh scattering. Soot refractive index was again assumed to be $m = 1.57 - 0.56\,i$. The line-of-sight extinction of the incident laser by soot is

$$I(x)/I^0(x) = \exp\left(-\int_{-R}^{R} K_{ext}(x,y)dy\right), \tag{3-10}$$

where the superscript 0 denotes the reference image. Eq. (3-10), combined with Eqs. (3-3) and (3-5), yields the following expression for the local soot volume fraction:

$$f_s(r) = \lambda A_b \left\{\ln\left[\mathrm{GS}^0(x)/\mathrm{GS}(x)\right]\right\}/6\pi E(m). \tag{3-11}$$

These Abel deconvolutions were performed using MatLab to convert the line-of-sight projections to radial distributions [70].

The uncertainty in the laser extinction soot volume fraction measurements is estimated to be $\pm 10\%$, with $\pm 6 \times 10^{-4}$ ppm precision for relative soot volume fractions.

3.3. Optical Diagnostics Results

Full-field soot temperatures were obtained in the soot containing region with ratio pyrometry. Temperatures from the three line pairs were averaged. The difference between the average temperature and any of the three pairs was less than 30 K where soot volume fraction was above 0.5 ppm. In most regions with less than 0.5 ppm soot, noise increased and the difference between the average temperature and any of the line pairs exceeded 30 K. Therefore regions with less than 0.5 ppm soot (e.g., heights below 8 mm, and near the centerline at heights below 40 mm) are not included in the figures shown below. Note that accurate temperature measurements can be performed where soot volume fraction is below 0.5 ppm by using longer exposures. However, longer exposures were not used here because this would have required different images in different regions of the flame.

Figure 3-4 shows the pyrometry results in the soot containing area at representative heights of 10, 20, 50, and 70 mm. Also shown are previous measurements of Santoro et al. [61], who used rapid thermocouple insertion, and the present thermocouple measurements at a height of 50 mm in the soot-free area. The pyrometry and thermocouple results obtained here are in reasonable agreement with those of Santoro et al. [61]. The peak temperatures in this flame are expected to be close to the adiabatic flame temperature (2370 K), but such high temperatures do not appear in Fig. 3-4, because there is insufficient soot to perform soot pyrometry there.

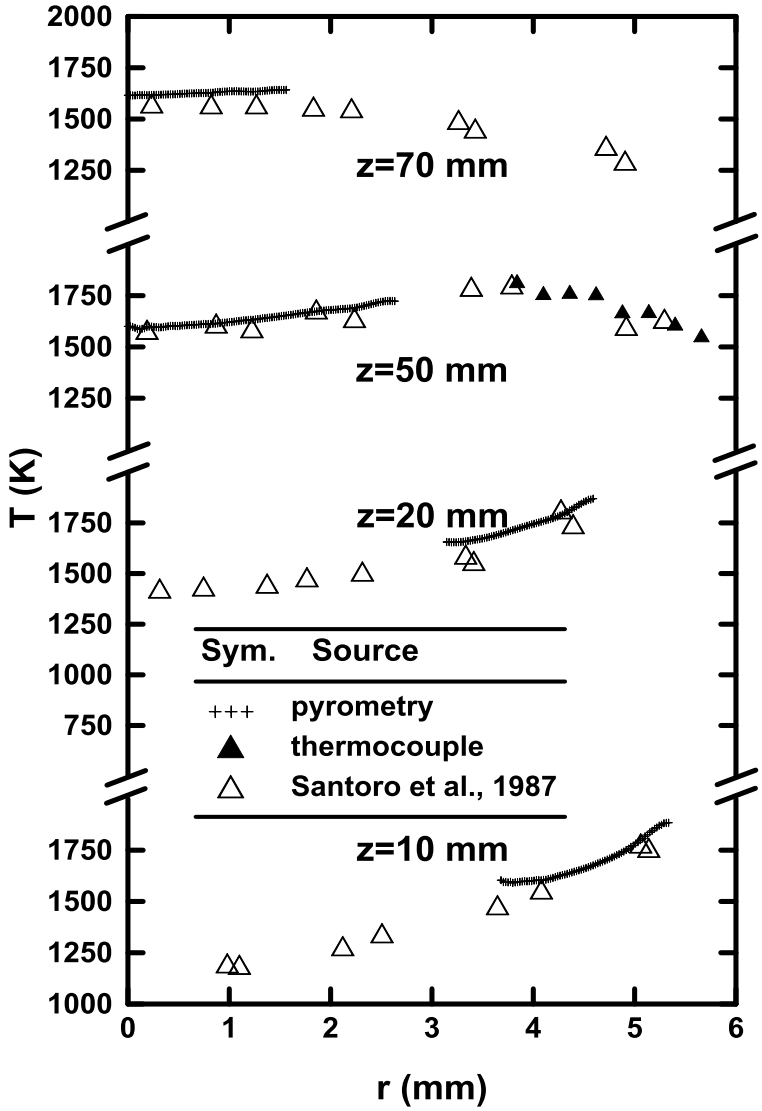

Figure 3-4 Measured temperatures versus radius at heights of 10, 20, 50, and 70 mm.

Figure 3-5 shows a contour plot of the soot pyrometry measurements. Temperatures were measured between 1600 – 1850 K. Temperatures outside this range exist in this flame, but are in regions with insufficient soot concentrations and/or with temperatures that are too low. Work in other flames has demonstrated the extension of this diagnostic to temperatures as low as 1000 K.

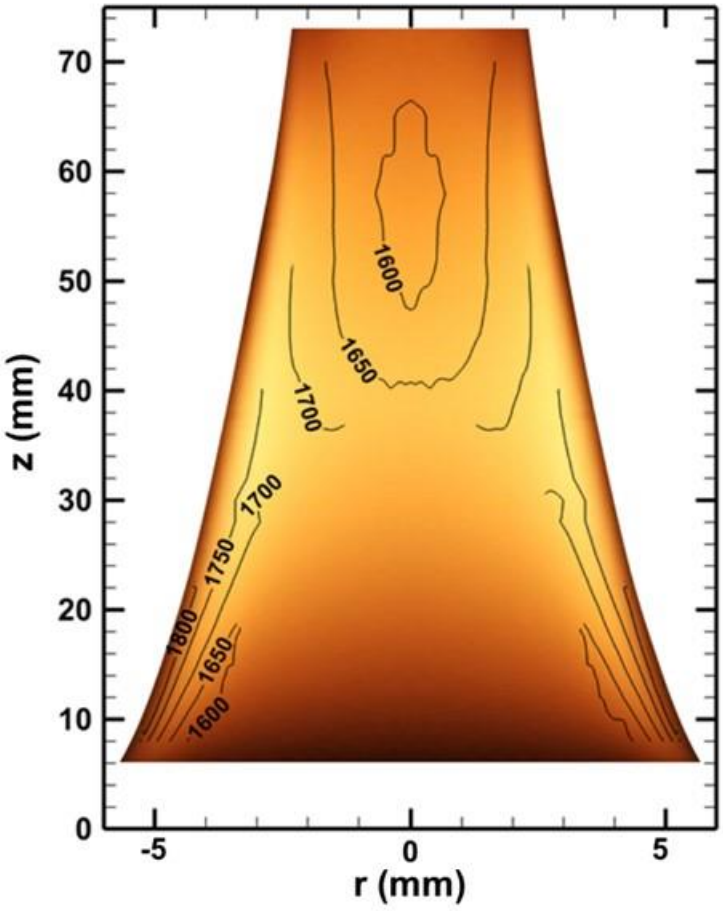

Figure 3-5 Contour plot of pyrometer temperature in K, superimposed onto the color image of Fig. 3-1(a). The radial axis is stretched.

Soot volume fractions were determined from soot emissions with Eq. (3-9) using each of the 450, 650, and 900 nm bandpass filters and then averaged. The difference between the individual determinations and the average was less than 10% at all locations. Soot volume fractions also were measured using the laser extinction system. For heights below 8 mm, insufficient soot was present for reliable measurements of soot volume fraction.

Figure 3-6 shows the measured soot volume fractions at representative heights of 15 and 50 mm above the burner for both the emission and extinction methods. Also shown are the previous measurements of Santoro et al. [50] using laser extinction with a point detector. The three determinations are in reasonable agreement. Small discrepancies in peak soot volume fraction and location are observed, but this is within experimental uncertainties. Near the centerline at 50 mm height, radial ringing in soot volume fraction arises owing to noise accumulation inherent in Abel deconvolutions.

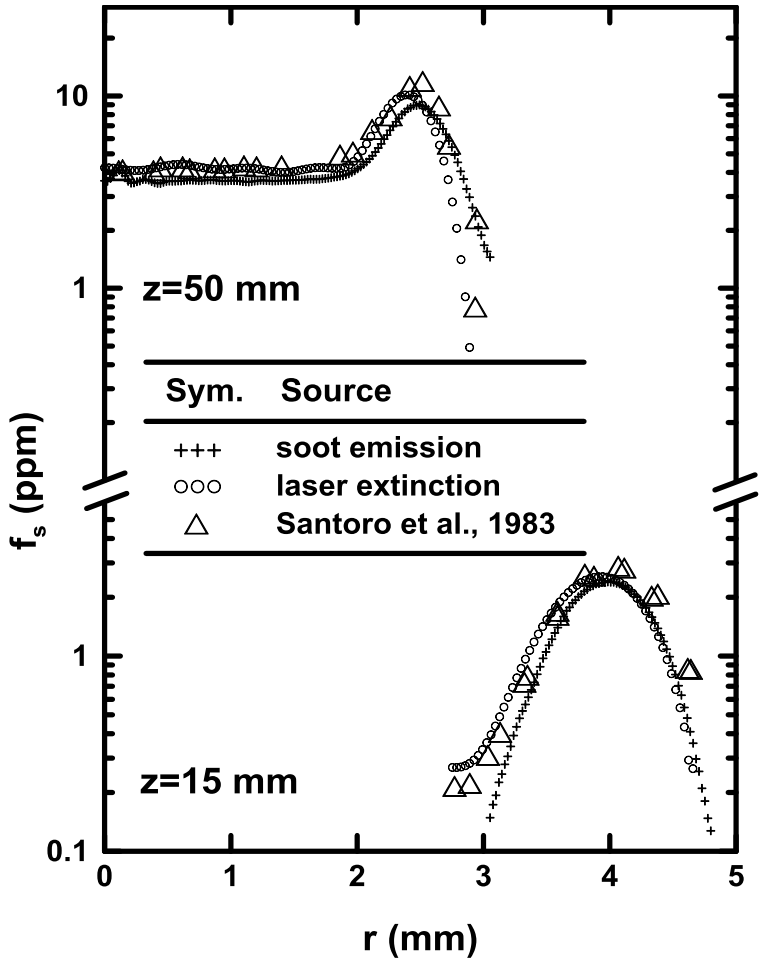

Figure 3-6 Measured soot volume fractions versus radius at heights of 15 and 50 mm.

Contour plots of the soot emission and the laser extinction measurements of soot volume fraction are shown in Fig. 3-7 (a) and Fig. 3-7 (b), respectively. The agreement between the two methods is within 15% at each height. Soot volume fractions were found down to 0.1 ppm using soot emission. This limit was associated with insufficient soot concentrations and/or low temperatures. Soot volume fractions were found down to 0.2 ppm using soot extinction. This limit resulted from nonuniformities in the laser background images. Both methods were able to resolve the highest measured soot volume fractions in this flame (10 ppm). Contour plots of the temperatures and the extinction-derived soot volume fractions are shown in Fig. 3-8 with the flame's aspect ratio preserved.

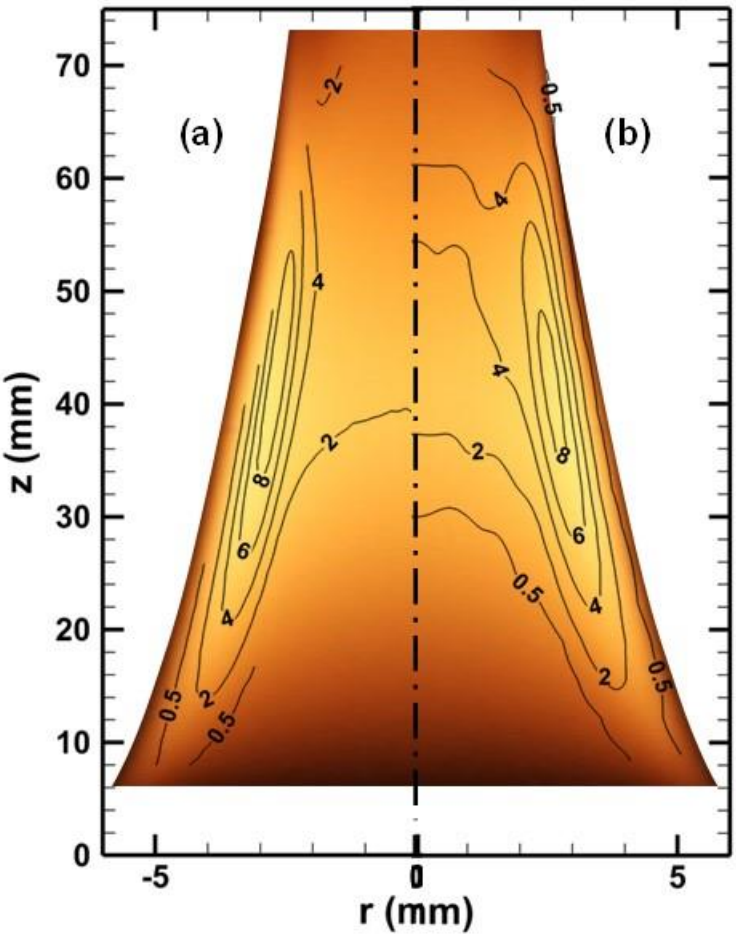

Figure 3-7 Contour plots of soot volume fraction in ppm from (a) emission and (b) extinction methods, superimposed onto the color image. The radial axis is stretched.

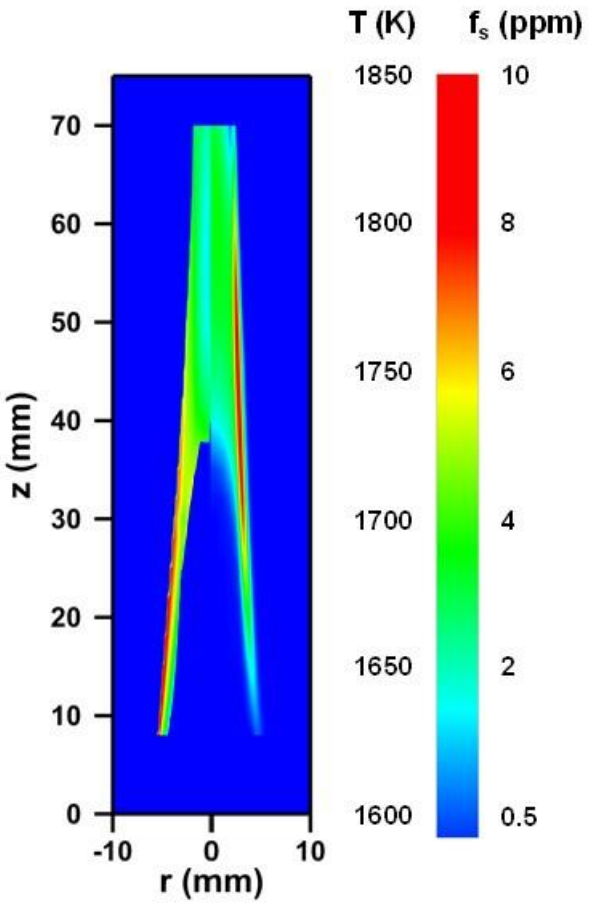

Figure 3-8 Color contour plots of pyrometer temperature (left of centerline) and soot volume fraction from extinction method (right of centerline). The flame's aspect ratio is preserved.

A few comments are needed about the prospects for applying these diagnostics to different flames. First, all three methods exploited the optically thin character of the flame considered. The methods could also be applied in flames approaching optically thick conditions by accounting for self-absorption. The methods cannot be used in optically thick regions. Second, for flames with larger diameters, the measurements of both temperature and soot volume fractions would extend to lower soot volume fractions. Third, although the present flame was steady and axisymmetric, the soot extinction measurements could also be performed in unsteady axisymmetric flames that are

quasisteady on a time scale of about 125 – 167 ms. The other measurements could be performed in such flames by using multiple cameras or, if appropriate, by taking advantage of flame periodicity. Advanced tomographic methods with a sufficient number of cameras would allow the methods to be applied even to nonaxisymmetric flames [76].

3.4. Optical Diagnostics Summary

To sum up, a Nikon D700 SLR camera was used to measure soot temperature and soot volume fraction in an axisymmetric flame. The camera had CMOS sensor with a size of 36×24 mm, a bit depth of 14 in each color plane, and 12 megapixels. The infrared cut filter was removed to image infrared light. The flame was an 88 mm high ethylene/air coflowing laminar jet diffusion flame on an 11.1 mm burner. It was steady, soot containing, optically thin, and axisymmetric.

Soot temperatures were measured with ratio pyrometry and deconvolution. This involved filtered images at 450, 650, and 900 nm with exposures of up to 125 ms each. Temperatures were obtained between $1600 - 1850$ K in the soot containing region with an estimated uncertainty of ± 50 K. Soot volume fractions were measured using two methods, and both were found to agree. Using soot emissions and deconvolution at 450, 650, and 900 nm, soot volume fractions were obtained between 0.1 – 10 ppm with an estimated uncertainty of $\pm 30\%$. Soot volume fractions were also measured with laser extinction at 632.8 nm and deconvolution using a camera exposure of 167 ms. Soot volume fractions were obtained between $0.2 - 10$ ppm with an estimated uncertainty of $\pm 10\%$. Spatial resolution in the object plane is estimated to be better than 0.7 and 0.3 mm

in the vertical and radial directions, respectively. Precision was ± 0.1 K for temperature and approximately $\pm 5 \times 10^{-4}$ ppm for both determinations of soot volume fraction. The results were compared with past measurements and reasonable agreement was observed.

Chapter 4: Soot Flame Characterization

The ternary flame system with a coflow burner and a customized ring burner was introduced. The soot flame was characterized by measuring the following properties: temperature, soot volume fraction, axial velocity, soot primary particle diameter, and major species concentration. Temperatures were measured with ratio pyrometry at 450, 650, and 900 nm, followed by deconvolution. Soo volume fractions were measured with laser extinction at 632.8 nm, followed by deconvolution. The integrated soot volume fractions were determined directly from the laser extinction. Axial velocities were measured from high speed imaging and flow visualization. Soot primary particle diameters were obtained from thermophoretical sampling and analyzed with a transmission electron microscopy (TEM). Gas samples were sampled isokinetcially. H_2O was determined from desiccant gravimetry. Other stable species was analyzed with a gas chromatography (GC) and a thermal conductivity detector (TCD).

4.1. Soot Temperature and Soot Volume Fraction

4.1.1. Soot Temperature Experimental

The soot flame temperature was measured following the basic steps in measuring the reference flame temperature. The following modifications were performed for the current ternary flame system.

Since the ternary flame system involves the relative position of three simultaneous flames, flame flickering can significantly affect the detected grayscales, and in turn the temperature accuracy. In the current study, shutter speed was set less than

0.1 s to freeze the flame fluctuation. Higher ISO (up to 4000) was therefore used for images at 450 nm wavelength where flame irradiance is significantly lower. An ISO calibration was performed with results shown in Fig. 4-1 below. The ISO calibration setup is the same as in the blackbody calibration. Temperature of the furnace was set to 1200 ^{o}C. The camera ISO is confirmed to be linear with a coefficient of determination of 0.9997. Calculated GS was normalized by ISO number.

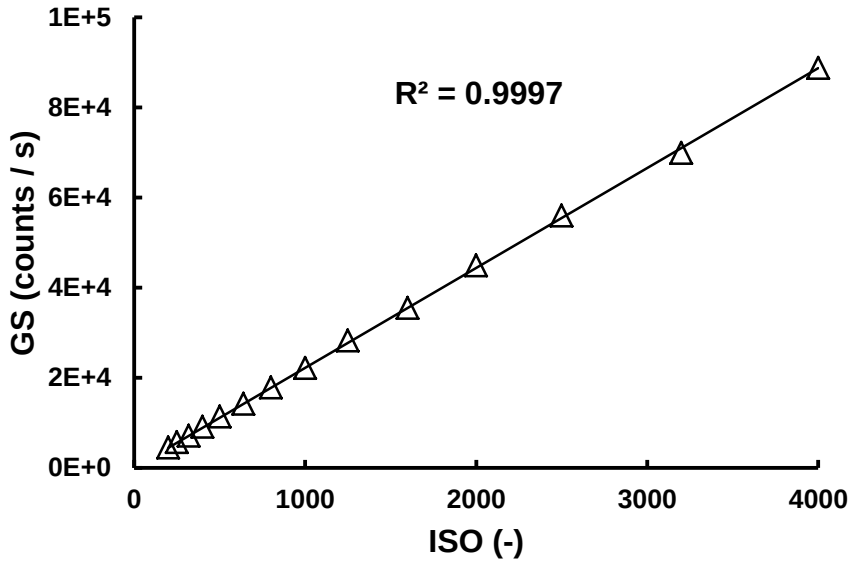

Figure 4-1 ISO Calibration with the blackbody furnace. The furnace temperature was set to 1200 ^{o}C.

The normalized grayscales were smoothed vertically with a Gaussian filter within 20 pixels (0.4 mm height). It was assumed that the flame properties will not change within that vertical distance at the same radial location. A Savitzky-Golay (S-G) filter was applied to horizontally smooth the grayscales. The S-G filter successfully suppresses the noise level with minimal distortion of the peaks. Background noises at the flame

region were obtained by linearly interpolating the grayscales in the flame-free region (< 1% of peak detected grayscales). The background noises were subtracted from the image.

Multiple images were taken for each filter, and the grayscales were averaged with peak locations aligned. The averaged grayscales were deconvolved using the MatLab. In dealing with the current soot flame where soot concentrates annularly within approximately 0.3 mm thickness, off by 1 pixel (0.02 mm) results in grayscale difference of about 30%. Therefore, each pixel was divided to 4 sub-pixels through interpolation. The deconvolved grayscales for each filter were then aligned (0.25 – 2 pixels) in order to obtain better temperature agreements, following Eq. (3-8). Color images of the soot flame at 450, 650, and 900 nm are shown in Fig. 4-2. The grayscales at 450 nm were saturation enhanced.

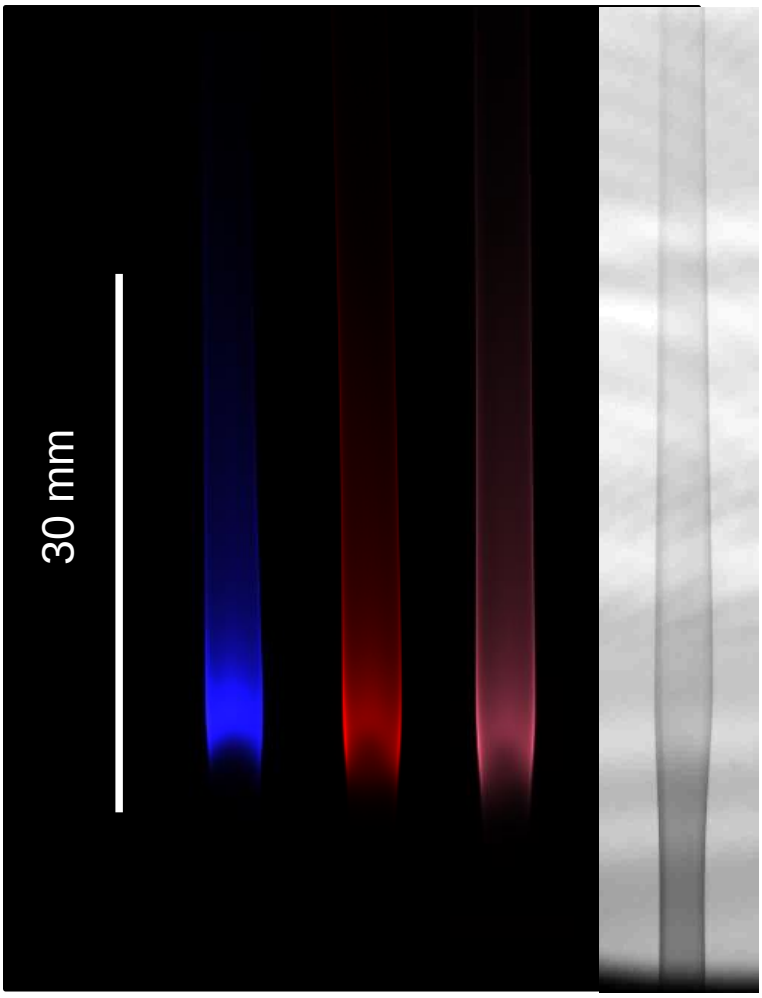

Figure 4-2 Color image of the soot flame at 450, 650, and 900 nm, and the laser extinction image at 632.8 nm.

Figure 4-3 – 4-12 show the deconvolved GS for each filter, and the calculated temperatures for each filter pair, at heights between 10 – 50 mm. Below 13 mm height, the flame temperature was low, resulting in negligible irradiance at flame centerline. Temperatures here were not reported. At 15 mm height, temperatures from three line pairs agree within 50 K in most of the flame region. As height increases, noise in the deconvolved GS also increases due to the reduced irradiance. The reduced flame irradiance is caused by: 1, reduced temperature; and 2, reduced soot concentration owing

to oxidation. The soot column is found to be nearly hollow, and the soot concentrates annularly. The temperature disagreements are higher than 50 K near the flame center with insufficient soot. At soot peak locations, the temperature agreements are conserved, as shown in the following figures.

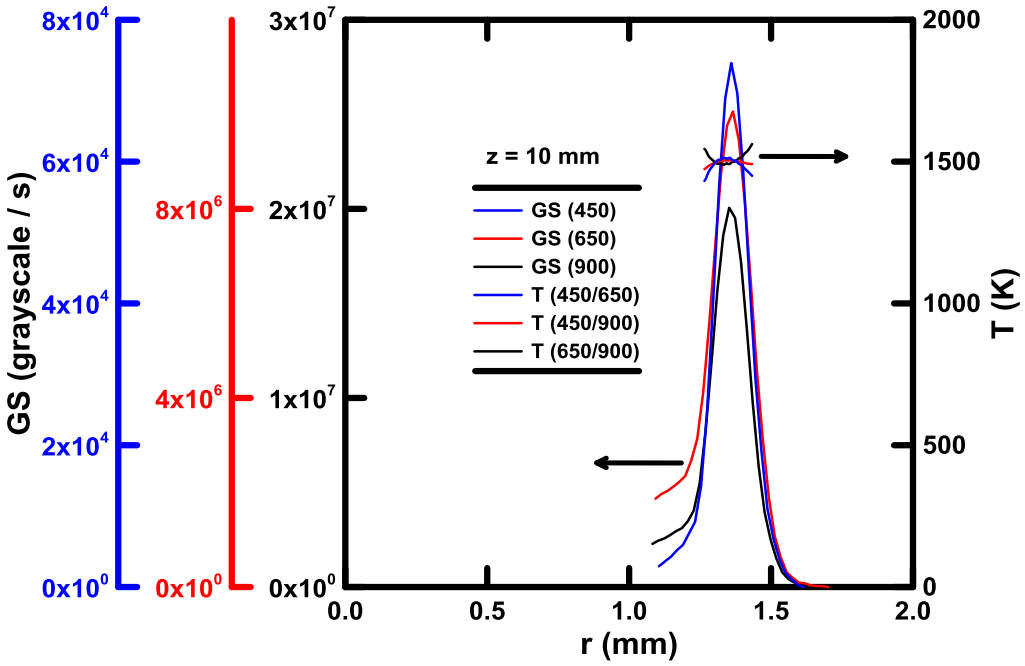

Figure 4-3 Deconvolved Grayscales for each filter and the determined temperatures for each filter pair, at z = 10 mm.

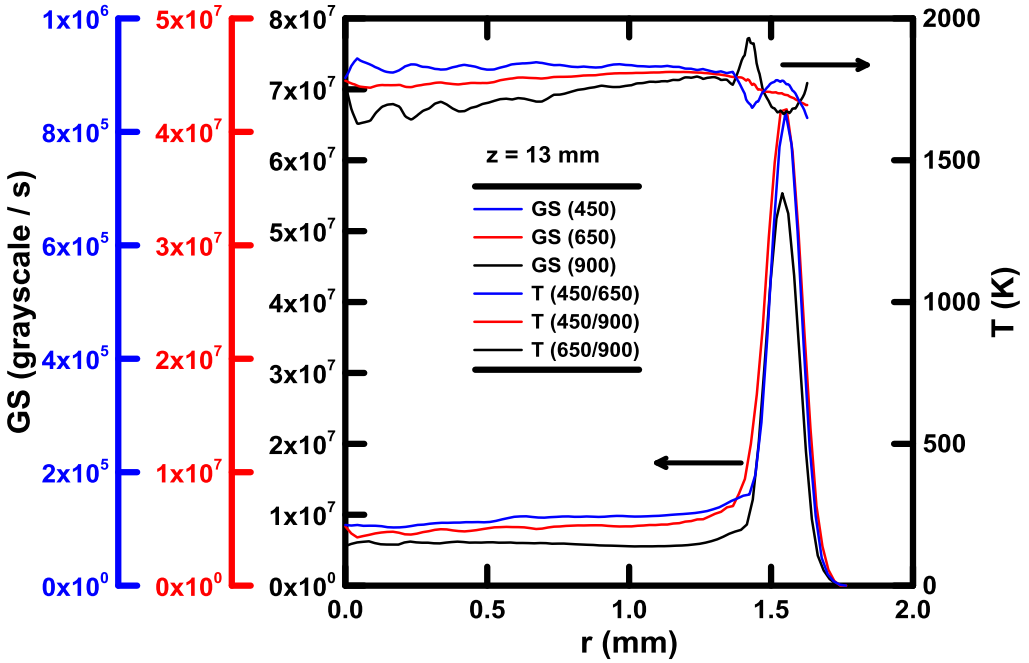

Figure 4-4 Deconvolved Grayscales for each filter and the determined temperatures for each filter pair, at z = 13 mm.

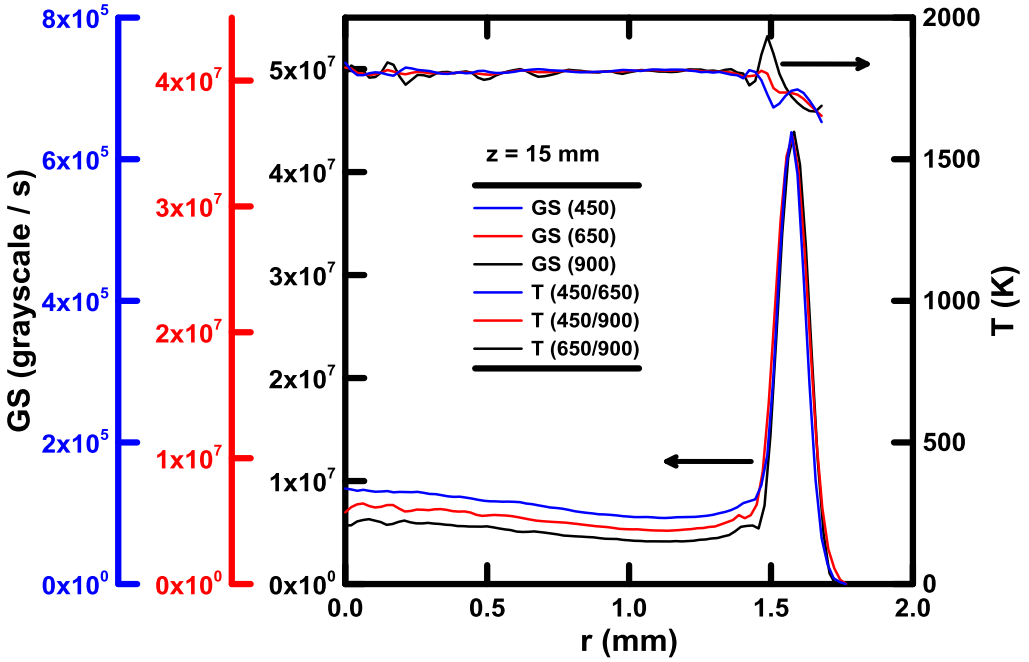

Figure 4-5 Deconvolved Grayscales for each filter and the determined temperatures for each filter pair, at z = 15 mm.

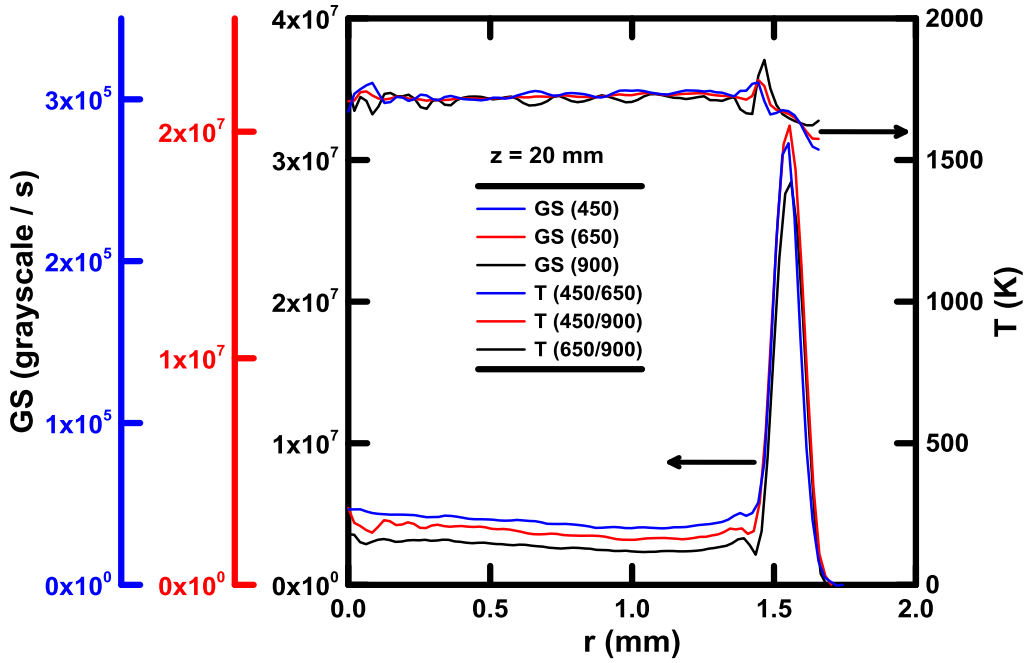

Figure 4-6 Deconvolved Grayscales for each filter and the determined temperatures for each filter pair, at z = 20 mm.

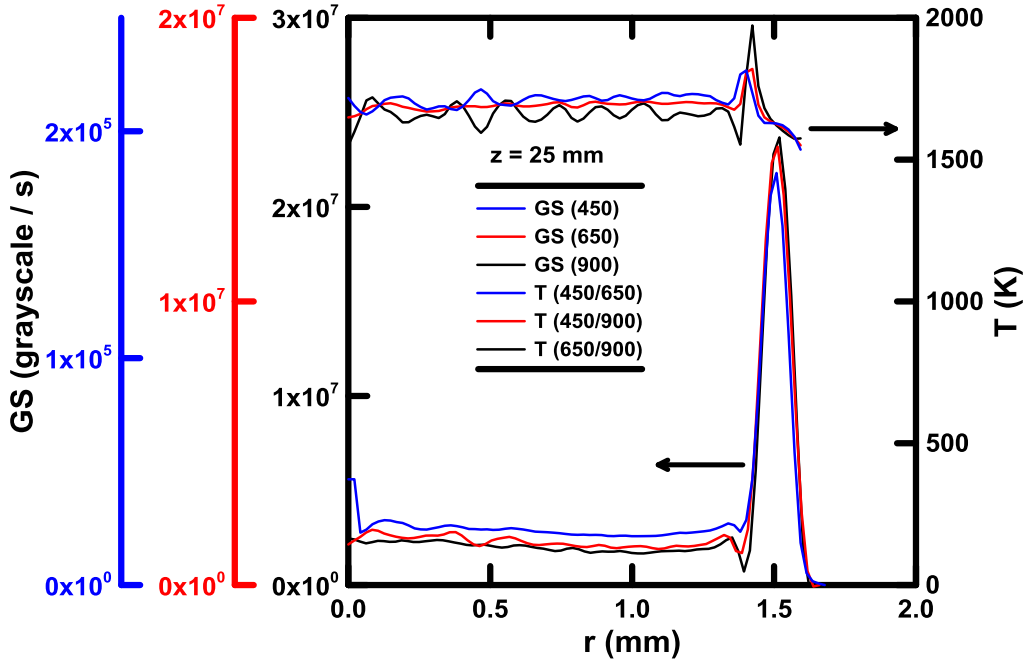

Figure 4-7 Deconvolved Grayscales for each filter and the determined temperatures for each filter pair, at z = 25 mm.

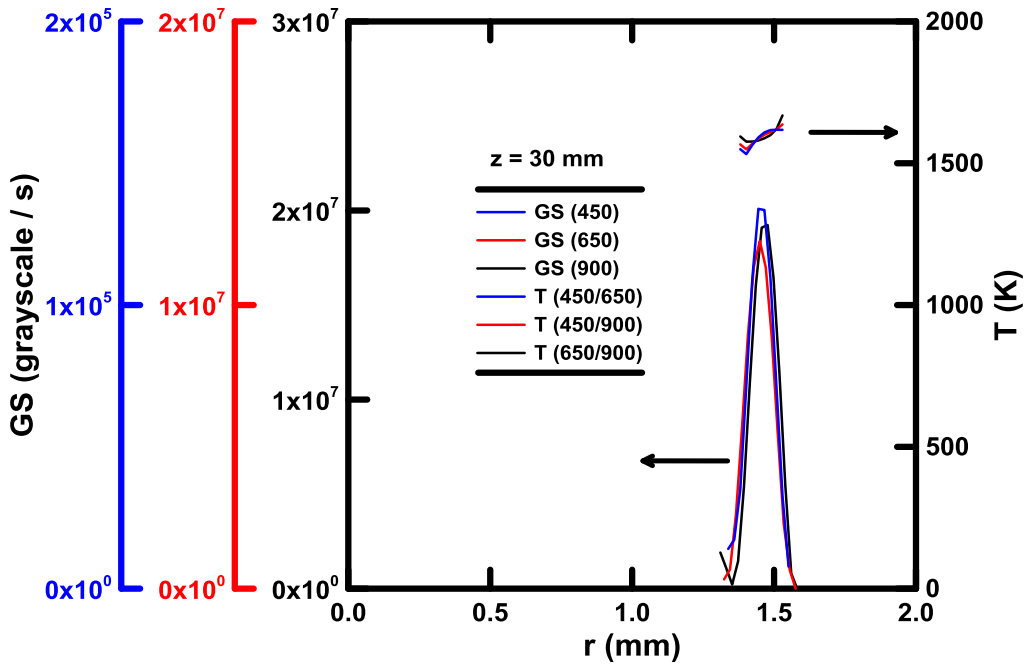

Figure 4-8 Deconvolved Grayscales for each filter and the determined temperatures for each filter pair, at z = 30 mm.

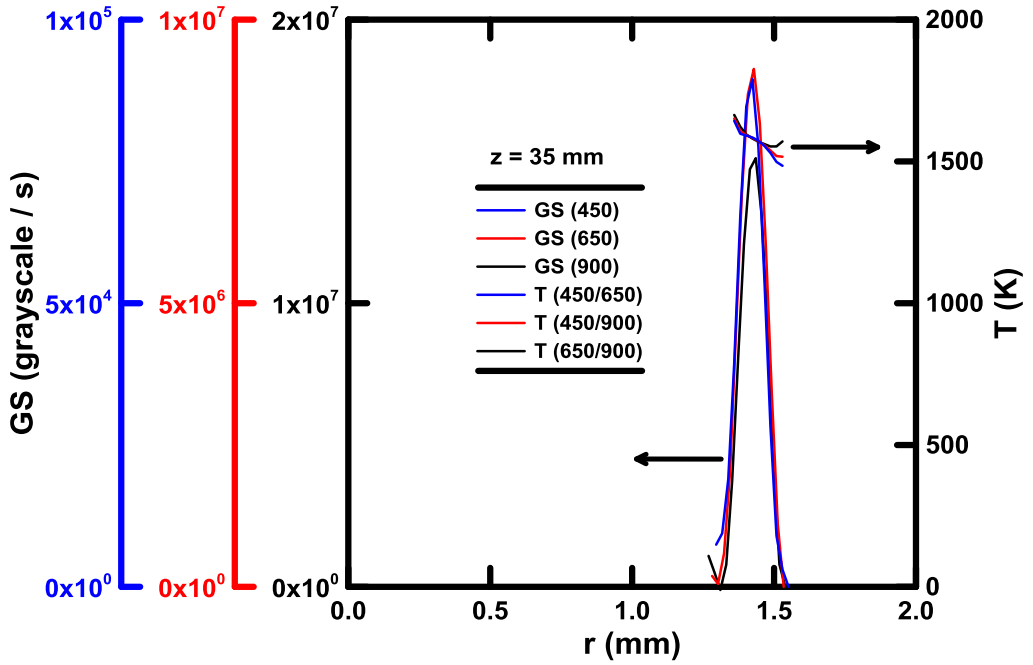

Figure 4-9 Deconvolved Grayscales for each filter and the determined temperatures for each filter pair, at z = 35 mm.

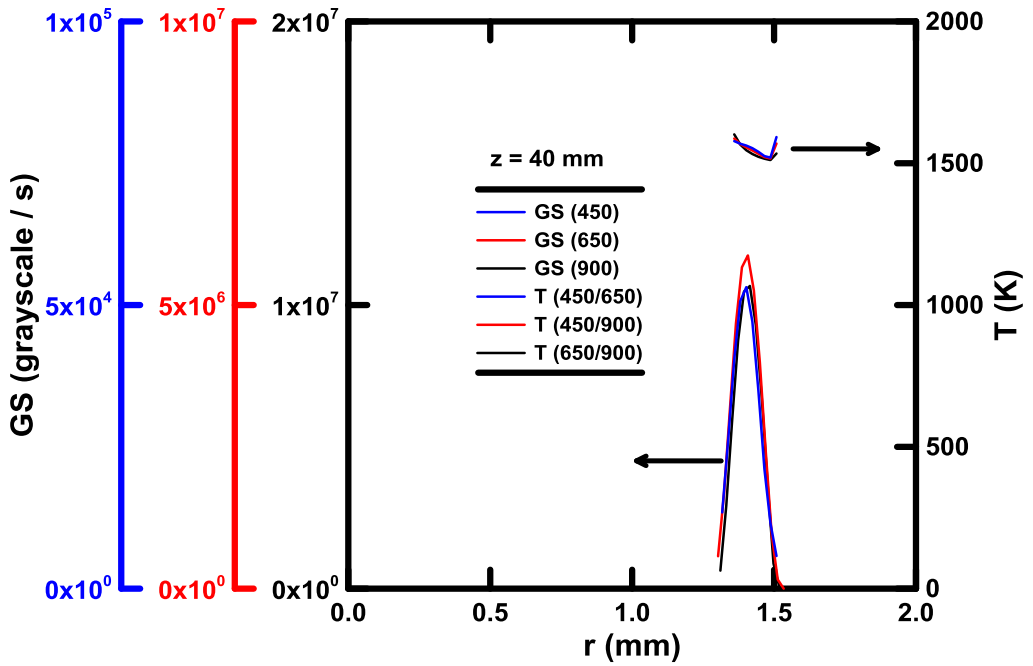

Figure 4-10 Deconvolved Grayscales for each filter and the determined temperatures for each filter pair, at z = 40 mm.

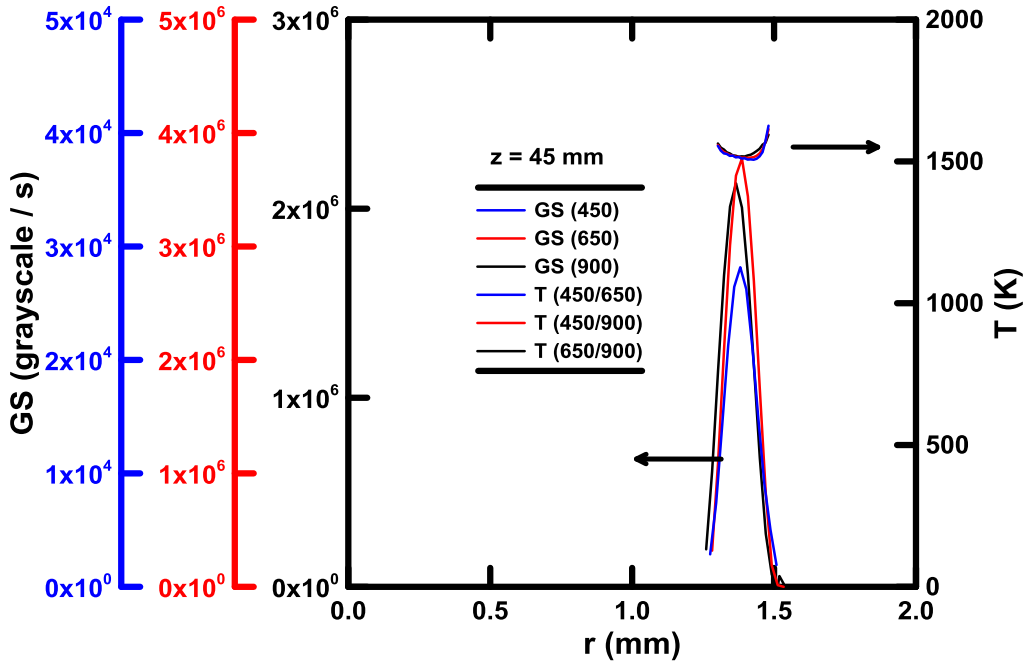

Figure 4-11 Deconvolved Grayscales for each filter and the determined temperatures for each filter pair, at z = 45 mm.

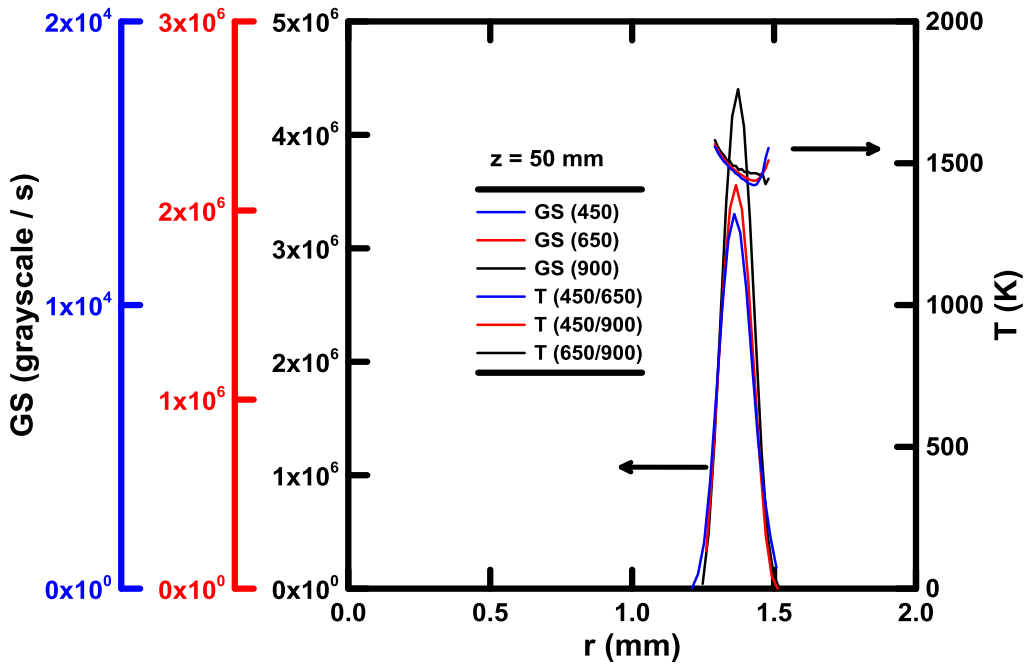

Figure 4-12 Deconvolved Grayscales for each filter and the determined temperatures for each filter pair, at z = 50 mm.

4.1.2. *Soot Volume Fraction Experimental*

For the ternary flame system, soot concentrations were measured using laser extinction, with setups similar to that in measuring the reference flame soot volume fraction. A 7 mW He-Ne laser operating at 632.8 nm was used as the light source. A soot refractive index of $m = 1.57 - 0.56\,i$ was used [73], and analysis of laser extinction measurements assumed that the soot satisfied the Rayleigh scattering approximation.

In preliminary flames (1) and (2) in Fig. 2-5, the centerline soot volume fraction is found to increase with height above 20 mm height (Appendix). The soot flux calculated with the sectional integrated soot volume fraction, however, continuously decreases with height, suggesting soot oxidation. While this ternary flame design successfully avoids the soot formation; the increase of centerline soot volume fraction is possibly caused by the

narrowing of the soot column, due to thermophoresis. It is therefore postulated that, if the radial soot transportation is significant, the integrated soot volume fraction is a more accurate indicator than the centerline soot volume fraction for calculating the oxidation rate.

In this study, the sectional integrated soot volume fraction (F_s), defined as $F_s = \int_{-R}^{R} \pi r f_s(r) dr$ at each height is used instead of the local soot volume fraction (f_s). F_s is determined from Eq. (4-1) to avoid the noises accumulated in deconvolution.

$$F_s = \lambda \left\{ \int_{-R}^{R} \ln\left[GS^0(x) / GS(x) \right] dx \right\} / 6\pi E(m), \tag{4-1}$$

where $E(m)$ is the refractive index absorption function, GS(x) is the grayscale indicated by the camera divided by the shutter time, r is the radius, R is the flame radius, x is the horizontal coordinates in the object plane, and λ is the laser wavelength. Superscript 0 denotes the reference image. F_s can be directly calculated without knowing f_s. For flames with small diameters, this integration method was able to obtain the global soot concentration, avoiding possible soot transport in the radial direction. In addition, this integration method does not request the axisymmetric assumption. The uncertainty was estimated to be better than ±5% (95% confidence) for F_s higher than 3×10^{-5} mm^2 (below 30 mm height), and better than ±10% (95% confidence) for the rest regions. Spatial resolution in the object plane was 34 μm, and the shutter time was 167 ms.

The following steps showed the detailed derivations of Eq. (4-1). The derivation is in the Cartesian coordinate so that axisymmetric is not required. From definition, the integrated soot volume fraction is:

$$F_s = \int_{-\infty}^{\infty}\int_{-\infty}^{\infty} f_s(x,y)dxdy\,. \tag{4-2}$$

For soot in any element volume, the soot volume fraction is assumed to be constant. Therefore, within the *i*-th element volume along the *y* direction, the extinction of incident light along the *y* direction can be expressed in the following equation:

$$\ln\left[\frac{I^{in}(x,i)}{I^{tr}(x,i)}\right] = \frac{6\pi E(m)}{\lambda} f_s(x,y,i)dy\,, \tag{4-3}$$

where superscript "*in*" and "*tr*" denote the incident and transmitted light intensity, respectively. The transmitted light intensity for the element *i* equals the incident light intensity for the next element, $i + 1$. Therefore, integrating Eq. (4-3) can be simply achieved by summing all the element volumes.

$$\int_{-\infty}^{\infty}\int_{-\infty}^{\infty} \frac{6\pi E(m)}{\lambda} f_s(x,y)dxdy = \int_{-\infty}^{\infty}\left[\sum_{i=1}^{N}\frac{6\pi E(m)}{\lambda} f_s(x,y,i)dy\right]dx = \int_{-\infty}^{\infty}\sum_{i=1}^{N}\ln\left[\frac{I^{in}(x,i)}{I^{tr}(x,i)}\right]dx\,. \tag{4-4}$$

And, because there is:

$$\sum_{i=1}^{N}\ln\left[\frac{I^{in}(x,i)}{I^{tr}(x,i)}\right] = \ln\left[\frac{I^{0}(x)}{I(x)}\right]. \tag{4-5}$$

Combining Eqs. (4-4) and (4-5) yields:

$$\int_{-\infty}^{\infty}\int_{-\infty}^{\infty} \frac{6\pi E(m)}{\lambda} f_s(x,y)dxdy = \int_{-\infty}^{\infty}\ln\left[\frac{I^{0}(x)}{I(x)}\right]dx\,. \tag{4-6}$$

Rearranging and replacing the light intensity with the sensor detected grayscale GS yield the exact expression for the integrated soot volume fraction as shown in Eq. (4-1). Since the derivation was performed in an ordinary Cartesian coordinate, Equation (4-1) can also be used in any asymmetric flames.

The laser extinction image is also shown in Fig. 4-2. The image is linearly saturation enhanced. In the soot flame measurement, the extinction is much higher than the laser background noise level, as indicated in Fig. 4-13 and 4-14. Therefore, GS^0 signal was approximated by linearly interpolating the grayscales in the soot free region in the "laser on flame on" image. This method further simplifies the laser extinction measurement with just one image. Figure 4-13 to 4-15 show the measured grayscales from the "laser on flame on" image, the interpolated laser background grayscales, and the signal ratio (GS^0 / GS), at representative heights of 10, 35, and 55 mm. The ratios from the left were flipped to the right side, supporting the axisymmetric assumption. The averaged ratios were then integrated with Eq. (4-1) to obtain the integrated soot volume fraction. Replications were taken with 14 images and the averaged values were used.

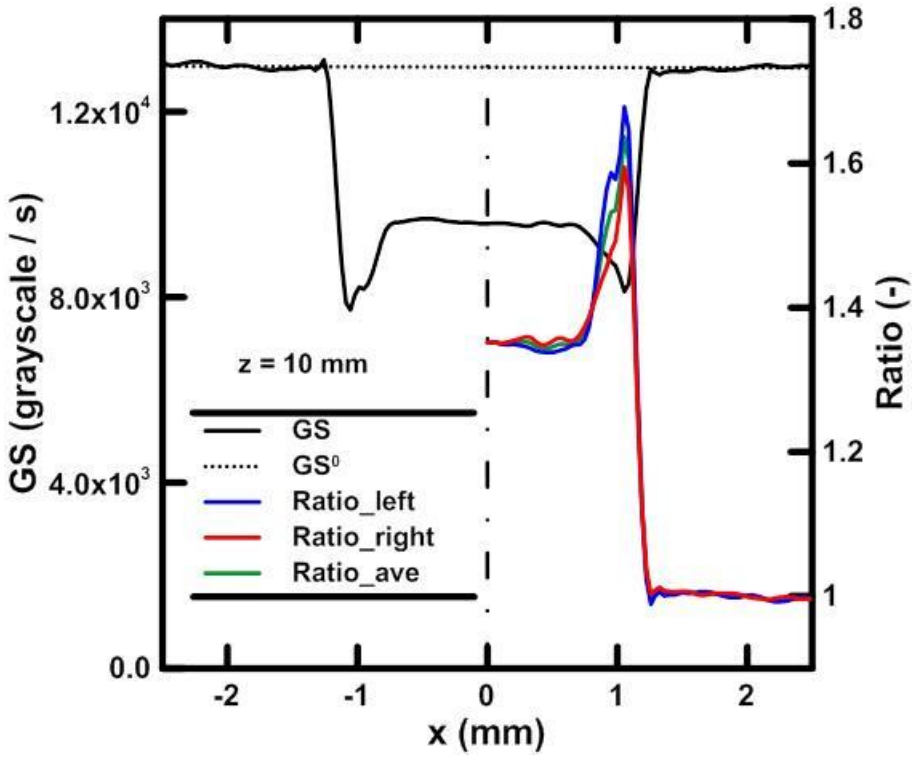

Figure 4-13 Laser extinction grayscales and the signal ratio GS^0 / GS at z = 10 mm.

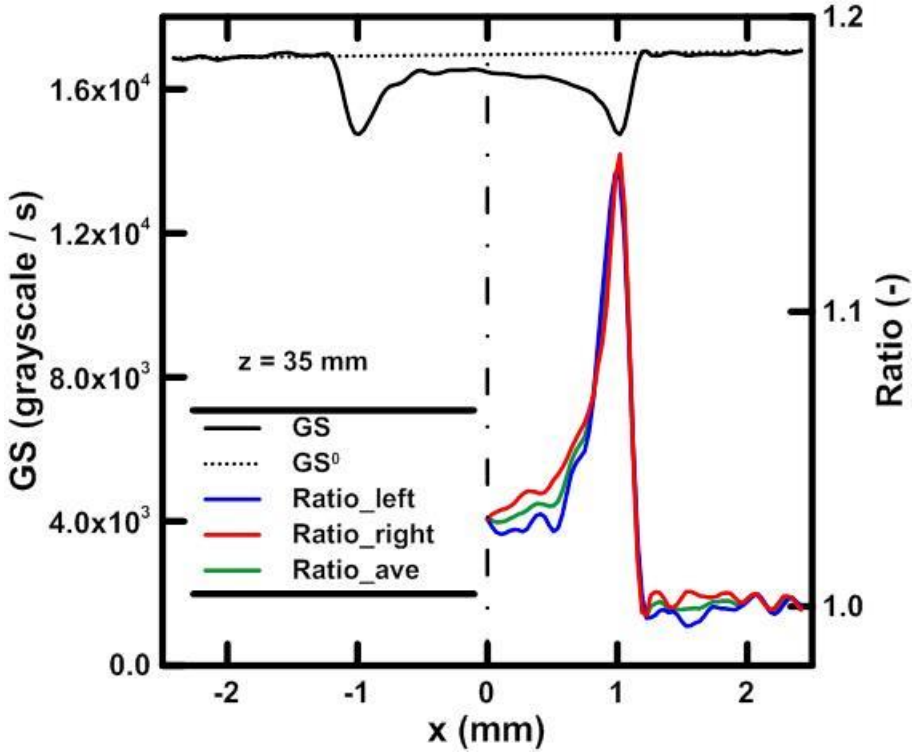

Figure 4-14 Laser extinction grayscales and the signal ratio GS^0 / GS at z = 35 mm.

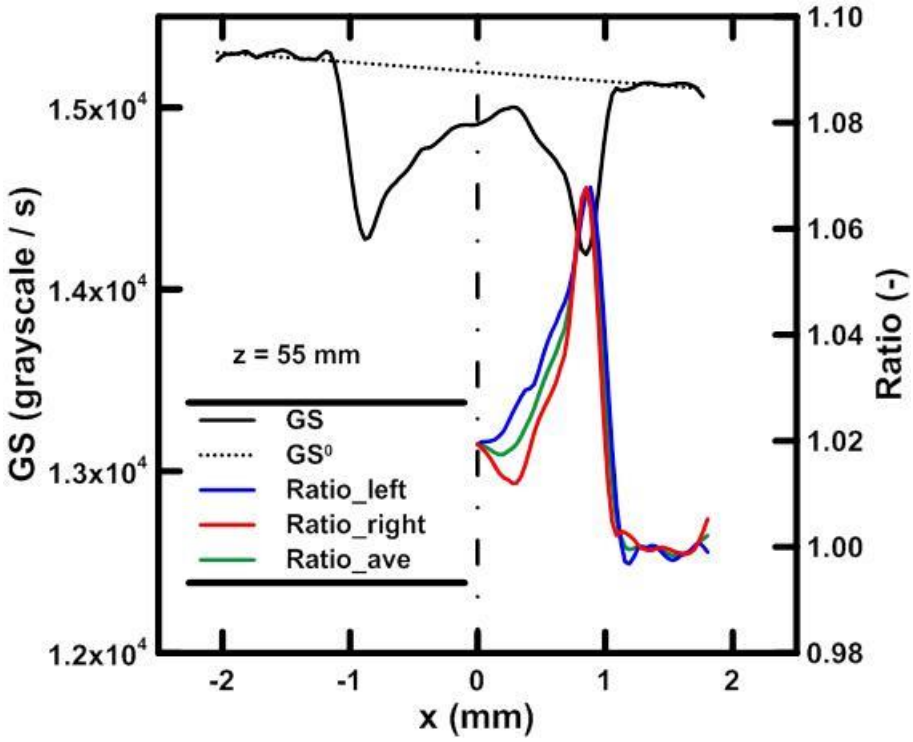

Figure 4-15 Laser extinction grayscales and the signal ratio GS^0 / GS at z = 55 mm.

4.1.3. Soot Temperature and Soot Volume Fraction Results

Figure 4-16 shows the radially resolved temperatures and soot volume fractions at representative heights of 13, 30, and 45 mm. Soot temperature is nearly uniform in the radial direction, with a maximum difference of 150 K. Temperature decreases at locations where soot concentration peaks, due to radiative heat loss. Above 45 mm, temperatures at the inner radius were not obtained due to insufficient soot, as discussed in Ref. [77]. The soot flame was hollow with soot concentrated at outer radius, as shown in the three representative heights in Fig. 4-16. At z = 13 mm, soot volume fractions at inner radius (< 0.7 mm) are not shown due to the accumulated laser background noises from the Abel deconvolution using Eq. (3-11). Above 15 mm height, soot volume fractions near the centerline are negligible.

Figure 4-17 shows the measured temperatures versus height. The temperature at each height was calculated by averaging the radially resolved temperatures within regions where soot concentration peaked (above half of local maximum). The average value represents the temperature at which most of the soot oxidation occurred at each height. Temperatures are between 1500 – 1725 K. Temperature peaks at 13 mm height which coincides with the maximum flame diameter location. Above, the temperature decreases with height when away from the hydrogen flame. The temperature is significantly lower than that in a hydrogen only flame (about 2000 K).

Temperatures in the hydrogen only flame were measured with thin filament pyrometry following Ref. [57]. SiC fibers with diameters of 13.9 μm were used.

Radiation corrections were performed with an filament emissivity of 0.88 [65]. Gas velocities were estimated to be the same as the measured soot flame velocity.

The cooler soot column (enriched with air) from the lower hydrocarbon flame affects the hydrogen flame by: changing the local stoichiometric condition; and cooling the local reaction zone (from convection and soot radiation).

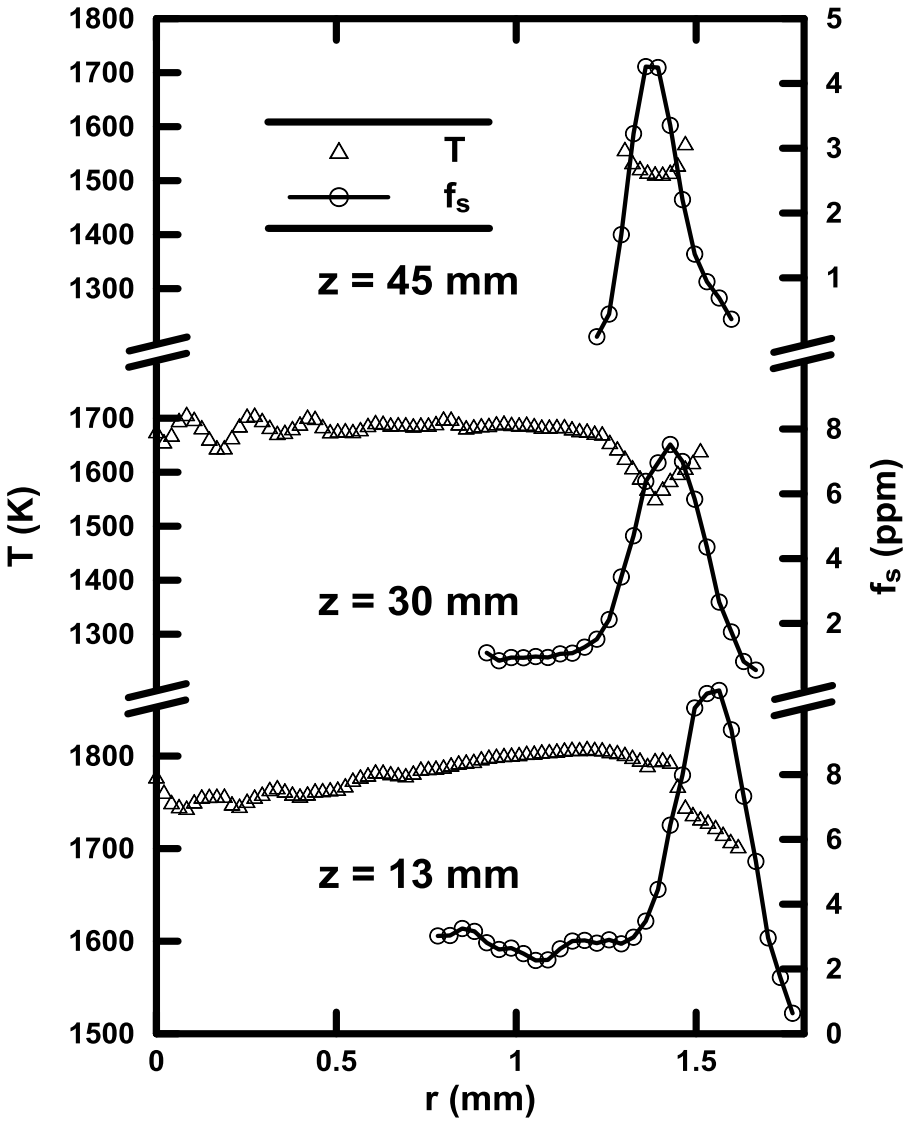

Figure 4-16 Measured temperatures and soot volume fractions versus radius at heights of 13, 30 and 45 mm.

Figure 4-17 also shows the integrated soot volume fractions using Eq. (4-1) versus height, with an increment of 1 mm. F_s continuously decreased with height owing to oxidation. Above 55 mm height, the laser extinction and the laser background noises are at the same level, and the results are not reported. F_s was measured between 10 – 120 $\times 10^{-6}$ mm^2. Normalized by the flame sectional area yields averaged soot volume fractions between 1 – 15 ppm.

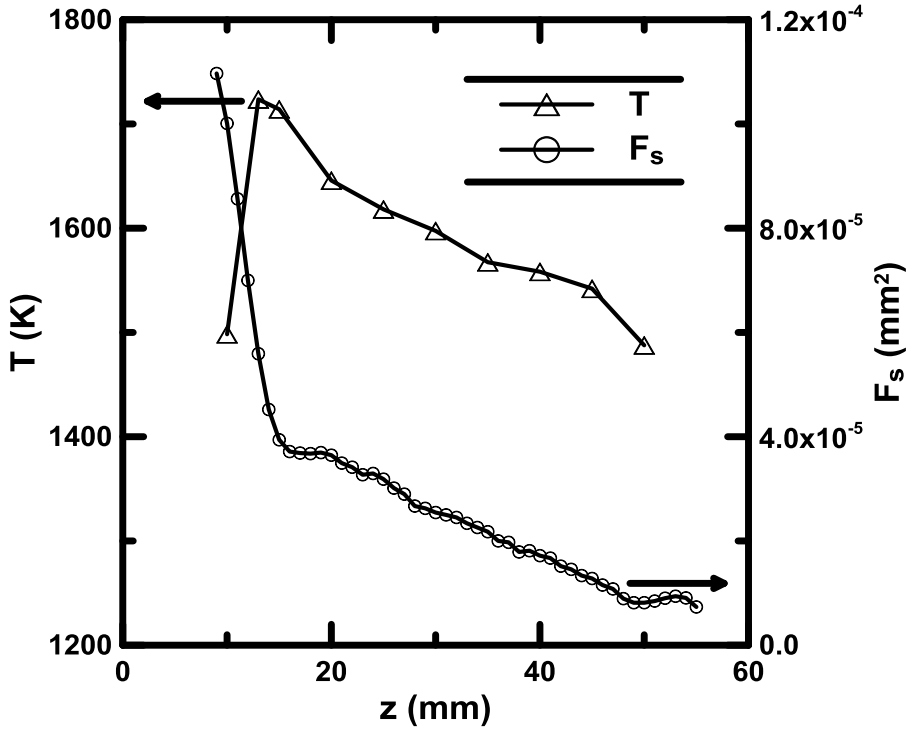

Figure 4-17 Measured temperatures and integrated soot volume fractions versus height.

4.2. Axial Velocity

4.2.1. Axial Velocity Experimental

The velocity of the soot flame is not expected to vary over its narrow 2.5 – 3.3 mm width. Soot particles are expected to follow the local gas velocities which are sufficiently high here to dominate over any thermophoresis in the axial direction. Axial

velocities were measured by momentarily passing a metal rod with a rectangular profile (2.80 × 0.66 mm) through the soot column for 2 ms at 35 mm above the propylene fuel port and recording the motion of the interruption with a high speed video camera (Casio EX-FH100). The camera recorded at a rate of 420 frames/s, with a spatial resolution of 0.45 mm. Velocities were determined from the mean of the leading and trailing edges of the interruption with an estimated uncertainty of ±5% (95% confidence).

4.2.2. Axial Velocity Results

Figure 4-18 shows the measured axial flame velocity. Velocities were measured at heights between 20 – 100 mm for a better coefficient of determination. A linear fit is shown in Fig. 4-18, which has a R^2 of 0.96. Velocities were measured between 2 – 3 m/s. Velocities increase with height owing to buoyancy.

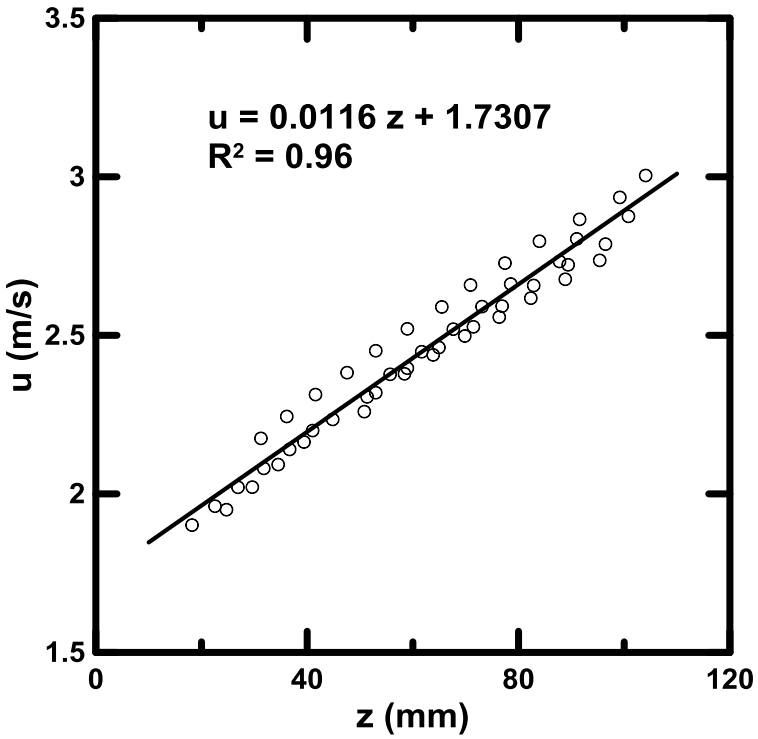

Figure 4-18 Measured flame axial velocities versus height.

4.3. Soot Primary Particle Diameter

4.3.1. Soot Primary Particle Diameter Experimental

Soot samples were obtained using thermophoretic sampling and were analyzed using TEM similar to previous studies [47, 78, 79]. To determine primary particle size distribution, a program employing a Hough transform algorithm similar to Ref. [80] was developed. The program identified likely primary particles in the TEM images which were then manually inspected to eliminate falsely identified primary particles. The uncertainty was estimated to be ±10% (95% confidence).

4.3.2. Soot Primary Particle Diameter Results

Figure 4-19 presents the TME images of soot aggregates at representative heights of 10 and 40 mm. Roughly spherical soot particles agglomerate in clusters or chains. Soot particles were found to be merely touched or overlapped with narrowed bridges. It was recognized that the overlapping sacrifices the soot surface area by roughly 0 – 20%. Corrections will not be attempted here due to the uncertainty in overlapping estimation. Soot particles are assumed to be merely touched.

For each height, 200 – 3500 soot particles were examined, depending on the available agglomerate size. The resulting size distributions approach a normal or lognormal shape. Here, a lognormal distribution was assumed due to the high variance in particle diameter (standard deviation of about 10 nm). Figure 4-20 shows the measured geometric mean soot particle diameter. Diameters were measured between 20 – 45 nm. Diameter decreases with height because of oxidation.

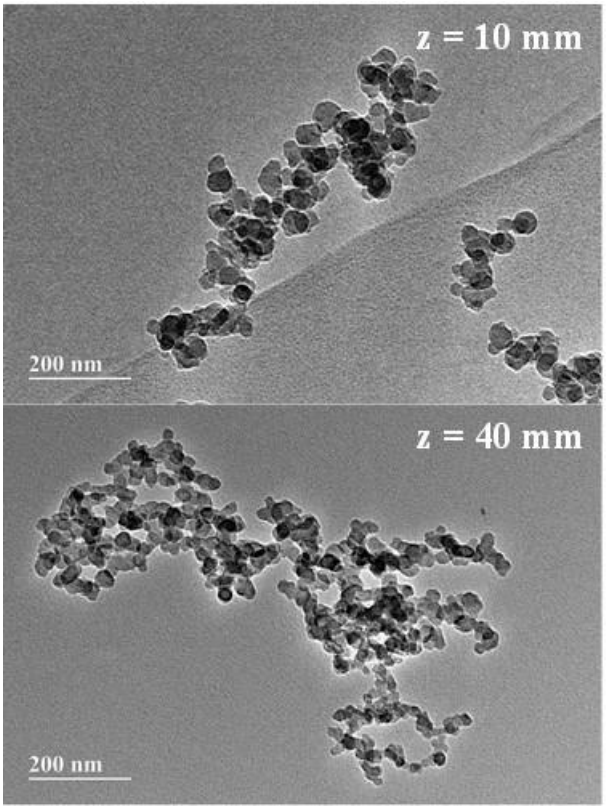

Figure 4-19 Typical TEM images of soot aggregates at heights of 10 and 40 mm.

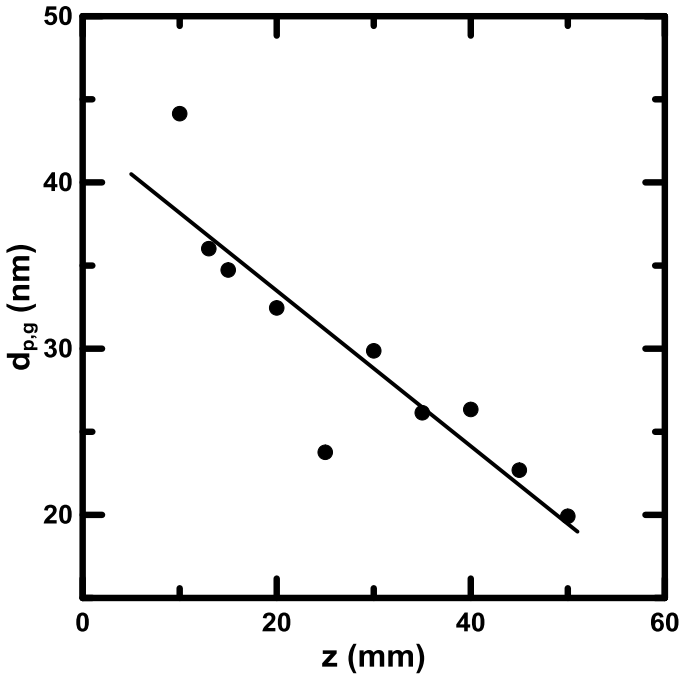

Figure 4-20 Measured soot primary particle diameters versus height.

4.4. Major Species Concentration

4.4.1. Major Species Concentration Experimental

Major gas compositions (H_2, O_2, N_2, CO, CO_2, and H_2O) were measured by isokinetic sampling, similar to [47-49], and analyzed with desiccant gravimetry for water vapor, and with GC for other stable species.

A stainless steel radiatively cooled sampling probe was used, having a port diameter of 2.1 mm. The isokinetic sampling condition was maintained with a vacuum pump, a manual metering valve and a rotameter calibrated with soap bubble meter. The sampling flow rate was first estimated from the measured axial velocity and the probe inner sectional area, such that the downstream velocity through the probe is the same as the gas velocity at the sampling location. In this step, it was assumed there is no water absorption in the water trap, and the mass flow rate through the probe equals to the mass flow rate through the rotameter.

The flow rate was then corrected for the temperature difference between the flame and the rotameter, assuming ideal gas law. Sampled gas was cooled to the ambient temperature at the rotameter. It is noted that since the composition of the sampled gas varies with the sampling location; the response of the rotameter to the actual flow rate also varies. The rotameter calibration was therefore performed with N_2 (99.999% purity), N_2/O_2 mixture (79.5%/20.5%), and $N_2/CO_2/CO$ mixture (78.0%/20.1%/1.9%), respectively. The calibration gas mixtures were chosen to generally cover the gas composition range in the current flame system, as determined from some preliminary tests. Effect of H_2 (estimated $< 0.6\%$ of sample gas on dry basis) is negligible. The

calibration results were consistent within 6%, as shown in Fig. 4-21. Also shown are the calibration results of pure H_2 and the calibration curve for N_2 from manufacturer. The rotameter for sampling can be taken as insensitive to composition variance in the current flame system. N_2 (estimated > 80% of the sample gas on dry basis) calibration results were used for rotameter.

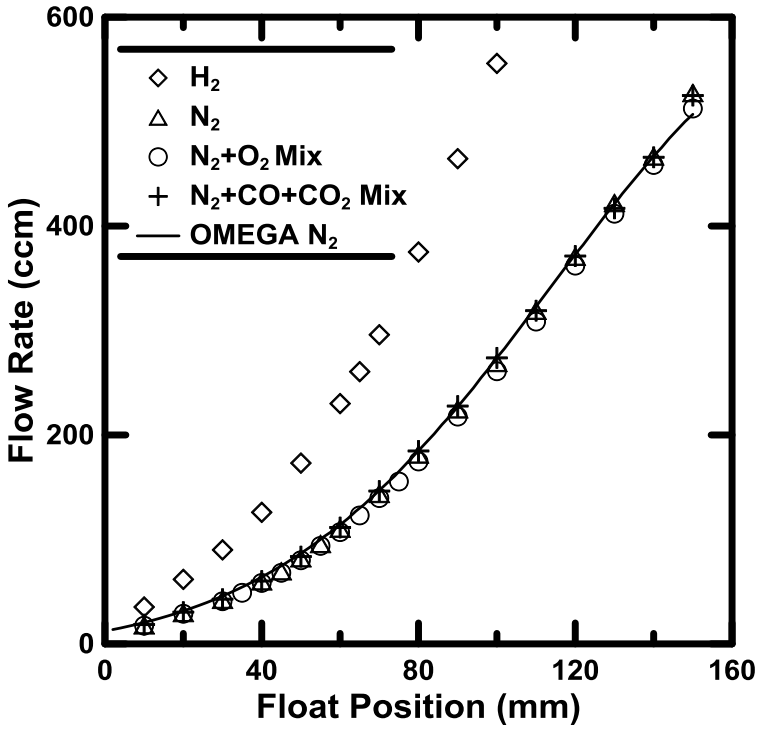

Figure 4-21 Rotameter calibration with N_2+CO+CO_2 mixture, pure N_2, air, and pure H_2, using a soap bubble meter. Also shown is the calibration curve for N_2 provided by the manufacturer.

For H_2O, the gas samples were passed through a brass tube (12 cm in length and 1.1 cm in inner diameter) filled with glass wools to remove soot. The brass tube is heated above 100 ℃ to avoid water condensation. The gas samples were then passed through a U-shape stainless steel water trap (23 cm in length and 0.4 cm in inner diameter) filled with drierites (calcium sulfate, >98; cobalt chloride, <2%). The water trap was water-

cooled to avoid overheating of the drierites. Gaseous products were sampled for 30 min with a vacuum pump, and the weight increase of the desiccant was determined gravimetrically using a micro-balance (Mettler Toledo, MS4002S) with an accuracy of 0.01 g. H_2O concentration was determined from the weight increase of the desiccant, the sampling flow rate, and the sampling time.

It is noted that the actual mass flow rate through the probe equals to the mass flow rate through the rotameter, plus the mass of water absorbed by the desiccant per unit time. The flow rate was therefore also corrected for the water trap effect, with the measured water concentration. The experiments were repeated with the updated isokinetic condition for water measurement, until the results converged. The sampling system diagram for water measurement is shown in Fig. 4-22. The uncertainty was estimated to be ±10% (95% confidence). The updated isokinetic condition was used for GC sampling.

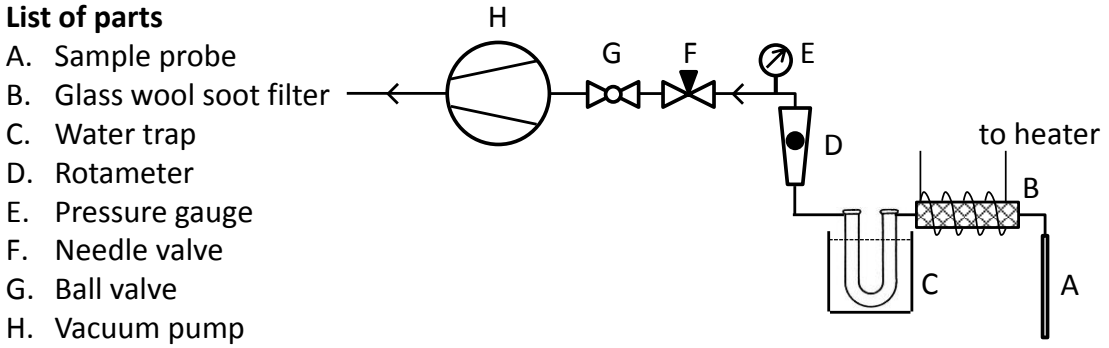

Figure 4-22 Sampling system diagram for water measurement.

For other major species, a PTFE membrane soot filter (Gelman 66143) with pore size of 0.2 μm was used to replace the glass wool soot filter, for GC compatibility. A water filter (7 cm length and 1 cm inner diameter) filled with indicating drierites was used to remove water in the sampling stream. The amount of drierites is minimized in GC

measurements as it absorbs small amount of CO and CO_2. The absorption effect is found to be negligible after saturation. Gas samples flowed through a 10 μL sample loop and the injection was controlled with a 6-port sample valve. Details of the GC sampling setup are shown in Fig. 4-23. At the isokinetic sampling condition, the small diameter (< 0.2 mm) of the sample loop causes significant pressure drop, which in turn affects the rotameter condition. The pressure drop through the loop was therefore compensated with a bypass line in parallel. Allocation of the flowrate through the sample loop and the bypass line was achieved with a needle valve (E). In the sample position in Fig. 4-23(a), gas samples flew through the sample loop and exhaust from the vacuum pump. And the carrier gas flew through the GC. Valve (E) was set fully open prior to injection in order to balance the pressure. After the 6-port valve switched to the inject position, as shown in Fig. 4-23(b), the carrier gas blew the gas samples resided in the sample loop to the GC.

A GC (Hewlett-Packard 5890) with a thermal conductivity detector (TCD), and a capillary column (Supelco Carboxen 1010) with a length of 30 m and an inner diameter of 0.53 mm, similar to Ref. [81], were used to analyze the gas samples. Helium (99.9995% purity) was used as the carrier gas for O_2, N_2, CO, and CO_2. Argon (99.9995% purity) was used as the carrier gas for H_2 due to similar thermal conductivity between helium and hydrogen. The GC parameters were set as follows: carrier gas (He or Ar) at 3 mL/min, initial oven temperature of 35 ℃, initial holding time of 8.5 min, heating rate of 24 ℃/min, final temperature of 200 ℃, and final holding time of 4 min.

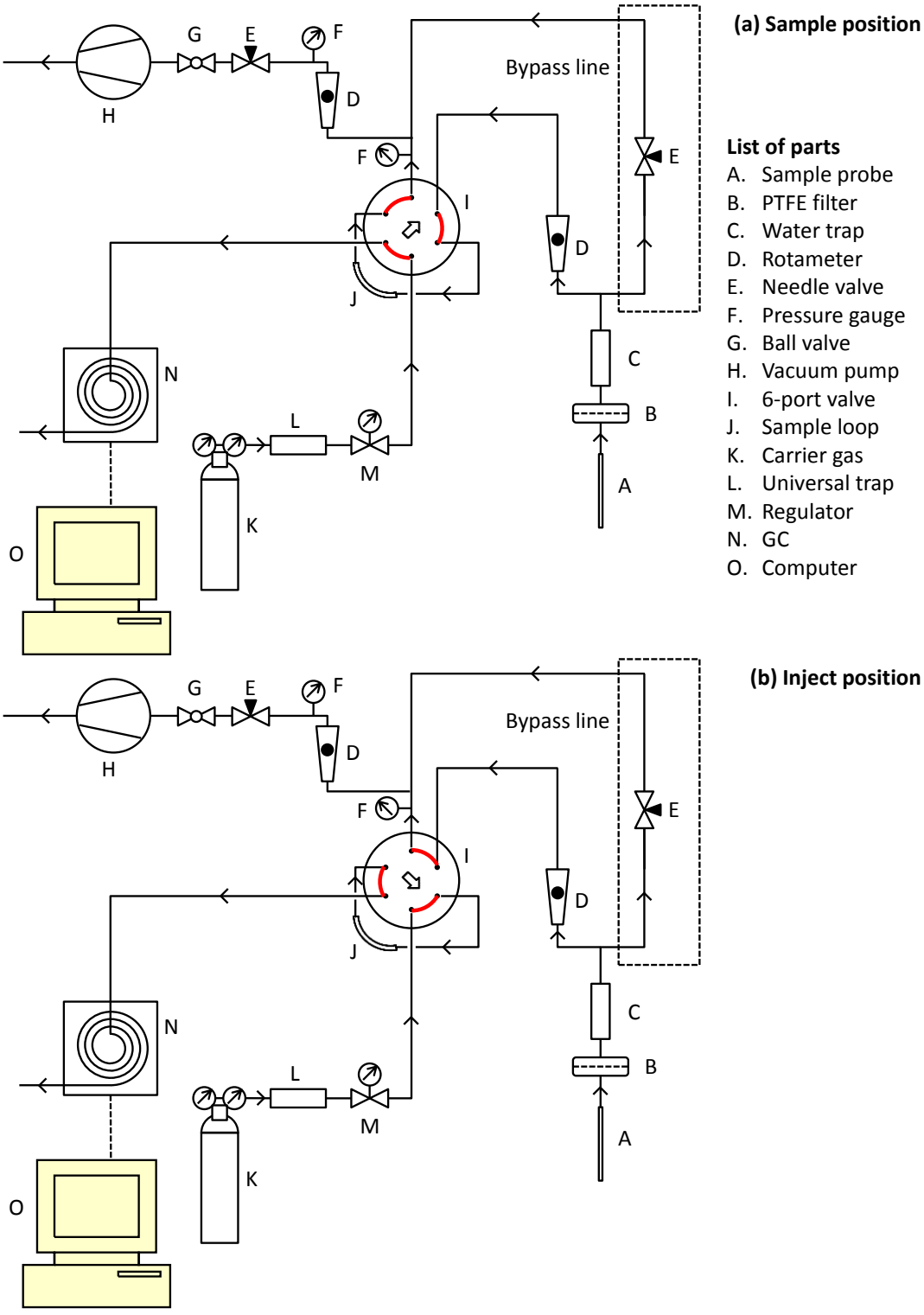

Figure 4-23 Sampling system for GC measurement with a 6-port sample vale: (a) sample position, (b) inject position.

The relative concentration of each gaseous compound was calculated by firstly integrating the signal peak area above the baseline and then calibrating the GC with different volumes of gas mixture (Air Liquide). The coefficients of determination (R^2) for calibrations are above 0.99. Gaseous products were sampled for 10 min with a vacuum pump. The species concentration was corrected for the difference in loop pressure between calibration and test (< 0.5 psi). The uncertainty was estimated to be ±10% (95% confidence).

Detailed calibration results as well as the selected calibration gases were shown in Appendix. Figure 4-24 shows one GC calibration results (helium carrier gas) with calibration species concentration of 5% each in helium balance. The gas species was determined from its characteristic retention time. With the current GC methods, the resulting GC retention time is shown in Table 4-1.

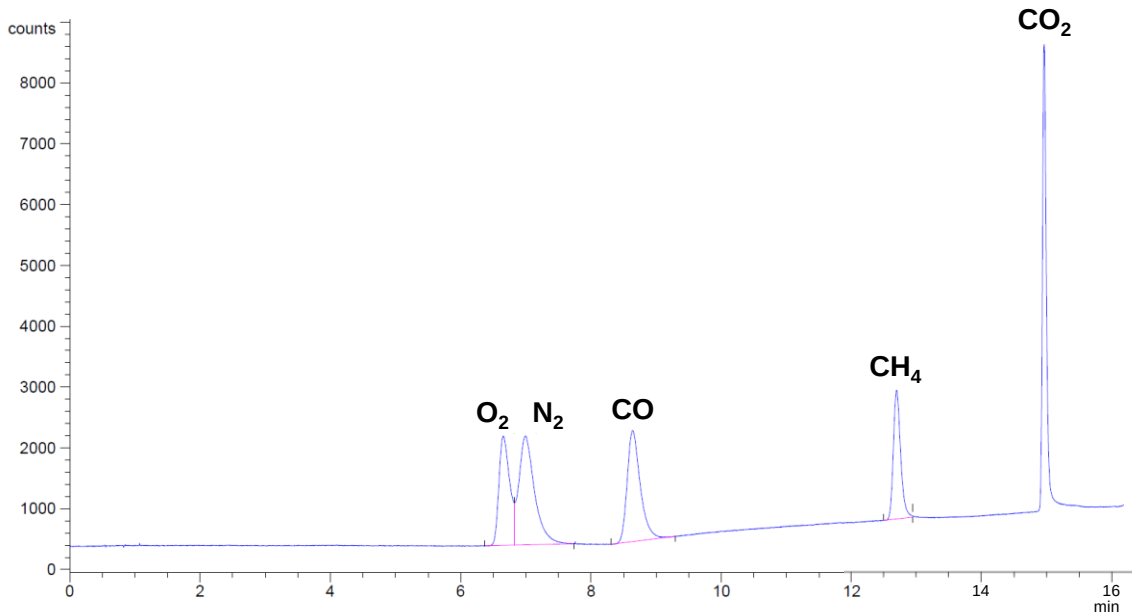

Figure 4-24 GC calibration with species concentration of 5% each in helium balance.

Table 4-1 Retention time for the selected species with the chosen GC methods.

Species	Ret. Time (min)
H_2	4.7
O_2	6.6
N_2	7.0
CO	8.6
CH_4	12.7
CO_2	14.9

4.4.2. Major Species Concentration Results

Figure 4-25 shows the measured major species concentration versus height. N_2 concentrations are nearly constant with height, ranging between 65 – 75%. O_2 are between 0.8 – 10%. O_2 concentration peaks at 10 mm owing to entrainment from the lower propylene/air flame. This was verified with a H_2 only flame, where O_2 concentration at the same location was found lower than 1%. O_2 concentration decreases with height up to 20 mm, owing to oxidation. Above, O_2 concentration increases with height when away from the H_2 flame zone. H_2O increases with height and peaks at 30 mm with a concentration of 26%. It decreases thereafter due to diffusion. CO_2, CO, and H_2 concentrations show similar pattern. The concentrations peak between 15 – 20 mm. At heights below 15 mm and above 30 mm height, the H_2 signal and the baseline noises are at the same level and the concentrations (estimated < 0.1% on the dry basis) are not reported.

The ratio of measured O atom versus N atom was shown in Fig. 4-26. Species measurement uncertainty of 10% was assumed for the error bar calculation. Since in the current flame system, air is the only source for O and N atom, the O/N ratio from the

measured species concentration is expected to be conserved. The dashed line indicates the ideal O/N ratio in air. Figure 4-26 was used as a quick check for the GC measurement.

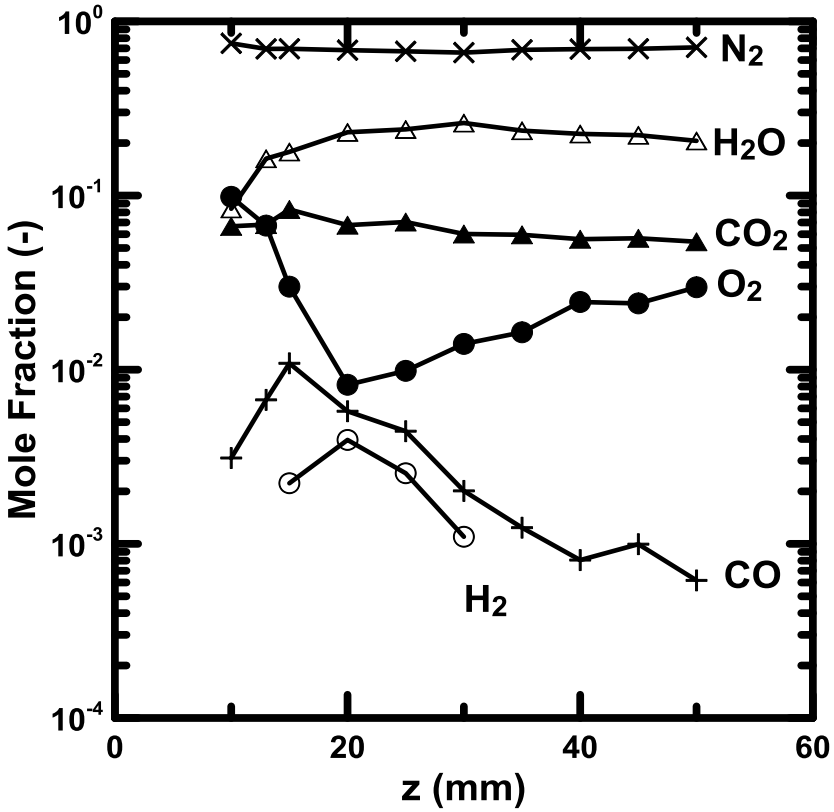

Figure 4-25 Measured stable species concentrations versus height.

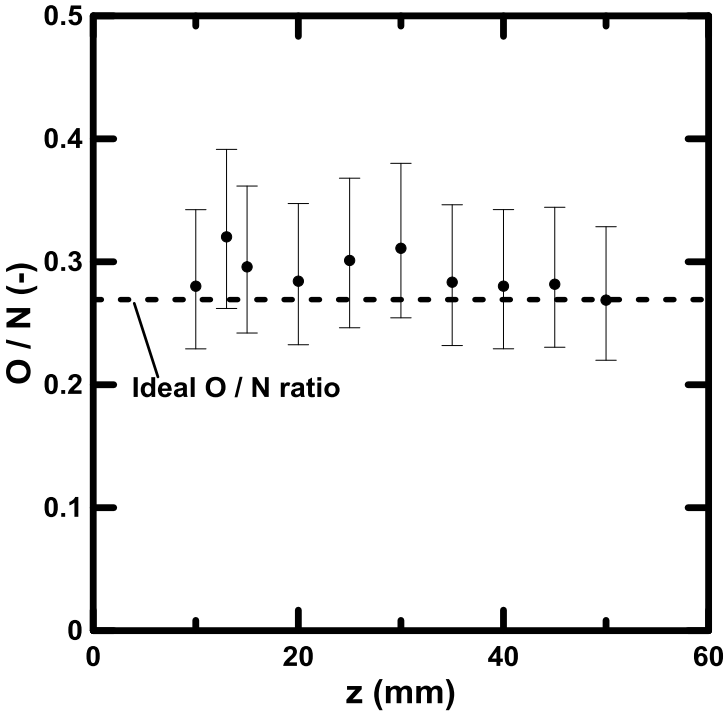

Figure 4-26 O/N atom ratio versus height determined from the measured species concentration.

The stoichiometric condition in the soot flame was determined from the local equivalence ratio (Φ), which is defined as the ratio of the stoichiometric number of O atoms to the actual number of O atoms available (assuming that all the final products are CO_2 and H_2O) [82, 83]. The calculated local equivalence ratio using Eq. (4-7) was shown in Fig. 4-27.

$$\Phi = \frac{H_2 + 2CO_2 + 2CO + H_2O}{2O_2 + 2CO_2 + CO + H_2O} \tag{4-7}$$

The current soot flame was found to be lean at all heights. The local equivalence ratio is between 0.54 – 0.98. The leanest location is at 10 mm height where the O_2 concentration is the highest, due to the entrainment.

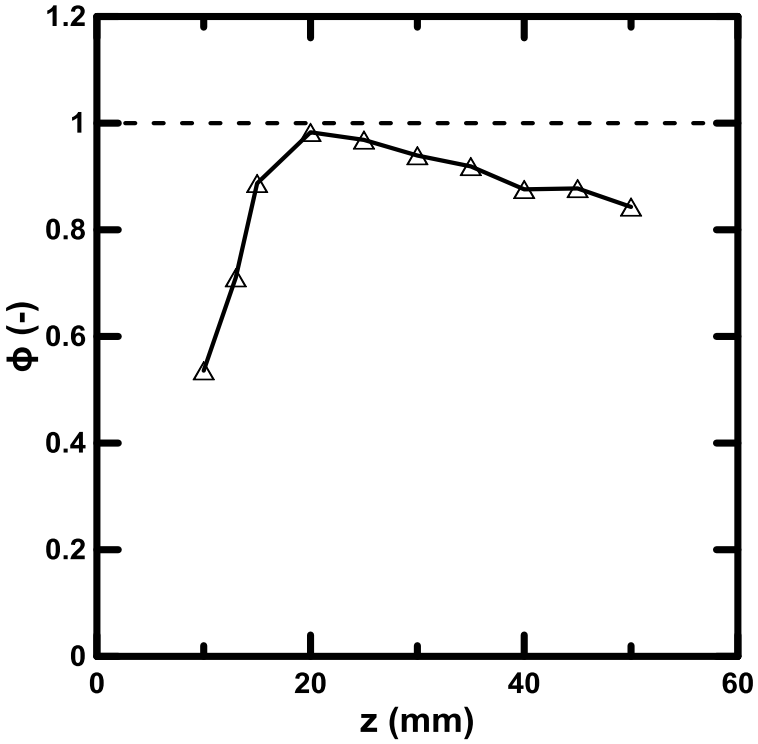

Figure 4-27 Local equivalence ratio versus height.

4.5. Soot Flame Summary

The following properties of the developed soot flame were measured: temperature, soot concentration, velocity, soot primary particle diameter, and stable species concentration. The temperatures in the soot flame are between 1500 – 1725 K. Soot temperatures are nearly uniform in the radial direction. The peak soot temperature was found at 13 mm height. The integrated soot volume fractions are between 10^{-5} – 10^{-4} mm^2. Normalized by the flame sectional area yields average soot volume fractions between 1 – 15 ppm. Velocities are between 2 – 3 m/s. Velocities increase with height owing to buoyancy. Soot primary particle diameters are between 20 – 45 nm. Soot diameter decreases with height owing to oxidation. O_2 concentrations are between 0.8 – 10%, and

peak near the ring burner top. O_2 is from the entrainment of air from the lower coflow flame. The flame is found to be lean at heights between 10 – 55 mm.

Chapter 5: OH Concentration Estimation

The measurement of radical concentrations (OH, O, and H) in reacting flows is very challenging, especially in the presence of soot. The investment required in cost and time is tremendous. Therefore this chapter presents methods for estimating OH concentrations using assumptions of partial and complete equilibrium, with the measured stable species concentration and temperature.

5.1. Radical Introduction

Fenimore et al. [30] were the first to advocate the importance of OH radical in soot oxidation. The role of OH in soot oxidation was thereafter investigated in Refs. [12, 15, 16, 34, 39-41], with different approaches for OH determination.

Lasers have been used to measure OH concentrations in flames either by absorption or fluorescence [15, 16, 84, 85]. The accuracy deteriorates in the presence of soot flame due to the strong scattering, absorption, and thermal emission from soot at the wavelengths of interest.

Laser induced fluorescence (LIF) is the most widely used direct OH concentration measurement technique. This involves tuning a laser to a specified wavelength (typically 306 nm) to excite the OH radicals. Those radicals then de-excite and emit fluorescence, which can be detected and used to determine the OH concentration [15, 16, 39, 84]. However, its accuracy quickly deteriorates when soot is present because: soot attenuates both the incident laser and the emitted fluorescence; and soot radiation interferes with the

laser. Garo et al. [39] used LIF for their methane/air diffusion flame and admitted that the accuracy of the optical LIF data was not sufficient for analyzing the soot oxidation process, where the local soot volume fractions were low, between 0 – 0.2 ppm.

OH concentrations have also been measured using the laser absorption method of Refs. [86, 87]. Similarly, the OH absorption and the soot attenuation of laser are intertwined in a sooting flame, and corrections are required.

Indirect measurements of OH involve measurements of other radicals (O or H), and/or stable species (H_2, O_2, CO, CO_2, and H_2O). The OH concentrations are then determined based on equilibrium assumptions (partially or completely) with measured temperatures.

One indirect method is the lithium atom absorption method [12, 34, 40, 41]. LiCl powder seeded nitrogen is introduced to flames. In a flame the Li becomes either atomic or in the form of LiOH, which is expected to be in equilibrium according to $Li + H_2O \leftrightarrow LiOH + H$. Radical H concentration is determined from the above equilibrium assumption. Radical OH and O concentrations are then estimated based on a partial equilibrium assumption. Unfortunately, introducing extra powder seeded nitrogen into the fuel system can be very intrusive. The accuracy depends on the validity of the two equilibrium assumptions.

Similarly, Fenimore and Jones [30] substituted N_2O for part of the CO_2 in the mixing chamber and determine the O concentration from the equilibrium in $O + N_2O \leftrightarrow 2NO$. Radical OH concentration was then estimated by further assuming equilibrium in O

+ $H_2O \leftrightarrow 2OH$. Similar to the lithium atom absorption method, two equilibrium assumptions are required.

Other indirect measurements of OH are established based on only stable species measurements and the equilibrium assumption. These are the focus of the rest of this chapter.

Mitchell et al. [83, 88] assumed partial equilibrium holds within a set of bimolecular reactions.

$$H + O_2 \leftrightarrow OH + O, \quad K_1 \tag{5-1}$$

$$O + H_2 \leftrightarrow OH + H, \quad K_2 \tag{5-2}$$

$$OH + H_2 \leftrightarrow H + H_2O, \quad K_3 \tag{5-3}$$

$$OH + CO \leftrightarrow CO_2 + H, \quad K_4 \tag{5-4}$$

where $K_1 – K_4$ are equilibrium constants of the reactions.

Although the equilibrium of these reactions was supported in a variety of premixed flames, its accuracy deteriorates in diffusion flames [83]. It was therefore postulated that since diffusion is a relatively slow process, sufficient time is available in the reaction zone to allow chemical reaction to reach complete equilibrium. In their studies of a CH_4/air diffusion flame [83, 88], partial equilibrium was found to exist near the flame sheet. Elsewhere this partial equilibrium condition quickly breaks down. Garo et al. [39] showed similar observations with the same flame setup by comparing the LIF determined OH with the partial equilibrium results. Whereas near the flame sheet the LIF

results agreed with the partial equilibrium within a factor of 2, the agreement deteriorated quickly at the flame centerline for laminar jet diffusion flames.

Complete equilibrium calculations can be readily obtained from the measured stable species concentrations and temperatures in steady flames [83, 84, 89, 90]. The results depend only on thermodynamics and the conditions specified. Equilibrium is determined based on the minimization of Gibb's free energy.

Puri et al. [15] compared their LIF determined OH concentrations with those estimated from complete equilibrium. They found that in lean regions the measured OH concentration approaches the equilibrium condition. Specifically lean regions of a sooting hydrocarbon diffusion flame, the equilibrium condition is quickly achieved. They pointed out that the large soot surface area can serve as a chaperon, M, for three-body recombination reactions.

Mulcahy and Young [91] studied the oxidation of carbon at 298 K by OH. OH radicals react rapidly to produce CO and CO_2. Their findings support the catalyzed recombination reaction of:

$$H + OH + C \rightarrow H_2O + C, \qquad (5\text{-}5)$$

and when H atoms are present, this reaction is several times faster than the gasification of the carbon by OH. Equilibrium of reaction (5-5) helps the local equilibrium condition quickly achieved.

Neoh [12] suggested that in lean flames the following reaction is in near equilibrium:

$$O_2 + 2H_2O \leftrightarrow 4OH, \quad K_6 \tag{5-6}$$

and that in rich flames the following equation is:

$$CO_2 + H_2O \leftrightarrow CO + 2OH. \quad K_7 \tag{5-7}$$

These claims have not been verified. If the OH concentration in a flame has not reached equilibrium, then the assumption that reactions (5-6) and (5-7) are equilibrated is not valid [12]. Equations (5-6) and (5-7) can thus be used as a validation of the complete equilibrium assumption.

In this study, OH concentrations will be estimated from the measured temperature and stable species concentrations, with the complete equilibrium assumption. The equilibrated OH concentration will also be compared with that calculated with the partial equilibrium assumption, and the lean/rich equilibrium condition suggested by Neoh [12].

5.2. Radical Estimation

5.2.1. Partial Equilibrium Estimation

Combustion simultaneously involves both fast and slow reactions. Under the partial equilibrium assumption it is assumed that the fast reactions are equilibrated even though the system as a whole is not. A set of four bimolecular reactions, (5-1) – (5-4), is usually assumed to be equilibrated [83, 88]:

Quantities $K_1 – K_4$ are the equilibrium constants for the shuffle reactions. In most hydrocarbon flames the H_2 concentration is relatively low and therefore it is treated as an

unknown to avoid the uncertainty in measuring H_2. Equilibrium of Eqs. (5-1) – (5-4) then yields:

$$p_{OH} = \mathrm{K}_1^{0.5}\mathrm{K}_2^{0.5}\mathrm{K}_3^{-0.5}\mathrm{K}_4^{0.5} p_{O_2}{}^{0.5} p_{H_2O}{}^{0.5} p_{CO}{}^{0.5} p_{CO_2}{}^{-0.5}, \tag{5-8}$$

$$p_O = \mathrm{K}_1\mathrm{K}_4 p_{O_2} p_{CO} p_{CO_2}{}^{-1}, \tag{5-9}$$

$$p_H = \mathrm{K}_1^{0.5}\mathrm{K}_2^{0.5}\mathrm{K}_3^{-0.5}\mathrm{K}_4^{1.5} p_{O_2}{}^{0.5} p_{H_2O}{}^{0.5} p_{CO}{}^{1.5} p_{CO_2}{}^{-1.5}, \text{ and} \tag{5-10}$$

$$p_{H_2} = \mathrm{K}_3^{-1}\mathrm{K}_4 p_{H_2O} p_{CO} p_{CO_2}{}^{-1}. \tag{5-11}$$

The last equation comes from the water-gas shift reaction, which can normally be used as a quick check for the partial equilibrium condition. Equilibrium constants were calculated from the JANAF thermochemical tables [92], using:

$$\log(K) = \sum \log(K_{i,prod}) - \sum \log(K_{i,react}) \tag{5-12}$$

Mitchell et al. [83, 88] used $K_p = 0.039 \exp(3500 / T)$ to fit $K_3^{-1}K_4$. If the reactions are partially equilibrated, the equilibrium must also exist for the water-gas shift reaction, and the temperature dependent K_p must satisfy $K_p = [CO_2][H_2] / [CO][H_2O]$. However, water-gas shift reaction does not guarantee partial equilibrium.

For flames where CO and CO_2 are not abundant, it is also usually assumed that partial equilibrium exists among three reactions $\mathrm{K}_1 – \mathrm{K}_3$ [93]:

$$p_{OH} = \mathrm{K}_1^{0.5}\mathrm{K}_2^{0.5} p_{O_2}{}^{0.5} p_{H_2}{}^{0.5}, \tag{5-13}$$

$$p_O = \mathrm{K}_1\mathrm{K}_3 p_{O_2} p_{H_2} p_{H_2O}{}^{-1}, \text{ and} \tag{5-14}$$

$$p_H = \mathrm{K}_1^{0.5}\mathrm{K}_2^{0.5}\mathrm{K}_3 p_{H_2}{}^{1.5} p_{O_2}{}^{0.5} p_{H_2O}{}^{-1}. \tag{5-15}$$

Along the centerline of the CH_4 / air diffusion flame of Mitchell [88] and Garo et al. [39], where both O_2 and H_2 were present, the four-reaction mechanism in Eq. (5-8) and the three-reaction mechanism in Eq. (5-13) yield OH concentrations that agree within 10%. In all the hydrocarbon diffusion flames used by Xu et al. [34], the agreement is better than 30% at locations where H_2 mole fraction exceeds 0.5%. It is therefore postulated here that, because the reactions involving CO and CO_2 are relevantly slow, their presence will not affect the equilibrium condition, regardless of whether partially or completely equilibrated. Both equations were tested for the current study.

5.2.2. Full Equilibrium Estimation

The radical concentration at the complete equilibrium condition was estimated using CHEMKIN [89, 90]. It was assumed that complete equilibrium exists among the following species: H_2, O_2, N_2, CO, CO_2, H_2O, O, H, and OH. The thermodynamic properties of the species were found in the CHEMKIN default thermodynamic database Ver. 4.0 [90]. The measured stable species mole fractions and temperature were used as the input. The equilibrated species concentration was estimated by minimizing the Gibb's free energy assuming the combustion process is a constant pressure, constant enthalpy process. An advantage of this complete equilibrium method is that its accuracy is not affected by the detailed chemistry selection or by uncertainties in the reaction rate.

5.2.3. Catalyzed Partial Equilibrium Estimation

If the catalytic carbon increases the reaction rates of (5-5) in both directions, its equilibrium condition (equilibrium constant denoted by K_5) must affect the partial equilibrium among reactions (5-1) – (5-3). Linearly recombining reactions (5-1) – (5-3)

and (5-5), and assuming they are equilibrated, also suggests the equilibrium condition among the following reactions:

$$\mathrm{H+H+M \leftrightarrow H_2+M}, \qquad \mathrm{K_8} \tag{5-16}$$

$$\mathrm{O+O+M \leftrightarrow O_2+M}, \qquad \mathrm{K_9} \tag{5-17}$$

$$\mathrm{O+H+M \leftrightarrow OH+M}. \qquad \mathrm{K_{10}} \tag{5-18}$$

In fact, if reactions (5-1) – (5-3) are equilibrated, involving any of Eqs. (5-5) and Eq. (5-16) to Eq. (5-18) yields all the others. Detailed derivations will not be presented here. Here, reaction (5-5) is assumed to be equilibrated, which yields:

$$p_{OH} = \mathrm{K_1}^{0.25}\mathrm{K_2}^{0.25}\mathrm{K_3}^{-0.25}\mathrm{K_5}^{-0.25} p_{O_2}{}^{0.25} p_{H_2O}{}^{0.5}, \tag{5-19}$$

$$p_H = \mathrm{K_1}^{-0.25}\mathrm{K_2}^{-0.25}\mathrm{K_3}^{0.25}\mathrm{K_5}^{-0.75} p_{O_2}{}^{-0.25} p_{H_2O}{}^{0.5}, \text{ and} \tag{5-20}$$

$$p_O = \mathrm{K_1}^{0.5}\mathrm{K_2}^{-0.5}\mathrm{K_3}^{0.5}\mathrm{K_5}^{-0.5} p_{O_2}{}^{0.5}. \tag{5-21}$$

The expression for OH in Eq. (5-19) is identical to the equilibrium assumed by Neoh [12] in reaction (5-6). In is noted that in flames where only H_2, O_2, N_2, CO, CO_2, H_2O, O, H, and OH were assumed to be important, partially equilibrium among reactions (5-1) – (5-3), (5-5), and (5-16) – (5-18) involves most of the possible reactions, and suggests a complete equilibrium condition.

In rich flames where O_2 cannot be accurately measured, reaction (5-4) was involved, and OH can be determined from:

$$p_{OH} = \mathrm{K_4}^{-0.5}\mathrm{K_5}^{-0.5} p_{CO_2}{}^{0.5} p_{H_2O}{}^{0.5} p_{CO}{}^{-0.5}. \tag{5-22}$$

Similarly, this expression is identical to the equilibrium Neoh suggested in Eq. (5-7). In the current study, the flame was found to be lean at all heights.

5.3. Radical Results

The measured species ratio $[CO_2][H_2] / [CO][H_2O]$ versus flame temperature was compared with the water-gas shift equilibrium constant $K_p = 0.039 \exp(3500 / T)$, as shown in Fig. 5-1. As indicated, the partial equilibrium condition was not satisfied.

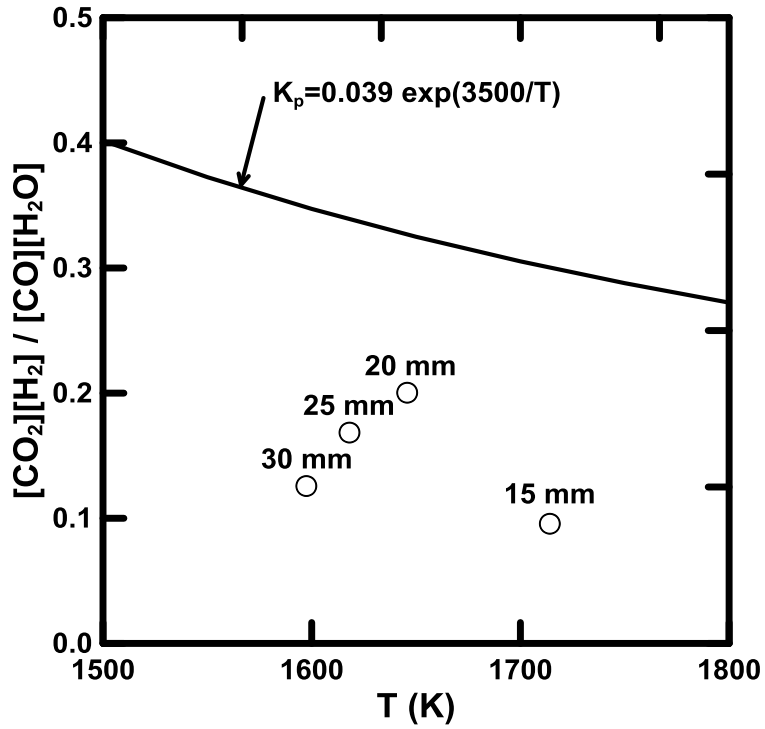

Figure 5-1 Comparison between the water-gas equilibrium constant and the ratio of $[CO_2][H_2] / [CO][H_2O]$ from the measured species concentration in the ternary flame.

Radical concentrations (OH, O, and H) determined from partial equilibrium (four-reaction mechanism, three-reaction mechanism, and catalyzed mechanism), and complete equilibrium calculations are presented in Figs. 5-2 to 5-4. Since the soot flame was found to be lean at all heights, Eqs. (5-19) to (5-21) were used for the catalyzed mechanism.

As shown in the figures, radical concentrations predicted using the four-reaction mechanism agrees well with that using the three-reaction mechanism, except for the heights where H_2 concentration was too low to be accurately determined. OH mole fractions estimated from the four-reaction mechanism are between $10^{-3} – 10^{-2}$. This range is similar to what Neoh et al. [12] measured in premixed flames, where radical overshooting is normally expected, and is much higher than those measured ($10^{-6} – 10^{-3}$) in hydrocarbon diffusion flames [15, 34, 39]. The four-reaction mechanism predicts radical concentrations that are at least 10 times those predicted by complete equilibrium.

Complete equilibrium yields OH concentrations close to those estimated from the catalyzed mechanism, suggesting the current flame may be near equilibrium condition [12]. In the complete equilibrium estimation, OH mole fraction was between $10^{-4} – 10^{-3}$, and peaked at 13 – 15 mm height. The peak OH locations correspond to the measured peak temperatures. OH concentration was about an order of magnitude higher than O concentration, supporting its more important role in soot oxidation. H mole fraction was estimated to be one order of magnitude lower than O mole fraction.

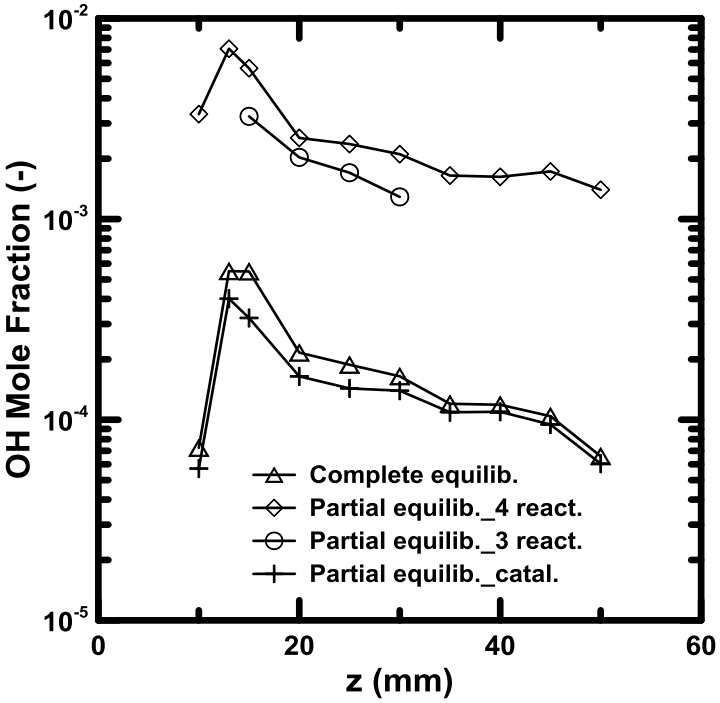

Figure 5-2 OH radical estimated from partial equilibrium (four-reaction, three-reaction, and catalyzed mechanism), and complete equilibrium.

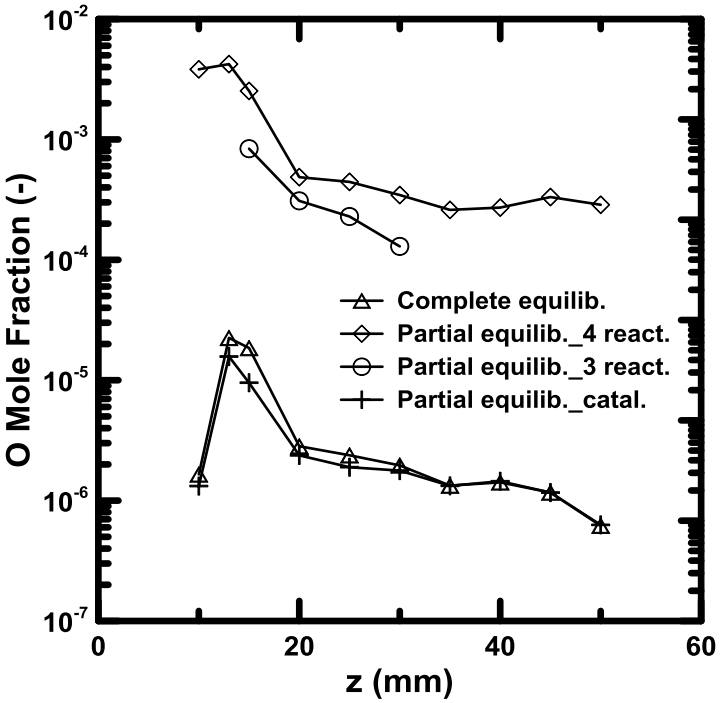

Figure 5-3 O radical estimated from partial equilibrium (four-reaction, three-reaction, and catalyzed mechanism), and complete equilibrium.

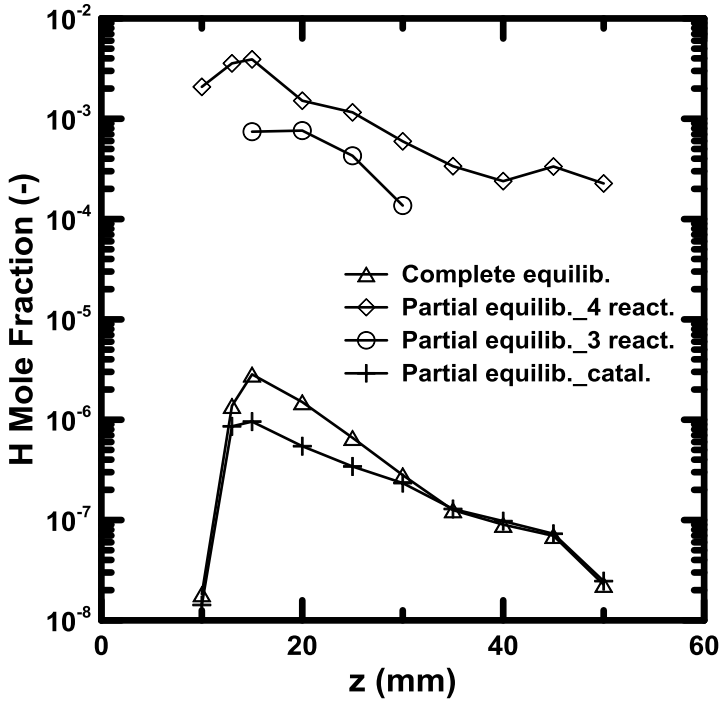

Figure 5-4 H radical estimated from partial equilibrium (four-reaction, three-reaction, and catalyzed mechanism), and complete equilibrium.

The complete equilibrium estimations are subject to uncertainties. Figure 5-5 shows the super-equilibrium ratio (SR) versus the local equivalence ratio (Φ) from past studies [15, 16, 34, 39, 85]. Super-equilibrium ratio is defined as the measured radical concentration divided by the estimated radical concentration from complete equilibrium. These studies are all diffusion flames, and OH from the flame centerline is used.

Cheng et al. [85] used two H_2/air laminar diffusion flames and measured the OH concentration with LIF. Φ was calculated based on their species measurements. The OH concentration at complete equilibrium was calculated using CHEMKIN, with their measured species concentration and temperature.

Garo et al. [39] used a CH_4/air laminar diffusion flame and measured the OH concentration with LIF. The detailed species concentration and temperature profile were found in the work of Mitchell [88] where the same flame setup was used. Φ and OH at equilibrium were calculated similarly.

Puri et al. [15, 16] used three hydrocarbon laminar diffusion flames and measured the OH concentration with LIF. SR and Φ were obtained from their tabulated data.

Xu et al. [34] used fine hydrocarbon laminar diffusion flames and measured the OH concentration with the lithium atom absorption method. Similarly, SR and Φ were calculated with their measured species concentration and temperature.

As shown in Fig. 5-5, OH in flames quickly approaches to its complete equilibrium condition as Φ reduces. The data is scattered because the radical equilibrium condition in flames can be a complex function of temperature, stoichiometry, residence time, diffusion, and detailed chemistry. Corrections based on the fitting will not be attempted for the current study due to uncertainty. However, it is also noted that average soot concentration in the current study is 1 – 15 ppm at heights between 10 – 50 mm, and is much higher than the soot concentration (0 – 6 ppm) observed in the past studies [15, 16, 34, 39, 85]. The catalytic effect of the soot surface in the equilibrium of reaction (4-5) is expected to be important. And OH equilibrium is expected to be quickly achieved in the current study. OH concentrations estimated from the complete equilibrium assumption were used in its correlation with the oxidation rates.

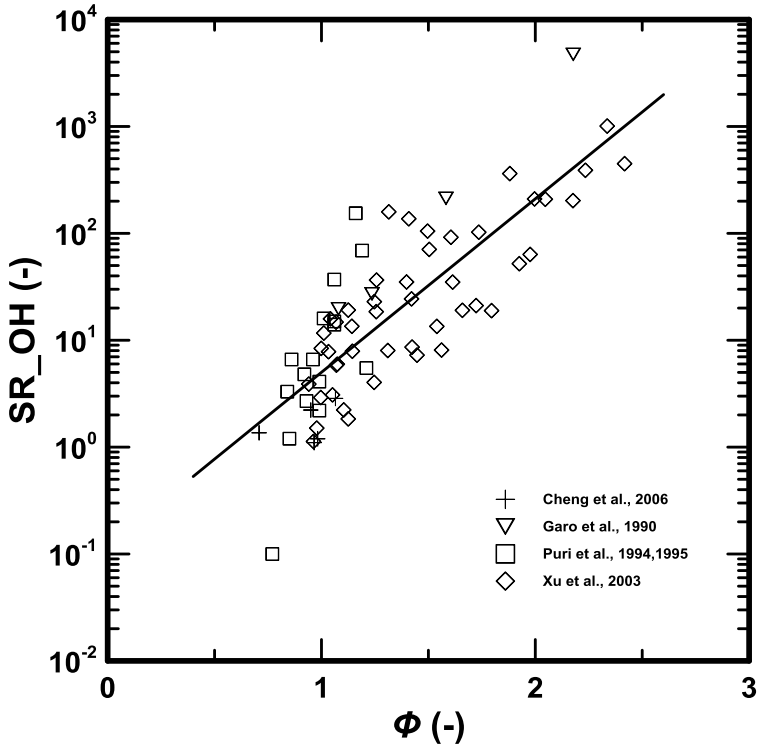

Figure 5-5 Super-equilibrium ratio versus local equivalence ratio from past studies.

Uncertainty in OH estimation, as propagated from the uncertainty in temperature and species measurement, is estimated to be ±40% (95% confidence).

5.4. Radical Summary

Radical concentrations (OH, O, and H) were estimated from the measured stable species concentration and temperature, following different equilibrium assumptions (complete, four-reaction partial, three-reaction partial, and catalyzed partial). The four-reaction and three-reaction mechanism predicts OH concentration about one order of magnitude higher than OH predicted from the catalyzed mechanism and complete equilibrium. OH equilibrium condition from past studies was also analyzed, and the complete equilibrium was found to predict better in the lean flame region. OH partial

pressures are between 10^{-4} – 10^{-3} bar. Complete equilibrium determined radicals were chosen for its correlation with the oxidation rates.

Chapter 6: Optimized Soot Oxidation Mechanisms for O_2 and OH

It is generally accepted that the two main soot oxidizers in flames are molecular oxygen (O_2) and hydroxyl radical (OH). The leading soot oxidization mechanisms for these species generally disagree with more recent studies that measured soot oxidation rates in various systems, including diffusion flames, premixed flames, tube furnaces, and thermogravimetric analyzers (TGA). To address this, 13 past experimental studies are examined here. These included 170 measurements of soot oxidation rates with a variation of 8 orders of magnitude. These are all the known measurements where these required quantities were reported: soot oxidation rate, major species, OH concentrations, and temperature. The measurements were correlated to yield new soot oxidation rates for O_2 and OH. The activation energy and the pre-exponential factors were determined by maximizing the coefficient of determination in fitting the measured overall oxidation rates with the predictions. The resulting activation energy for O_2 with soot is 195 kJ/mol, while the activation energy for OH with soot is negligible. The resulting constant collision efficiency for OH is 0.1. These soot oxidation mechanisms for O_2 and OH match the measured soot oxidation rates with a R^2 coefficient of determination of 0.98.

6.1. Oxidation Mechanism Introduction

Soot in flames can be oxidized by O_2, OH, O, CO_2, and H_2O [8, 10, 94]. Most soot nucleation and growth reactions are believed to be reversible. It is generally agreed that the soot diameter is small such that the diffusion of oxidizers to the soot surface is fast enough that the reactions are mostly kinetics controlled [12]. The kinetics of the

above oxidizers reacting with soot particles were briefly reviewed in Chapter 1. The contribution of CO_2 and H_2O to the overall soot oxidation in flames is negligible due to their low reactivity with soot [35, 37]. The reactivity of O is comparable to that of OH radical; however, its concentration is generally more than one order of magnitude lower than the OH concentration [33, 34]. The contribution of O to the overall oxidation is also negligible, compared with OH. Soot is assumed to be mainly oxidized by O_2 and OH, in both experimental [12, 14-16, 34, 39-41] and numerical studies [1-5, 42, 45]. Until now the leading soot oxidation mechanisms for these species had not been systematically compared with the large body of published soot oxidation measurements. Furthermore, they were based either on experiments with significant uncertainty or on substances very different from soot.

For O_2, the leading mechanism is that of Nagle and Strickland-Constable (NSC) [11]. They measured oxidation rates of heated carbon rods under O_2 impingement. Unfortunately, the experiment bore little resemblance to soot oxidation in flames. Nagle et al. [11] reported reasonable agreement between measurements and predictions for carbon filament oxidation at O_2 partial pressure of 2.5×10^{-5} bar. However, the oxidation rates obtained with the reactor graphite are higher than the predictions by approximately an order of magnitude, suggesting a surface reactivity difference.

Another widely used O_2 mechanism is that by Lee et al. [19], which was established by studying soot oxidation in the O_2 enriched post flame region of a hydrocarbon diffusion flame. The mechanism of Lee et al. [19] involves an activation

energy of 164.4 kJ/mol at temperatures between 1300 – 1700 K, and at O_2 partial pressures of 0.05 – 0.1 bar.

A comparison of the predicted soot oxidation rates due to O_2 with the correlations by NSC [11] and by Lee et al. [19] were made, as shown in Fig 6-1. The O_2 partial pressure was between 10^{-4} – 1 bar, and the temperatures were between 1500 – 2000 K. The measurement ranges of the two studies were also shown, as indicated by shading. The simpler Lee's correlation shows first-order O_2 dependence and the rate increases with increasing temperature. The more complicated NSC expression exhibits two noteworthy phenomena:

1. the increase of oxidation rate with O_2 is slower at higher O_2 partial pressure, indicating saturation; and

2. oxidation rate has a negative temperature coefficient at low O_2 partial pressure.

Nagle et al. [11] presumes that at higher temperatures, the carbon surface will be covered by less reactive sites, therefore reducing the overall oxidation rate by O_2. However, this temperature-dependent conversion has not been validated for soot. These two predictions disagree by up to a factor of 20 in Fig. 6-1.

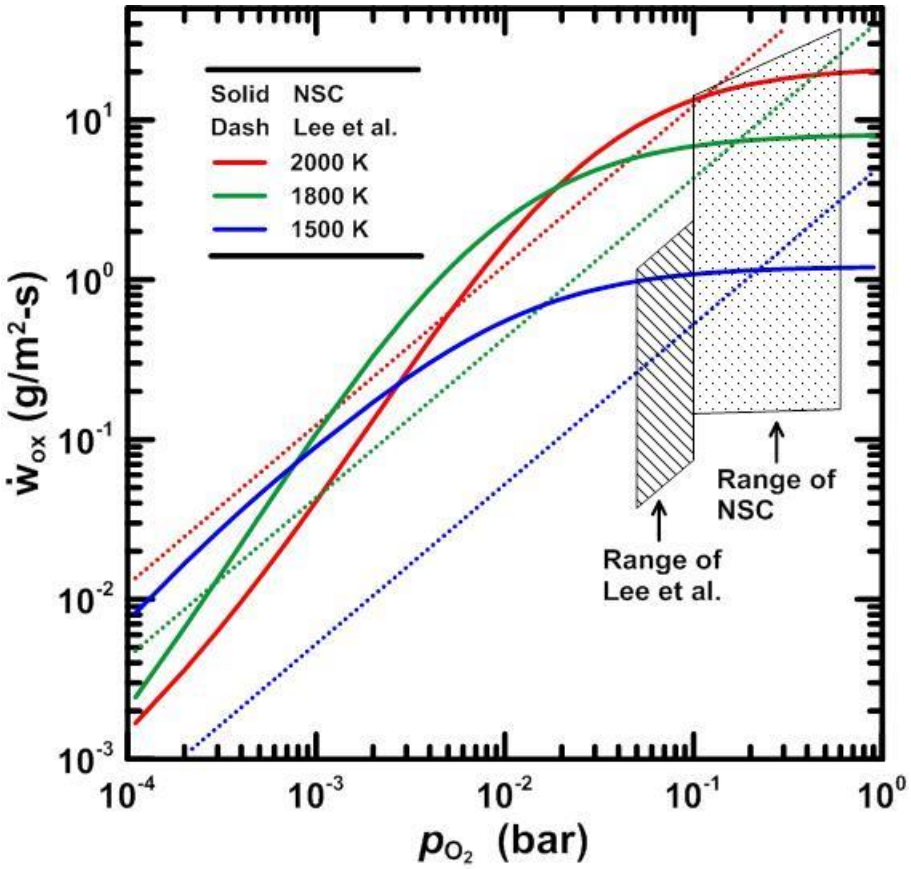

Figure 6-1 Comparison of the predicted soot oxidation rates due to O_2 using the formulation by Nagle et al., and Lee et al. The shaded areas show their measurement ranges.

Chan et al. [20] used an experiment setup similar to that of Lee et al. [19], and studied the soot oxidation due to O_2 in the post flame region and in the TGA environment. The activation energy is 143.5 kJ/mol at temperatures between 770 – 1250 K. They explored the soot oxidation in a temperature range lower than that of Lee et al. [19]. The resulting activation energy was also slightly lower.

Other low temperature soot oxidation studies in the TGA environment are in Refs. [24-29]. Kalogirou et al. [28] compared the oxidation of diesel soot and synthetic soot under the TGA environment at temperatures between 800 – 1000 K. They obtained an

activation energy of 161.2 kJ/mol. The reaction was dependent on the O_2 partial pressure raised to the power of 0.75. Unfortunately, the soot surface area was not measured. Similarly, Sharma et al. [29] measured the oxidation of soot in the TGA environment at temperatures between 800 – 900 K. They admitted that the oxidation was affected by the soot surface area. In their simplified model, however, they neglected this. Their activation energy for diesel soot reacting with O_2 is 155 kJ/mol.

Higgins et al. [21] studied the oxidation of soot by O_2 at temperatures between 1100 – 1400 K in a flow reactor. Soot with different initial mobility diameters was used for their study. Soot was oxidized in a constant temperature flow reactor, and the oxidation rates were determined by measuring the mobility diameter at the inlet and exit of the reactor. Their data yielded an activation energy of 164 kJ/mol, with respective pre-exponential factor for each initial particle size, differed by a factor up to 1.7.

Although conditions in TGAs and flow reactors are different from those in flames, they provide valuable low temperature oxidation information which cannot be achieved in flames. Residence times in flames are too short [34] to accurately observe oxidation rates below 10^{-2} g/m^2-s. TGAs and flow reactors cannot measure soot oxidation rates at higher temperatures.

The activation energy in soot oxidation due to O_2 is commonly compared with that obtained in coal burning due to the chemical similarity between soot and coal. Smith [94] reviewed the combustion of various types of carbons (coke, char, graphite, soot, etc.) from different studies and obtained an overall activation energy of 179.1 kJ/mol.

However, the diameter of coke or char primary particles is normally orders of magnitude larger than that of soot, and the oxidation kinetics is limited by the oxygen diffusion [94].

Soot oxidation with O_2 has also been included in several numerical models with detailed reaction kinetics [1-7, 42, 45]. The leading numerical model of soot formation and oxidation is that by Appel, Bockhorn, and Frenklach (ABF) [2, 3, 42]. O_2 was assumed to only react with activated soot radical. ABF includes an Arrhenius form with an activation energy of 31.3 kJ/mol for O_2. This value is from the work by Lin and Lin [44], where the reaction between phenyl radical (C_6H_5) and O_2 from low temperature shock tube was studied. And it is significantly lower than all the other studies. The various reported activation energy of O_2 reacting with soot is summarized in Table 6-1.

Table 6-1 Summary of the activation energy reported from the past studies.

Study	Condition	Material	E_A (kJ/mol)	T (K)
Chan et al., 1987	diffusion flame	soot	143.5	770 – 1250
Higgins et al., 2002	flow reactor	soot	165.0	1070 – 1400
Kalogirou et al., 2010	TGA	soot	161.2	820 – 970
Lee et al., 1962	diffusion flame	soot	164.4	1200 – 1670
Lin and Lin, 1987	shock tube	phenyl	31.3	1030 – 1670
Smith, 1982	N/A	various carbon	179.1	600 – 2300
Sharma et al., 2012	TGA	soot	155.0	830 – 910

For OH, Fenimore and Jones [30] considered a two-stage burner where the soot-laden combustion gases from the first stage were mixed with air and burned in the second stage. They postulated that their flames possessed an additional mechanism besides

oxidation by O_2; and advocated the importance of OH in soot oxidation. They obtained OH collision efficiency, η_{OH} of 0.1.

Neoh et al. [12-14] considered a similar experiment and examined soot oxidation with different equivalence ratios. OH was found to be the primary oxidizer in their flames, with a collision efficiency of 0.13. Soot oxidation by O_2, predicted using the NSC expression [11], had to be subtracted from the measured oxidation rates. Considering the uncertainty in the NSC expression, this subtraction leads to even higher uncertainty if the oxidation rates of O_2 and OH are similar.

Soot oxidation was also studied in hydrocarbon diffusion flames [15, 16, 34, 39-41], with an anticipation of fitting the measurements with predictions using Refs. [11-14]. Garo et al. [39] used a methane diffusion flame and was only able to observe soot oxidation within 5 mm height. Puri et al. [15, 16] studied soot oxidation in methane, methane/butane, and methane/butene flames. Soot oxidation was subsequently observed in a variety of hydrocarbon diffusion flames at pressures from 0.1 – 8.0 bar [34, 40, 41]. Unfortunately, all these flames involved soot oxidation in the presence of hydrocarbons, requiring corrections for effects of soot surface growth. The measured oxidation rates, subtracted by the oxidation due to O_2 using the NSC expression, were used to calculate the collision efficiency for OH. The resulting OH collision efficiencies vary between 0.01 – 0.4. The subtraction yields negative OH collision efficiencies in some measurements from Refs. [15, 16, 34, 40, 41], so those points are neglected.

The diversity in soot oxidation rate expressions for O_2 and OH attests to the uncertainties in all these expressions. It also limits exploring the oxidation expressions of

other minor oxidants (O, CO_2, and H_2O), which require corrections for oxidation by O_2 and OH. The objective of the current study is to develop soot oxidation mechanisms for both O_2 and OH, that better match the soot oxidation rates of past studies.

6.2. Past Oxidation Studies

Table 6-2 summarizes the 13 studies to date that report soot oxidation rate, temperature, O_2, and OH, if there is any. Included are the number of measurements, test conditions, and the assumed oxidants. These studies contain 170 measurements. Only soot is considered here. Char, graphite, coke, synthetic soot, etc., are not included because their diameters are generally more than one order of magnitude larger than soot and therefore the diffusion limits the chemical kinetics. Furthermore the similarity in surface reactivity between soot and other carbon materials is not well understood.

The studies in Table 6-2 include different experimental approaches and their oxidation rate expressions are different. They were therefore corrected and converted to g/m^2-s in consistency, as follows.

The work of Garo et al. [39] reported 6 measurements and the OH concentration was determined from the partial equilibrium assumption. Unfortunately, the partial equilibrium determined OH concentrations disagree with their direct measurements from the laser induced fluorescence (LIF) method. Mitchell et al. [83] using the same flame setup suggested that, while the partial equilibrium condition might exist in the high temperature primary reaction zone of their diffusion flame, the partial equilibrium

condition is poorly satisfied along the centerline. In the current study, only the data (50 mm height) with direct OH measurements was used.

The work of Guo and coworkers [95] measured soot oxidation in a hydrocarbon-free environment. The OH concentration was estimated from the complete equilibrium assumption. Details about the measurements and estimations can be found in the other chapters in this dissertation.

The work of Neoh [12] involves 86 measurements in 7 premixed flames. Here the data points were reduced to 11 by removing their interpolated data, without sacrificing the generality. Their measured oxidization rates based on the light scattering determined surface area were about 2 times higher than those determined from the TEM method [12]. They were therefore corrected in consistency with the other study.

In the TGA studies of Kalogirou et al. [28], the oxidation rate was expressed in terms of $\mathrm{d}m / m\,\mathrm{d}t$, neglecting the soot surface area effect. In the current analysis, it was converted with $\dot{w}_{ox} = d_p\,\rho_s\,\mathrm{d}m / (6\,m\,\mathrm{d}t)$ [12], in g/m^2-s, assuming constant soot density of 1860 g/m^3, and constant soot particle diameter of 40 nm [96]. In the current analysis, only the oxidation of diesel soot at the isothermal condition was selected for simplicity. The rates were calculated from their best fit expression. Similar conversions were also performed for the work of Sharma et al. [29]. The oxidation rates of diesel soot at the isothermal condition were obtained from their reported mass conversion factor profile (up to 90% mass loss). The soot surface area was estimated to reduce by up to one factor within 90% mass loss.

Puri et al. [15, 16] reported oxidation rates with $R_{ox} = \rho_s \, df_s / dt$, in kmol/m^3-s. In the current analysis, R_{ox} was converted to $\dot{w}_{ox} = d_p \, \rho_s \, df_s / (6 \, f_s \, dt)$ [47, 48], in g/m^2-s, with their measured d_p and f_s, in order to be consistent with the other study. The change of gas density due to temperature was neglected.

Table 6-2 Summary of past measurements of soot oxidation in various conditions.

Study	Number of meas.	Condition	Assumed oxidant
Chan et al., 1987	3	diffusion flame	O_2
Chan et al., 1987	9	TGA	O_2
Fenimore and Jones, 1967	3	premixed flame	O_2 and OH
Fenimore and Jones, 1967	2	tube furnace	O_2
Garo et al., 1990	1	diffusion flame	O_2 and OH
Guo, 2015	10	diffusion flame	O_2 and OH
Higgins et al., 2002	25	flow reactor	O_2
Kalogirou et al., 2010	6	TGA	O_2
Kim et al., 2004	12	diffusion flame	O_2 and OH
Kim et al., 2008	9	diffusion flame	O_2 and OH
Lee et al., 1962	29	diffusion flame	O_2
Neoh, 1980	11	premixed flame	O_2 and OH
Puri et al., 1994,1995	5	diffusion flame	O_2 and OH
Sharma et al., 2012	24	TGA	O_2
Xu et al., 2003	21	diffusion flame	O_2 and OH

The measured oxidation rates from past studies were first examined with the oxidation expressions of NSC [11] for O_2 using Eq. (1-6), and of Neoh et al. [12-14] for OH using Eq. (1-8) with a collision efficiency of 0.13. The results were plotted in Fig. 6-2, with measurements versus predictions. The measured oxidation rates were between 10^{-6} – 100 g/m^2-s. As shown, most of the data points fall above the prediction line,

indicating the models over-predict the oxidation rates. Specifically, the predictions perform poorly in the diffusion flames and the TGA. The R^2 for Fig. 6-2 is 0.79.

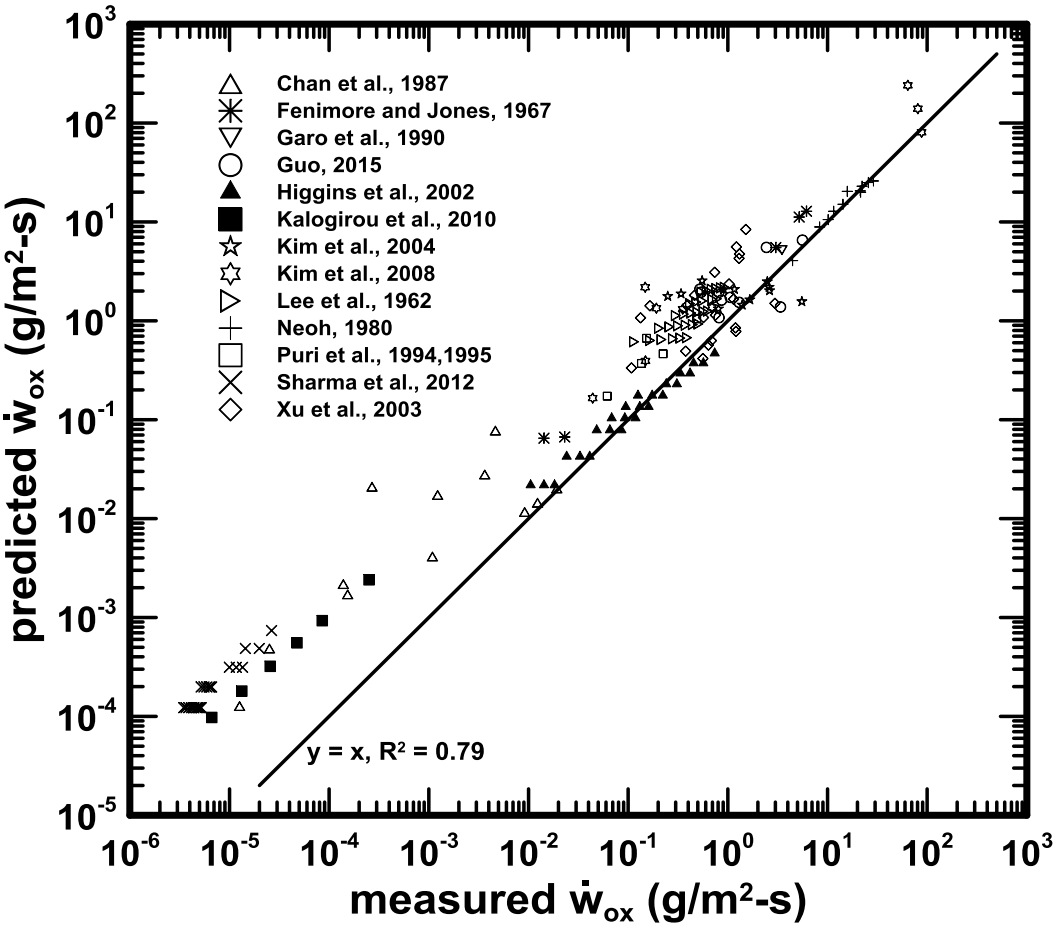

Figure 6-2 Comparison between the measured soot oxidation rate and the predictions using the expression of NSC for O_2 and Neoh et al. for OH.

6.3. Soot Oxidation Modeling

In the current study, it is assumed that the soot oxidation is not diffusion limited, but only controlled by the chemical kinetics. For both O_2 and OH mechanisms, bimolecular reactions with collision theory were assumed. Unlike the work in Refs. [12, 34, 40, 41], where constant collision efficiency (η) was assumed for both O_2 and OH, the

current work considered an Arrhenius form where the rate constant also depends on the activation energy (E_A), similar to Ref. [19].

The mean molecular velocity for oxidant *i* is [48]:

$$\bar{u}_i = \left(8R_u T / \pi MW_i\right)^{0.5}, \tag{6-1}$$

where *MW* is molar mass, R_u is the universal gas constant, *T* is temperature, and subscripts *i* denotes the oxidant species (O_2 or OH here). The oxidation rate with constant collision efficiency and constant activation energy is:

$$\dot{w}_{ox,i} = \frac{\eta_i [i] \bar{u}_i m_{C,i}}{4} \exp\left(-\frac{E_{A,i}}{R_u T}\right), \tag{6-2}$$

where bracket denotes the mole concentration, C_i is the mass of carbon removed per reactive collision, e.g., 12 g/mol for OH, and E_A is the activation energy. Combining the ideal gas equation, Equations (6-1) and (6-2), and rearranging the constants, yields the following form for soot oxidation due to species *i*

$$\dot{w}_{ox,i} = \frac{A_i p_i}{\sqrt{T}} \exp\left(-\frac{E_{A,i}}{R_u T}\right), \tag{6-3}$$

where *A* is the pre-exponential factor and *p* is partial pressure.

It is normally assumed that the activation energy for OH is negligible [12-14]. Therefore, Equation (6-3) can be reduced to

$$\dot{w}_{ox,i} = \frac{A_i p_i}{\sqrt{T}}, \tag{6-4}$$

which is identical to the formulation used in Refs. [12-14]. A_{OH} was converted to its equivalent η in the current study for comparison with the literature.

The activation energy and pre-exponential factor can be determined from the slope and intersection in the plot of K_i versus 1 / T, following the equation below:

$$K_i = \ln\left(\frac{w_{ox,i}\sqrt{T}}{p_i}\right) = -\frac{E_{A,i}}{R_u}\frac{1}{T} + \ln A_i . \tag{6-5}$$

Unfortunately, the oxidation of soot by O_2 and OH is simultaneous in most measurements. And attributing the appropriate oxidation rate to each oxidant is challenging if neither of their oxidation kinetics is sufficiently understood.

The proposed oxidation mechanism for O_2 was examined, assuming that oxidation was contributed by only O_2. Figure 6-3 shows the Arrhenius form plot of the oxidation rate from past studies versus the reciprocal of temperature. Also shown are the results calculated with the NSC expression [11], at O_2 partial pressures of 10^{-4} and 0.5 bar, respectively. These two are the lower and upper limit of O_2 partial pressures included in the current study. An obvious slope can be found from the figure, indicating the activation energy. The data scatters more at higher temperatures, due to possible oxidation by OH. The lower and upper boundaries of the NSC expression were only able to cover the oxidation rates at the middle temperature region. The coverage deteriorates at temperatures lower than 1000 K, or higher than 1600 K. Despite the effect from OH and the other neglected oxidants (O, CO_2, and H_2O), a linear fitting of the plotted data

(R^2 = 0.96) yields an activation energy of 213.6 kJ/mol. The pre-exponential factor is 183 $K^{0.5}$ s / m.

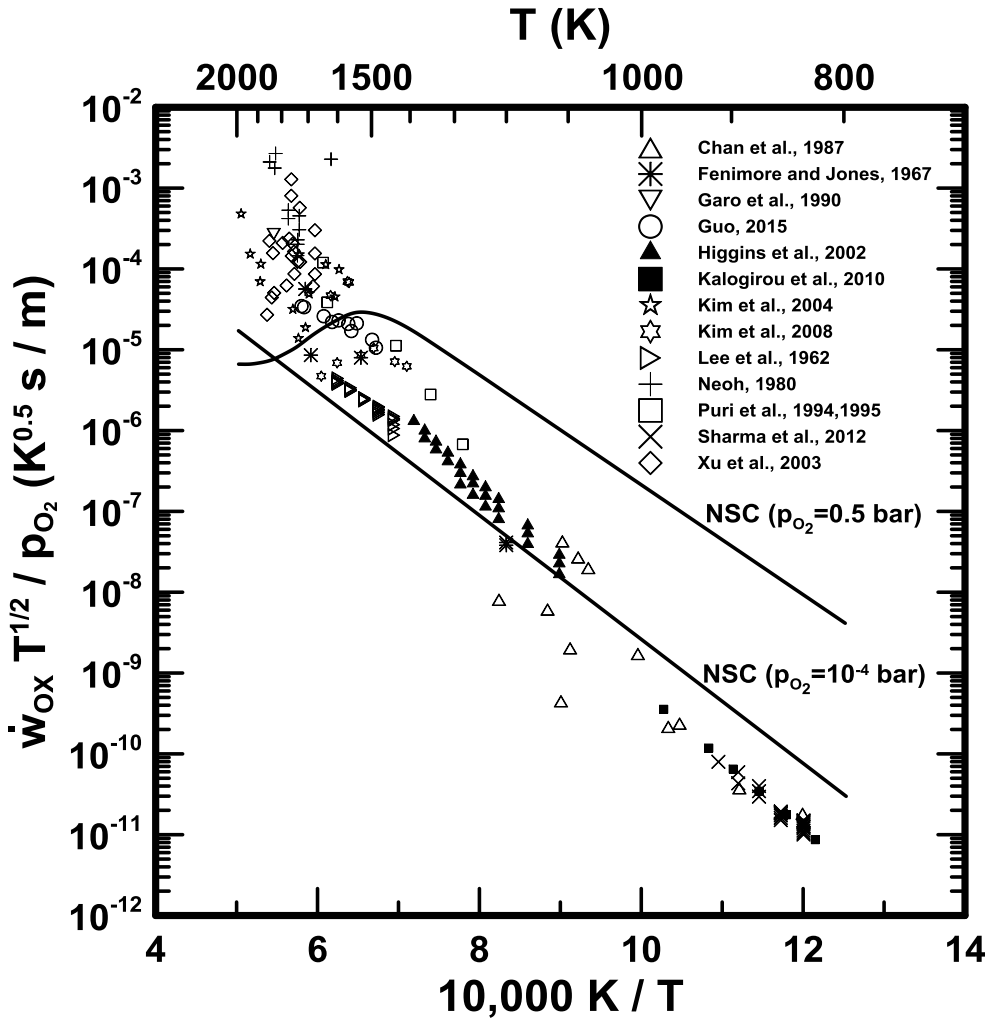

Figure 6-3 Arrhenius form plot of the soot oxidation rate from past studies versus the reciprocal of temperature, assuming the oxidation is only by O_2. Two solid lines are the results calculated with the NSC expression at 10^{-4} and 0.5 bar.

Similarly for OH, the overall oxidation was assumed to be from OH only, and the results are shown in Fig. 6-4. Also shown are the results of carbon oxidized by OH in the work of Mulcahy et al. [16, 91], estimated based on the lower and upper limit of their

reported collision efficiencies. Data scatters within two orders of magnitude in the y axis, at temperatures between 1300 – 2000 K. There is no statistical evidence that activation energy of OH exists, even when the temperature is extended to 298 K. A constant fitting yields an equivalent collision efficiency of 0.14 ± 0.03 (95% confidence).

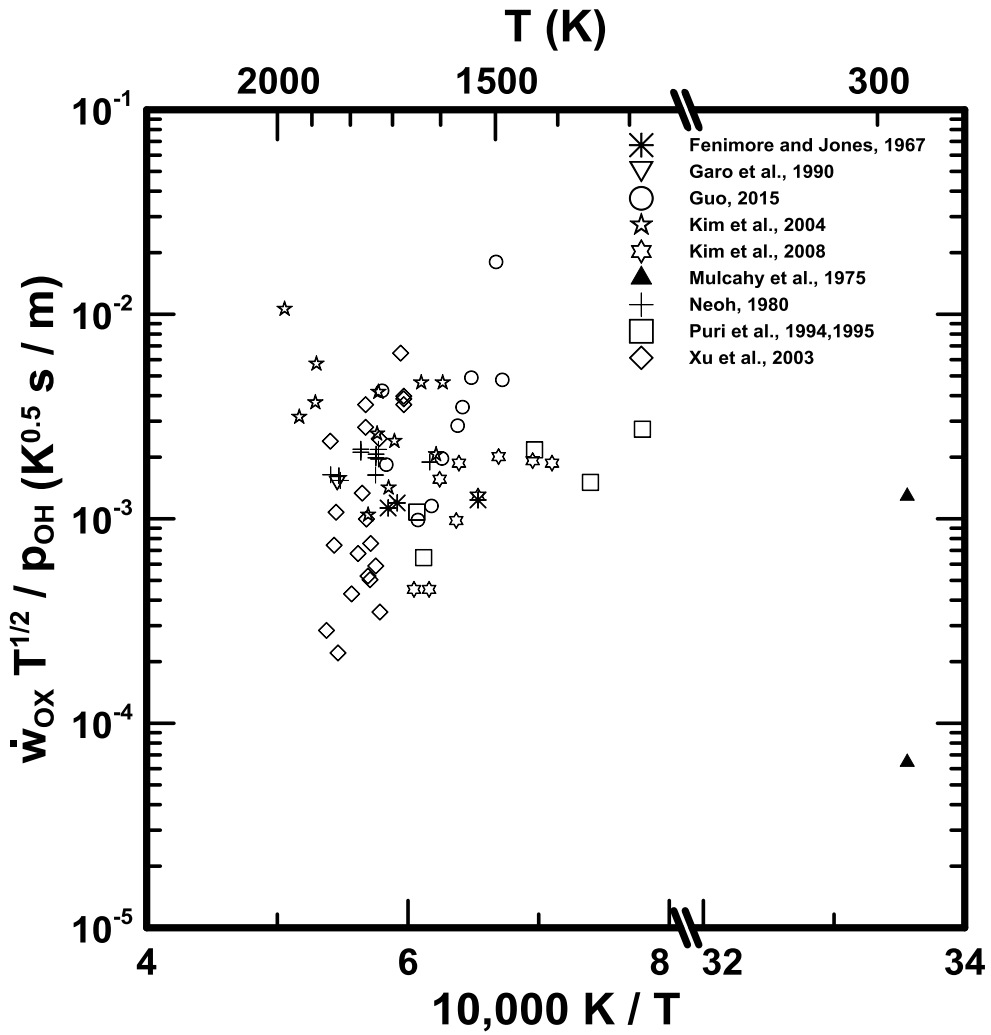

Figure 6-4 Arrhenius form plot of the oxidation rate from past studies versus the reciprocal of temperature, assuming the oxidation is by only OH. Also shown are the oxidation of carbon by OH at 298 K from Mulcahy et al.

6.4. Modeling Optimization

Most past studies show the existence of the O_2 activation energy. The activation energy for OH is negligible. The current study focuses on determining the appropriate A_{O2}, E_{O2}, and A_{OH} by maximizing the coefficient of determination in fitting the measured overall oxidation rates with the predictions. The uncertainties associated with each study's measurement (T, $\dot{w}_{ox}$, and p_i) were not available. In the current study, the experiment uncertainties from the past studies were treated as random noise. Optimization was performed with MatLab.

A_{O2}, $E_{A,O2}$, and A_{OH} were found to be 15.8 $K^{0.5}$ s / m, 195 kJ/mol, and 1.27×10^{-3} $K^{0.5}$ s / m, respectively. The resulting R^2 was 0.98. The optimized results were shown in Fig. 6-5. The A_{OH} corresponds to a constant collision efficiency of 0.10, which is close to the values reported by Fenimore and Jones [30], and Neoh et al. [12-14]. The activation energy E_{O2}, however, is higher than that reported by Lee et al. [19] (164 kJ/mol), and much higher than that used by Frenklach et al. [2, 42] (31.3 kJ/mol). The optimized oxidation mechanisms for O_2 and OH have an overall uncertainty of ±30% (95% confidence).

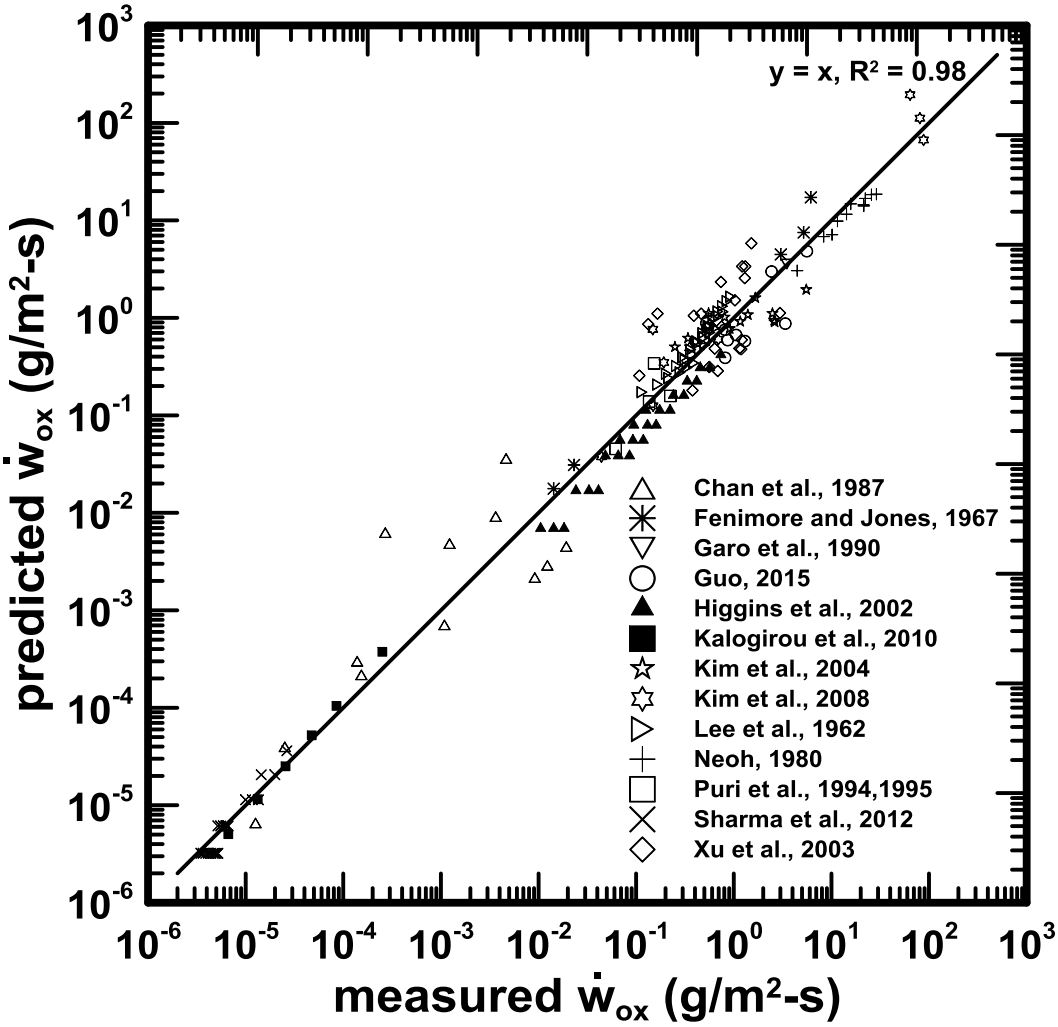

Figure 6-5 Comparison between the measured soot oxidation rate and the predictions using the model with the optimized A_{O2}, $E_{A,O2}$, and A_{OH}. The resulting R^2 is 0.98.

The sensitivity of the maximized R^2 to each variable was also tested and the results are shown in Fig. 6-6. For each variable (e.g., η_{OH}) value, its corresponding maximum R^2 was found by adjusting the other two variables (e.g., A_{O2} and $E_{A,O2}$). Each variable is normalized by dividing its value at maximum R^2. Due to the exponential correlation in Eq. (6-3), A_{O2} needs to adjust itself rapidly for any small changes in $E_{A,O2}$ for convergence. A_{O2} / A_{O2_max} was shown in a log abscissa.

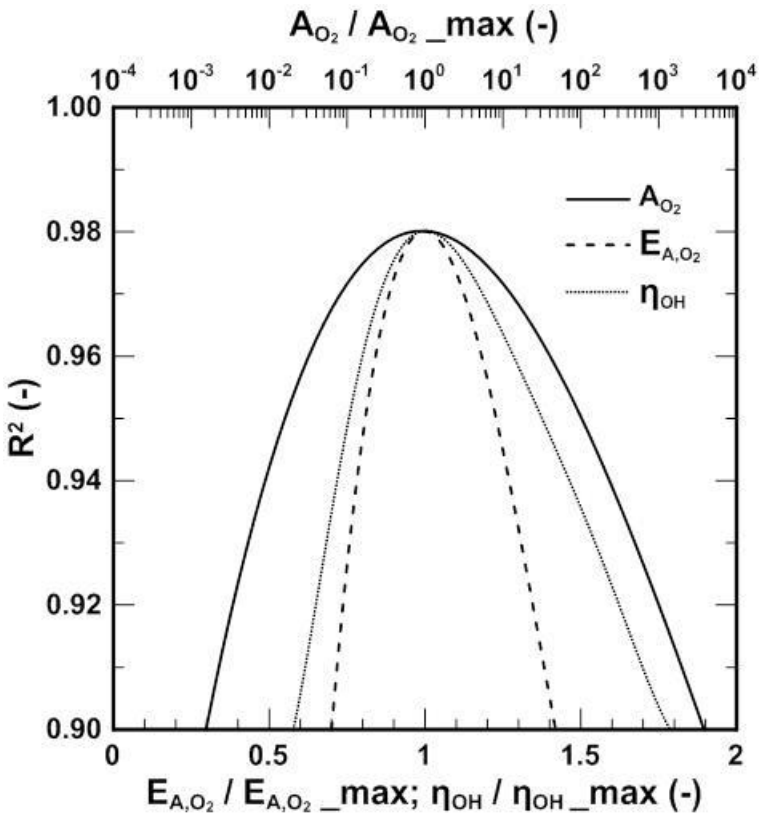

Figure 6-6 Sensitivity of the maximized R^2 to each variable.

The recommended soot oxidation mechanisms for O_2 and OH are:

$$\dot{w}_{ox,O_2} = \frac{1.58\times10^{9}\, p_{O_2}}{\sqrt{T}} \exp\left(-\frac{1.95\times10^{5}}{R_u T}\right), \text{(g/m}^2\text{-s)} \tag{6-6}$$

$$\dot{w}_{ox,OH} = \frac{1.27\times10^{5}\, p_{OH}}{\sqrt{T}} . \text{(g/m}^2\text{-s)} \tag{6-7}$$

Partial pressure is in bar, and temperature is in Kelvin. The correlations yield an overall estimation uncertainty of 30% (95% confidence).

6.5. Oxidation Mechanism Summary

Past experimental studies including 170 measurements of soot oxidation rates were examined. The measurements were correlated to yield new soot oxidation rates for O_2 and OH. The activation energy and the pre-exponential factors were determined by maximizing the R^2 in fitting the measured overall oxidation rates with the predictions. The resulting O_2 mechanism has an activation energy of 195 kJ/mol, and a pre-exponential factor of 15.8 $K^{0.5}$ s / m. The activation energy for OH with soot is negligible. The OH mechanism has a collision efficiency of 0.10. These soot oxidation mechanisms for O_2 and OH match the measured soot oxidation rates with a R^2 of 0.98.

Chapter 7: Soot Oxidation Rates

7.1. Theory

Soot oxidation rates are normally expressed as the mass of soot oxidized per unit surface area per unit time. Typical soot oxidation rates in diffusion flames are on the order of 1 g/m^2-s [34]. Soot oxidation rates in flames can be found from conservation of soot mass along a soot pathline.

The upward soot flux at a given height is

$$\dot{m}_s = \rho_s u \int_{-\infty}^{\infty} \pi r f_s(r) dr \,, \tag{7-1}$$

where f_s is local soot volume fraction, $\dot{m}_s$ is soot flux, r is radius, u is velocity, and ρ_s is soot density, taken here to be 1860 kg/m^3 [97]. The integrated soot volume fraction F_s can be directly obtained as derived in Section 4. Equation (7-1) can be simplified as:

$$\dot{m}_s = \rho_s u F_s \,. \tag{7-2}$$

The generalized formulation of soot oxidation rate is derived below. The system considered here consists of a control volume between heights 1 and 2 with an average convection time Δt as depicted in Fig. 7-1.

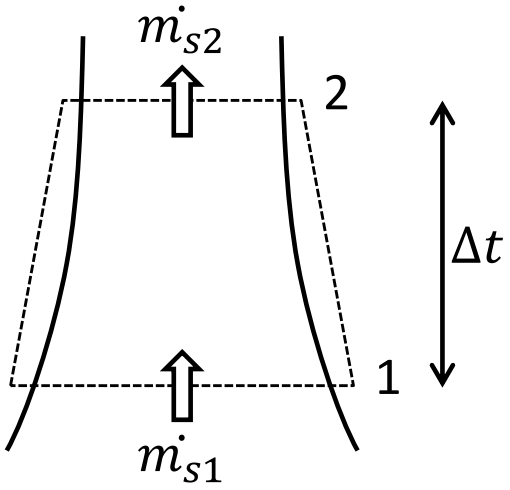

Figure 7-1 Macroscopic control volume for soot oxidation rate analysis.

Within the control volume the change of soot mass is

$$\Delta m_s = \left(\dot{m}_{s1} - \dot{m}_{s2}\right)\Delta t\,. \tag{7-3}$$

Soot surface area can be found from soot primary particle diameter and primary soot particle number density (number of primary soot particles per unit volume). The soot primary particle diameters were assumed to follow either the monodisperse distribution as in Refs. [47, 48], or the lognormal distribution as in Ref. [12]. Derivations of both cases were performed to compare the distribution effect on the specific soot oxidation rate.

A. If the soot particle diameters are monodisperse

For soot particles with a monodisperse distribution, the volume of soot can be calculated by assuming that the particles are not or merely touched:

$$f_s = n_{p,a}\pi d_{p,a}^3 \big/ 6\,, \tag{7-4}$$

where n_p is the particle number density. Subscript a denotes the arithmetic mean. The soot surface area per unit volume is

$$S = n_{p,a}\pi d_{p,a}^2 = 6 f_s / d_{p,a} \,. \tag{7-5}$$

Because the soot volume fraction is spatially resolved here, the total soot surface area in the control volume can be found from

$$\overline{S} = u\Delta t \int_{-\infty}^{\infty} \pi r \left[6 f_s(r) / d_{p,a} \right] dr = 6u\Delta t F_s / d_{p,a} \,. \tag{7-6}$$

The soot oxidation rate $\dot{w}_{ox}$ in the control volume is

$$\dot{w}_{ox} = -\lim_{\Delta t \to 0} \frac{\Delta m_s}{\overline{S}\Delta t} \,. \tag{7-7}$$

Combining Eqs. (7-3), (7-6), and (7-7) yields:

$$\dot{w}_{ox} = -\frac{d_{p,a}\rho_s}{6uF_s} \frac{d(uF_s)}{dt} \,. \tag{7-8}$$

B. If the soot particle diameters have a lognormal distribution

The lognormal distribution of soot particle diameter d_p is equivalent to the normal distribution of $\ln(d_p)$. The probability density function is:

$$f(d_p) = \frac{1}{\sqrt{2\pi}} \exp\left\{ -\frac{\left[\ln(d_p) - \ln(d_{p,g})\right]^2}{2\sigma^2} \right\}, \tag{7-9}$$

where σ is the standard deviation of $\ln(d_p)$, and the subscript g denotes geometric mean. Equations (7-4) and (7-5) become:

$$f_s = \left[n_{p,g}\pi \int_0^{\infty} d_p^3 f(d_p) d(d_p) \right] \Big/ 6 = \left[n_{p,g}\pi d_{p,g}^3 \exp\left(4.5\sigma^2\right) \right] / 6 \,, \tag{7-10}$$

$$S = n_{p,g}\pi\int_0^\infty d_p^2 f\left(d_p\right)d\left(d_p\right) = n_{p,g}\pi d_{p,g}^2 \exp\left(2\sigma^2\right). \tag{7-11}$$

Combining Eqs. (7-10) and (7-11) yields:

$$S = 6 f_s / \left[d_{p,g} \exp\left(2.5\sigma^2\right)\right]. \tag{7-12}$$

Following the steps in the monodisperse case the soot oxidation rate is:

$$\dot{w}_{ox} = -\frac{d_{p,g}\rho_s \exp\left(2.5\sigma^2\right)}{6uF_s}\frac{d\left(uF_s\right)}{dt}. \tag{7-13}$$

Equation (7-8) and (7-13) yield soot oxidation rates that agree within 20% for the current measurements. A detailed examination of the distribution found that the soot diameter distribution is between normal and lognormal. The soot oxidation rate in the current study was calculated with Eq. (7-13), assuming a lognormal distribution to incorporate the large variance in soot diameter. The temporal derivatives of Eq. (7-13) were found from linear fits of the measurements within a maximum height of 10 mm.

The soot oxidation expressions in Refs. [34, 40, 41, 47, 48], assuming monodisperse soot primary particles, is:

$$\dot{w}_{ox} = -\frac{\rho d_{p,a}\rho_s}{6 f_s}\frac{d\left(f_s/\rho\right)}{dt}. \tag{7-14}$$

This expression only explored the soot volume fraction at the centerline, assuming soot follows the streamline. The temperature effect due to the ideal gas law was corrected. However, transport of soot along the radial direction was neglected. Preliminary tests with a similar flame setup showed that Eq. (7-14) yields negative soot oxidation rates

along flame centerline within the hydrocarbon-free region, suggesting considerable transport of soot in the radial direction.

7.2. Results and Discussion

Figure 7-2 shows the measured soot flux from Eq. (7-2), and soot oxidation rate from Eq. (7-13), versus height. Soot flux was observed to decrease with height owing to oxidation. Soot burnout is about 90% at 55 mm height, as estimated from the soot flux. Soot oxidation rates are between 0.5 – 6 g/m^2-s. The rates are comparable to the range (0.5 – 2 g/m^2-s) measured by Xu. et al. [34] in diffusion flames at 1 atm. The soot oxidation rate initially increases rapidly with height, peaking at 13 mm height. This coincides with the peak temperature region on the axis, as shown in Fig. 4-8. The oxidation rate decreases to 0.5 g/m^2-s at 20 mm height, which coincides with the lowest O_2 concentration location.

The soot oxidation rates can be predicted from the mechanism for O_2 in Eq. (6-6), and for OH in Eq. (6-7). Temperature was from ratio pyrometry, p_{O2} was from the GC, and p_{OH} was from the complete equilibrium assumption. The four-reaction partial equilibrium yielded soot oxidation rates higher than the overall measured soot oxidation rates by approximately one order of magnitude, implying that the local OH overshooting is suppressed and in a state closer to complete equilibrium. The predictions are shown in Fig. 7-3. Due to the relatively high O_2 activation energy (195 kJ/mol) observed from past studies, the contribution of O_2 to the total soot oxidation strongly depends on temperature. At heights between 10 – 20 mm, where either O_2 or temperature is high, the predicted

oxidation by O_2 is comparable to or above that by radical OH. Above, the oxidation by O_2 is between 0.3 – 0.5 g/m^2-s, due to the competing effect of an increasing O_2 and a decreasing temperature. OH concentration is significantly reduced at lower temperatures, resulting in a continuous decrease of oxidation rate.

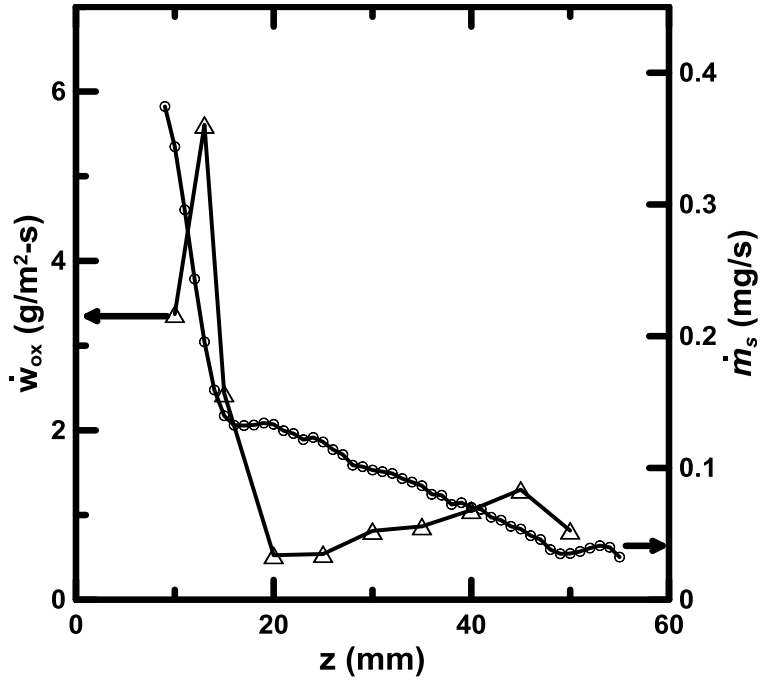

Figure 7-2 Measured soot flux and soot oxidation rate versus height.

The overall predictions by both O_2 and OH are compared with the measurements in Fig. 7-4. The model successfully predicts the peak soot oxidation rates and the agreement is better than 50% at heights between 13 – 40 mm. Above and below this the agreement is worse. Predictions are within ±80% of the measurements.

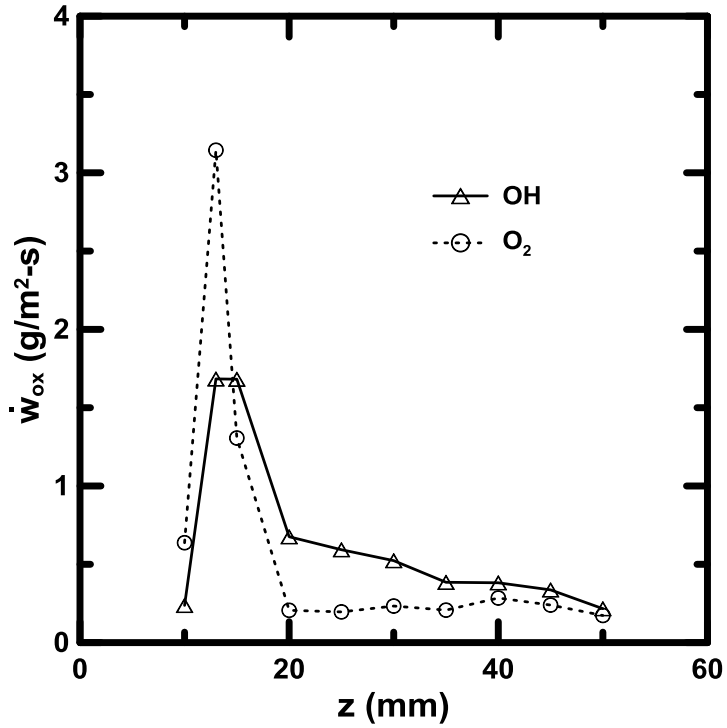

Figure 7-3 Predicted soot oxidation rate by O_2 and OH versus height.

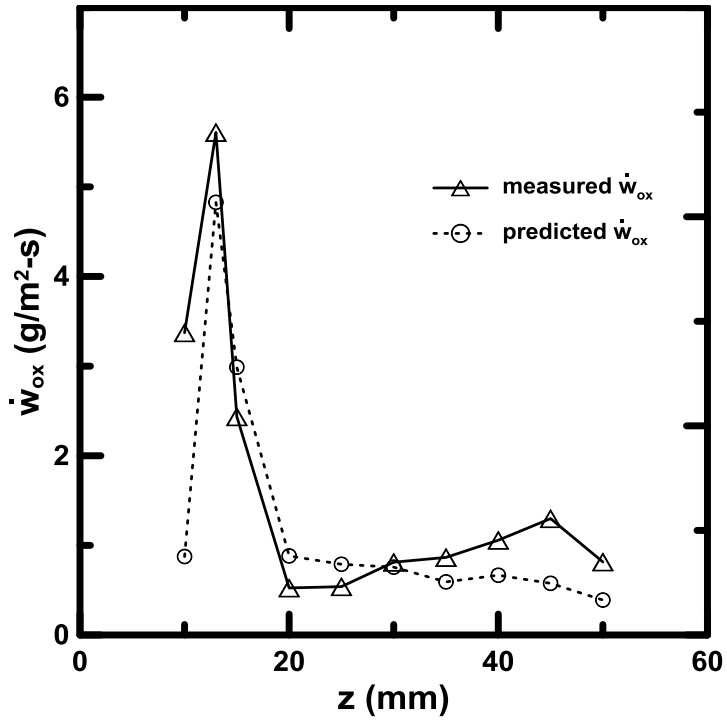

Figure 7-4 Comparison of the measured and predicted soot oxidation rate versus height.

The uncertainties in the measured oxidation rate arise from uncertainties in soot concentration, soot diameter, and velocity, and were estimated following Ref. [38]. Uncertainties were between ±30–70%, except for heights at 20 mm, where the oxidation rate has an uncertainty higher than ±100%. Similarly, the uncertainties in the predicted soot oxidation rates by O_2 are less than ±50%, as estimated from the propagated uncertainties in p_{O2} and temperature. Estimating OH in a lean sooting flame with the complete equilibrium has an experimental uncertainty of ±40%. Due to the weak dependence of oxidation rate on temperature, as shown in Eq. (6-7), the estimated uncertainties in the predicted soot oxidation rates by OH are also ±40%.

7.3. Summary

Soot oxidation rates were found from the measured soot concentration, velocity, and soot diameter, assuming a lognormal diameter distribution. The measured oxidation rates were between 0.5 – 6 g/m^2-s, and peaked at 13 mm height. Soot oxidation was also predicted using the developed mechanisms for O_2 and OH. The prediction yielded overall soot oxidation rate between 0.4 – 5 g/m^2-s, and its peak location coincided with the measured peak location. Predictions are within ±80% of the measurements.

Chapter 8: Conclusions and Recommendations

8.1. Summary and Conclusions

The objectives of the present work were to study soot oxidation in a hydrocarbon-free environment where soot oxidation was separated from soot formation. The work was motivated by the importance of soot on practical combustion devices, and the large uncertainty recently found in soot numerical modeling.

A ternary flame system was developed to incorporate two customized burners (Chapter 2). A soot column from the hydrocarbon diffusion flame was burned upon passing through the hydrogen diffusion flame supported by a ring burner. The soot flame was laminar, steady, axisymmetric, and freely accessible for optical and sampling diagnostics.

Optical diagnostics were developed to measure soot temperature and soot volume fraction in flames (Chapter 3). Soot temperature was measured with ratio pyrometry at 450, 650, and 900 nm, followed by deconvolution. Soot volume fraction was measured with laser extinction at 632.8 nm, followed by deconvolution. The diagnostics were tested with an axisymmetric steady laminar diffusion flame.

The soot flame was characterized by measuring its temperature, soot volume fraction, axial velocity, soot primary particle diameter, and major species concentrations (Chapter 4). Temperatures and soot volume fractions were determined with optical diagnostics. Integrated soot volume fractions were determined directly from the laser

extinction without deconvolution. Axial velocities were measured with high speed imaging and flow visualization. Soot primary particle diameters were measured from thermophoretic sampling and analyzed with TEM. Gases were sampled isokinetically. Water vapor concentration was determined with desiccant gravimetry. Other stable species were analyzed with GC and a TCD detector.

OH radical was estimated from the measured stable species concentration and temperature, assuming complete equilibrium (Chapter 5). The equilibrium condition in the soot flame was discussed by comparing the completely-equilibrated OH with that estimated from the partial equilibrium assumptions (four-reaction, three-reaction, and catalyzed reaction).

The soot oxidation mechanisms were analyzed with the measurements from the past studies (Chapter 6). Oxygen and OH radical were assumed to be the two main soot oxidants in flames. The past studies include 170 measurements in premixed flames, diffusion flames, TGA, tube furnace, flow reactor, etc. The temperatures cover a range from 800 – 2000 K. The measurements were correlated to yield new soot oxidation rates for O_2 and OH. The activation energy and the pre-exponential factors were determined by maximizing the R^2 in fitting the measured overall oxidation rates with the predictions. The developed oxidation mechanism for O_2 involves activation energy of 195 kJ/mol. The new OH mechanism has a collision efficiency of 0.10.

In the soot flame, the soot oxidation rate expressions were updated with the integrated soot volume fraction, assuming lognormal particle distribution (Chapter 7). Soot oxidation rates were calculated using the measured soot diameter, soot concentration,

and velocity. The soot oxidation rates were also predicted using the developed mechanisms for O_2 and OH, with the measured temperature and O_2 concentration, and the estimated OH concentration. The predictions agree within ±80% of the measurements.

8.2. Recommendations for Future Study

The following recommendations for future work in soot oxidation are presented.

The determination of soot particle diameter with TEM requires tremendous time in image post processing. The detection of primary particle is subjective as these particles are not perfectly spherical and normally overlapped. A more advanced image processing application can be developed to facilitate particle detection with minimal labor effort and subjective factors. Surface area loss from particle overlapping can be corrected. Particle number density and agglomerate size can also be found from the TEM image.

The design of this ternary flame system allows soot compositions and morphologies, soot concentration, temperature, gas compositions, etc. to be adjusted independently, by varying the fuel in the coflow burner and ring burner. Other fuels, such as propane ethylene, and acetylene, should be considered to examine possible fuel effects. The propylene flow rates could be reduced for lighter soot loading in the soot column to simplify the sampling for GC and water concentration measurements. The column diameter, maximum soot concentration, and absence of lateral motion could be optimized using variations in fuel and air flow rates and fuel port diameter. The soot to be considered in this work could be either mature or early. Columns of early soot could be

generated by placing a wire mesh in the propylene flame to quench it. The oxidation rates of early soot will likely be different, as it has different compositions and morphologies.

The ring burner flames could be adjusted to examine soot oxidation by OH in the near absence of O_2 and by O_2 in the near absence of OH. Air could be replaced by O_2 in some tests to increase the temperatures in the soot flames. Here are several ways of achieving these objectives. The initial ternary flame could involve hydrogen issuing from the ring burner, but at lower and higher flow rates. Low hydrogen flow rates will lead to low OH concentrations and high O_2 concentrations in the soot flame. Conversely high hydrogen flow rates will lead to high OH concentrations and low O_2 concentrations. This would aid in the development of OH and O_2 soot oxidation rate models. Corrections could be made for soot oxidation by O, CO_2, and H_2O. The next gases to be tested in the ring burner could be lean premixtures. For example, lean premixtures of C_2H_2 and air at low flow rates will not produce soot and yet will largely remove OH from the soot flames. Lean premixtures of H_2 and O_2 will extend the soot oxidation regions to higher temperatures. It was found that flowing pure O_2 into the ring burner is not sufficient to oxidize the soot. However, O_2 with a small amount of C_2H_2 or H_2 should be sufficient to oxidize the soot in the near absence of OH. Other gases to be considered for use in the ring burner could include CO (with 1% H_2) and N_2O_2. Both choices would nearly eliminate the presence of OH in the soot flame.

Appendix A. Deconvolution and Spectral Behavior

Onion peeling and Abel transform are two common deconvolution algorithms in reconstructing local properties from projections in a axisymmetric domain [70]. This section will briefly introduce these two methods and compare the difference in deconvolution.

The onion peeling method is based on numerical approximation. It is assumed that the entire domain can be divided into a series of concentric rings. The properties within each ring are assumed to be constant. Therefore, the local property can be calculated with the projection and a reconstruction matrix, following [70]:

$$F(\zeta_j) = \sum_{i=j}^{\infty} [s_{ji}]^{-1} P(x_i), \qquad r_j < \zeta_j < r_{j+1} \tag{A-1}$$

where F is the local property, P is the projected property, r is the radial direction, x is the direction perpendicular to the cord, and ζ is the radial location between two adjacent rings. s_{ij} is a matrix of the length of the i-th cord in the j-th ring:

$$s_{ij} = 2\left(\sqrt{r_{j+1}^2 - x_i^2} - \sqrt{r_j^2 - x_i^2}\right) = 2\left(\sqrt{[x_i + \Delta(j-i+1)]^2 - x_i^2} - \sqrt{[x_i + \Delta(j-i)]^2 - x_i^2}\right). \tag{A-2}$$

The schematic for the onion peeling method is shown in Fig. A-1.

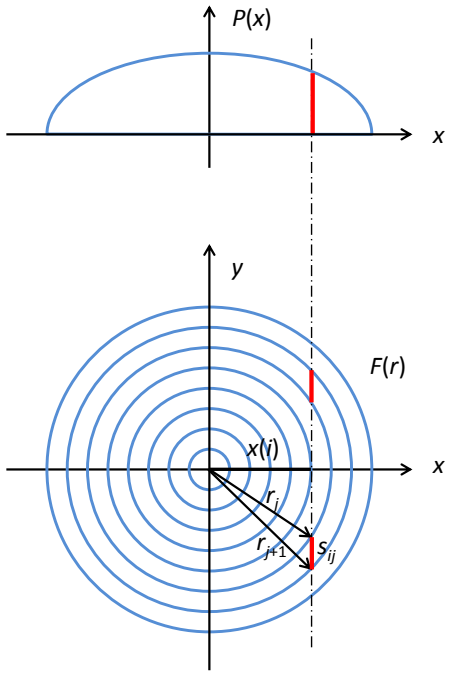

Figure A-1 The schematic for the onion peeling method.

On the contrary, the Abel transform method is based on the analytical solution of the strict integration form, following:

$$F(r) = -\frac{1}{\pi}\int_r^{\infty} \frac{P'(x)}{\sqrt{x^2 - r^2}} dx \tag{A-3}$$

As suggested in Ref. [70], directly using Eq. (A-3) is problematic because: 1, direct derivative magnifies the noises in the projection signal; 2, the denominator has singularity at $x = r$. Simply neglecting the data at $x = r$ will cause significant error. To avoid these, equation (A-3) was modified to [70]

$$F(r) = -\frac{1}{\pi}\int_r^{r+L} \frac{P(x) - P(r)}{\left(x^2 - r^2\right)^{3/2}} x dx - \frac{1}{\pi}\int_{r+L}^{R} \frac{P(x)}{\left(x^2 - r^2\right)^{3/2}} x dx + \frac{P(r)}{\pi\sqrt{L(2r+L)}}, \tag{A-4}$$

where L is the boundary of the lower integration limit, and R is the limit of the domain (e.g., flame radius). The first part can be solved with an open type numeric integration

(e.g., four-point Steffensen's formula [98]), using Eq. (A-5); the second part was solved with a closed type numeric integration (e.g. Simpson's rule), using Eq. (A-6).

$$\int_a^b f(x)dx = \frac{5L}{24}\left[11f(a+L)+ f(a+2L)+ f(a+3L)+11f(a+4L)\right],\ L=\frac{b-a}{5} \tag{A-5}$$

$$\int_a^b f(x)dx = \frac{b-a}{6}\left[f(a)+4f\left(\frac{a+b}{2}\right)+ f(b)\right]. \tag{A-6}$$

It is noted that, the first and the second term in Eq. (A-4) quickly increases as x approaches the boundary. Integrating the second term with a less strict method (e.g., Trapezoidal rule) causes significant error.

Alternatively, Abel transform in Eq. (A-3) was also approximated using [99]:

$$F(r_i) = \frac{-2}{\pi}\sum_{j=i}^{R-1}\frac{P(j+1)-P(j)}{r_{j+1}^{\ 2}-r_j^{\ 2}}\left[\left(r_{j+1}^{\ 2}-r_i^{\ 2}\right)^{1/2}-\left(r_j^{\ 2}-r_i^{\ 2}\right)^{1/2}\right]. \tag{A-7}$$

The onion peeling method in Eq. (A-1) and the Abel transform methods in Eq. (A-4) and (A-7) were discretized and programed using MatLab. Prescribed temperature and soot volume fraction profiles were used to generate an axisymmetric intensity signal, in order to test the methos:

$$T(r) = 1500 + 31r^2\ , \tag{A-8}$$

$$f_s(r) = 10\exp\left[-6(r-3)^2\right]. \tag{A-9}$$

The prescribed temperature and soot volume fraction profiles were shown in Fig. A-2.

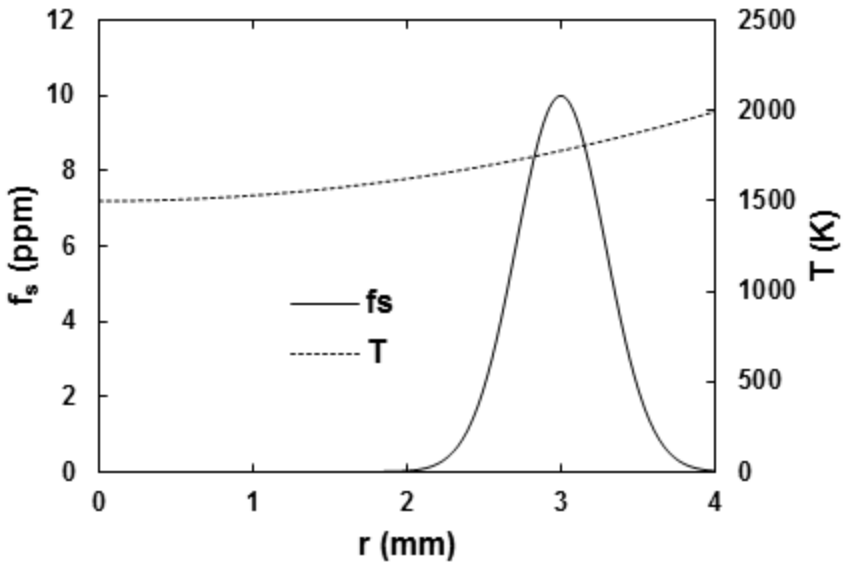

Figure A-2 Prescribed temperature and soot volume fraction profiles for deconvolution test.

The radial emission intensity can thus be analytical calculated using Eq. (3-4). Random optical parameters were used. The real line-of-sight projection was analytically integrated with the radial property. The radial distribution and the line-of-sight projection are shown in Fig. A-3. The units are arbitrary. The spatial resolution was chosen to be 0.1 mm/pixel, which was typical with the current imaging system.

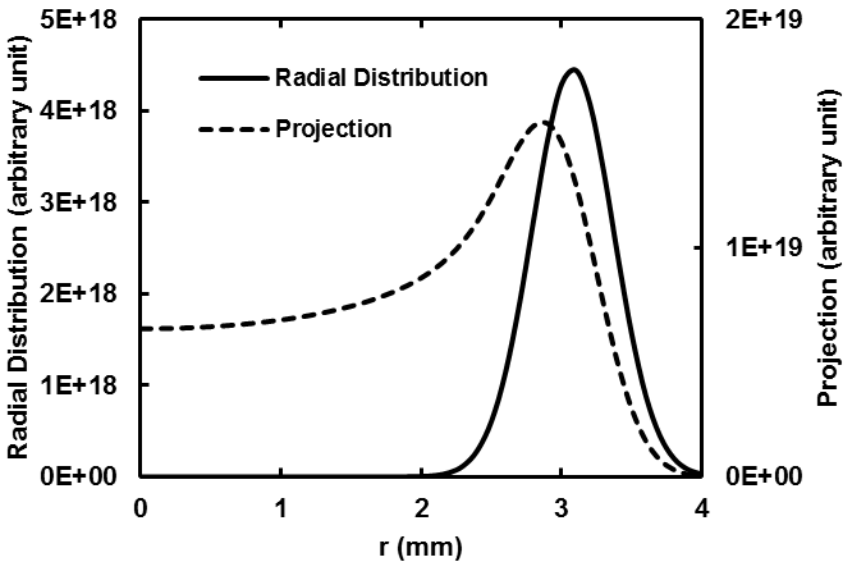

Figure A-3 Analytically calculated radial distribution and the line-of-sight projection.

The deconvolved results using onion peeling in Eq. (A-1), Abel transform (a) in Eq. (A-4) and Abel transform (b) in Eq. (A-7) were compared with the true value in Fig. A-4. In the signal peak region, Abel (b) is able to reconstruct the peak information better than the other methods. In onion peeling, the round-off error in approximating s_{ij} accumulates, and results in a small peak when approaches the centerline. This round-off error affects the deconvolution accuracy, especially when the detection noise is involved. At radius of 0 – 2 mm, the real distribution decreases exponentially when approaching centerline, and none of these algorithms is able to reconstruct this behavior. Ratio pyrometry using the deconvolved signal at this region is subject to a lower signal/noise ratio, and the uncertainty in deconvolution.

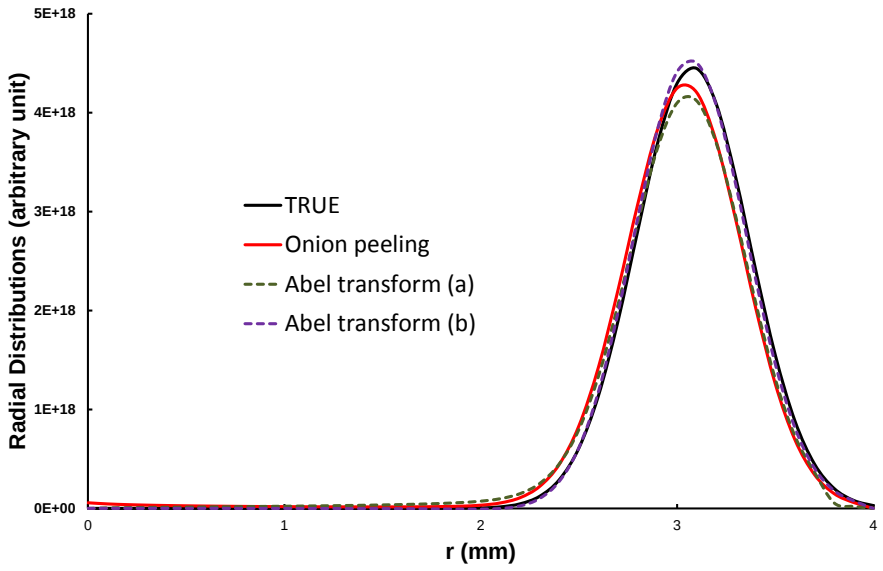

Figure A-4 Comparison of the deconvolved results using different algorithms with the true prescribed radial distribution.

Spectral behavior of the soot emission was noticed. Soot flickering is inevitable in flames. Whereas temporal averaging of the detected irradiance signal with multiple exposures has a broaden effect on flame diameter, comparing irradiance from a flickering flame (1 – 2 pixel off) results in significant uncertainty, especially near the peak location. In the above case, off by one pixel (0.1 mm) results in intensity difference by up to 30%. Aligning the detected emission intensity profile to correct for that flickering effect is intriguing but subjective. Since the local irradiance is a complicated function of temperature and soot volume fraction, aligning the peak locations of different wavelengths is problematic. Figure A-5 shows the irradiance profile for three wavelengths (450, 650, and 900 nm) in the above case, where the peak locations are found off by 5 pixels. Therefore, it is suggested that if the flame flickering affects the temperature measurement accuracy, alignment of the irradiance profiles should not be

merely based on the peak locations. Instead, both directions should be attempted until the best temperature agreement between pairs is observed.

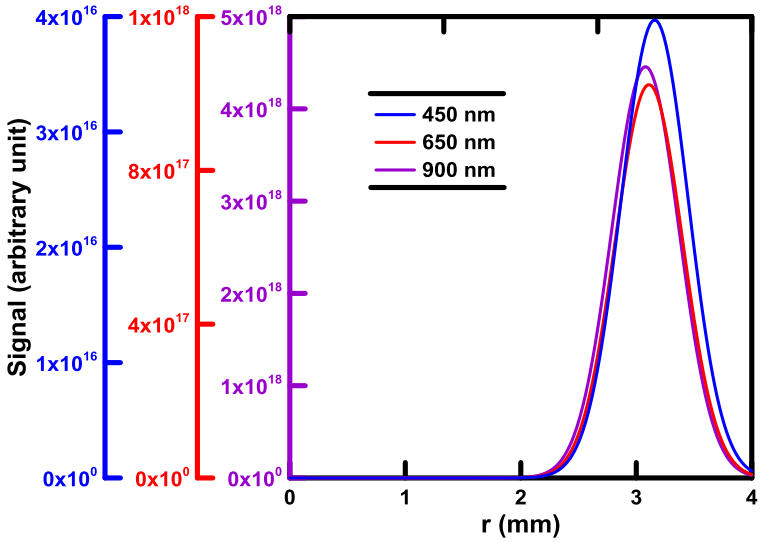

Figure A-5 Comparison of the calculated irradiance signal at 450, 650, and 900 nm.

The deconvolution algorithms involve differentiation. Noises in the detected projection signal are magnified after deconvolution. Therefore, data smoothing is highly recommended to arrest the noise level during deconvolution, and it should be performed prior to deconvolution. Changing the order of data smoothing and deconvolution yield different results [70].

Three different data smoothing algorithms were tested in the current study: low-pass filter, Gaussian filter, and Savitski-Golay (S-G) filter. The low-pass filter involves Fourier transform to convert the data in physical domain to frequency domain. The high frequency signals (recognized as noises in the current study) were removed by assigning a cut-off frequency (threshold). Signal with higher frequency was set to zero. The data was then reverted to the physical domain. Mirroring the signal prior to applying the low-pass filter helps reduce the sinusoidal oscillations. On the contrary, the Gaussian filter

smooths the data in the physical domain by applying a Gaussian function within a chosen rectangular window. However, there is trade-off between the smoothing effect and the data distortion, especially when the data has a sharp peak as shown in Fig. A-3. S-G filter is achieved by fitting adjacent data points in a chosen rectangular window with a low-degree polynomial by the method of least square fit. The sharp peak shapes can thus be conserved with minimal distortion [100]. Smoothing with these three algorithms shows that S-G filter worked the best for data in the current study.

Appendix B. Main Script for T calculation

```
%% obtain image information
% image input
RGB = imread('450.tiff'); % load image at 450,650,900nm
gray = mean(RGB,3); % flatten to grayscale, different from 'rgb2gray'
% crop image
x1=1000; % left location
y1=1; % upper location
x2=1500; % right location
y2=3700; % lower location **use the value at z=0
gray=gray(y1:y2,x1:x2);
[YL,XL]=size(gray);
% vertically smooth grayscale
win=21; % line thickness
sigmaY=10; % standard deviation for Gaussian filter
VSgray=zeros(YL,XL);
for i=1:XL
   VSgray(:,i)=GFilter(win, sigmaY, gray(:,i)); % Gaussian filter function
end

function sy=GFilter(win,sigma,y) % Gaussian filter function
xx=linspace(-win/2,win/2,win);
gF=exp(-xx.^2/(2*sigma^2));
gF=gF/sum(gF);
sy=conv(y,gF,'same');

% extract information at selected heights
res=0.021; % pixel resolution (mm/pixel)
del=1; % heights separation (mm)
dz=del/res; % separation pixel number (pixel)
N=floor((YL-1)/dz)+1; % number of heights
Ngray=zeros(N,XL);
for i=1:N
   Ngray(i,:)=VSgray(YL-round((N-i)*dz),:);
end
z=(N-1)*del:-del:0; % height (mm)
OUT=[z' Ngray];
dlmwrite('450.txt',OUT); % output height and grayscale

%% repeat for other wavelength

%% deconvolution
DATA=load('450.txt');
st=1/10; % shutter
```

```
ISO=200; % ISO
z=DATA(:,1); % height
N=length(z); % number of heights
yDATA=DATA(:,2:size(DATA,2)); % grayscale
L=length(yDATA(1,:));
t=0:L-1;
n=30; % input the n-th height
y=yDATA(n,:)';
SG_k=4; % polynomial order in S-G filter
SG_win=15; % window size in S-G filter, must be odd
sy=sgolayfilt(y,SG_k,SG_win); % apply S-G filter
res=2.1e-5; % m/pixel
adx=-38; % manually shift the center line by adx
% choose background, avoid flame region
y1=1;
y2=50;
y3=240;
y4=L;
t_line=[t(y1:y2) t(y3:y4)];
sy_line=[sy(y1:y2); sy(y3:y4)]';
line_ab = polyfit(t_line,sy_line,1);
sy0_line=line_ab(1)*t+line_ab(2); % linearly interpolate background noise
sy1=sy-sy0_line'; % subtract background noise
for i=1:L
   if sy1(i)<0
      sy1(i)=0; % remove negative value
   end
end
% average left and right signal
sy_left=flipud(sy1(1:round(L/2)+adx));
sy_right=sy1(round(L/2)+adx:L);
mL=min(length(sy_left),length(sy_right));
t_mL=0:(mL-1);
sy_ave=(sy_left(1:mL)+sy_right(1:mL))/2;
py_left=sy_left(1:mL);
py_right=sy_right(1:mL);
py_ave=sy_ave(1:mL);
x_c=90; % cutoff boundary
ppy_ave=py_ave(1:x_c);
aby_ave=HDeconv(res,ppy_ave); % deconvolution function

function aby=HDeconv(res,py) % deconvolution function
L=length(py);
fft=zeros(L);
for i=1:L
```

```
    for j=i:L-1
        fft(i,j)=-1/pi()*2*(py(j+1)-py(j))/(((j+1-1)*res)^2-((j-1)*res)^2)*...
            (sqrt(((j+1-1)*res)^2-((i-1)*res)^2)-sqrt(((j-1)*res)^2-((i-1)*res)^2));
    end
end

aby=sum(fft,2);
end

OUT=[z(n) 4501 ppy_ave'/(st*ISO)]';
filename=[num2str(z(n)) 'mm' '450.txt'];
dlmwrite(filename,OUT);

%% repeat for other wavelength

%% multiple image averaging not shown

%% T calculation
DATA1=load('40mm450.txt');
DATA2=load('40mm650.txt');
DATA3=load('40mm900.txt');
z=DATA1(1,2);
L1=length(DATA1(:,1))-1; % data length at each wavelength
L2=length(DATA2(:,1))-1;
L3=length(DATA3(:,1))-1;
r1=DATA1(2:end,1);
r2=DATA2(2:end,1);
r3=DATA3(2:end,1);
gs1=DATA1(2:end,2);
gs2=DATA2(2:end,2);
gs3=DATA3(2:end,2);
SubPix=2; % subpixel divider
res=2.1e-5/SubPix; % m/pixel, for shift and interpolation
r=0:res:max([r1;r2;r3]);
GS1=interp1(r1,gs1,r);
GS2=interp1(r2,gs2,r);
GS3=interp1(r3,gs3,r);
[maxGS2,Ind2]=max(GS2); % find the index of the peak location
ratio_12=GS1./GS2; % ratio
ratio_23=GS2./GS3;
ratio_13=GS1./GS3;
h=6.6256e-34; % Plank constant
c=3e8; % speed of light
k=1.38e-23; % Boltzmann constant
lamda1=449.45e-9; % wavelength
```

```
lamda2=649.05e-9;
lamda3=900.05e-9;
alpha=1; % dispersion coefficient
C12=(6.48*9.9)/(3.51*10.1); % from blackbody calibration(450/650)
C23=(1.71*8.5)/(6.48*9.9); % from blackbody calibration(650/900)
C13=(1.71*8.5)/(3.51*10.1); % from blackbody calibration(450/900)
T12=(h*c/k*(1/lamda2-1/lamda1))./log(ratio_12*C12*(lamda1/lamda2)^(5+alpha));
T23=(h*c/k*(1/lamda3-1/lamda2))./log(ratio_23*C23*(lamda2/lamda3)^(5+alpha));
T13=(h*c/k*(1/lamda3-1/lamda1))./log(ratio_13*C13*(lamda1/lamda3)^(5+alpha));
T_ave=(T12+T23+T13)/3; % T without alignment
del1=4; % shift distance (pixels) of GS1
del2=0; % use GS2 as the reference image, no shift of this image
del3=1; % shift distance (pixels) of GS3
GGSS1=zeros(1,length(r)); % shifted grayscale
GGSS2=GS2;
GGSS3=zeros(1,length(r));
for i=1:length(r) % 450 nm
   if del1==0
      GGSS1=GS1;
   else if del1>0
         GGSS1(1:del1)=GS1(1);
         GGSS1(del1+1:length(r))=GS1(1:length(r)-del1);
      else
         GGSS1(1:length(r)+del1)=GS1(-del1+1:length(r));
      end
   end
end
for i=1:length(r) % 900 nm
   if del3==0
      GGSS3=GS3;
   else if del3>0
         GGSS3(1:del3)=GS3(1);
         GGSS3(del3+1:length(r))=GS3(1:length(r)-del3);
      else
         GGSS3(1:length(r)+del3)=GS3(-del3+1:length(r));
      end
   end
end
rratio_12=GGSS1./GGSS2; % ratio
rratio_23=GGSS2./GGSS3;
rratio_13=GGSS1./GGSS3;
TT12=(h*c/k*(1/lamda2-1/lamda1))./log(rratio_12*C12*(lamda1/lamda2)^(5+alpha));
TT23=(h*c/k*(1/lamda3-1/lamda2))./log(rratio_23*C23*(lamda2/lamda3)^(5+alpha));
TT13=(h*c/k*(1/lamda3-1/lamda1))./log(rratio_13*C13*(lamda1/lamda3)^(5+alpha));
TT_ave=(TT12+TT23+TT13)/3; % T with alignment
```

Appendix C. Main Script for fs calculation

```
%% obtain image information
RGB1 = imread('I.tiff'); % shadowgraph image
Cgray1 = mean(RGB1,3); % flatten
% crop image
x1=1250; % left location
y1=1; % upper location
x2=1400; % right location
y2=3400; % lower location **use value at z=0
Cgray1=Cgray1(y1:y2,x1:x2);
[YL,XL]=size(Cgray1);
% vertically smooth grayscales
win=21; % input the line thickness
sigmaY=10; % standard deviation for Gaussian filter
VSgray1=zeros(YL,XL);
for i=1:XL
    VSgray1(:,i)=GFilter(win, sigmaY, Cgray1(:,i));
end
res=3.4e-2; % pixel resolution (mm/pixel)
del=1; % heights separation (mm)
dz=del/res; % seperation pixel number (pixel)
N=floor((YL-1)/dz)+1; % number of heights
Ngray1=zeros(N,XL);
for i=1:N
    Ngray1(i,:)=VSgray1(YL-round((N-i)*dz),:);
end
z=(N-1)*del:-del:0; % height information
OUT1=[z' Ngray1];
dlmwrite('I.txt',OUT1);

%% Axisymmetric and extinction
DATA1=load('I.txt'); % input data
yDATA1=DATA1(:,2:size(DATA1,2)); % grayscale
n=80; % input the n-th height
y1=yDATA1(n,:)';
L=length(y1);
t=0:L-1;
SG_k=6; % polynomial order
SG_win=15; % window size, must be odd
sy_SG1=sgolayfilt(y1,SG_k,SG_win); % apply S-G filter
sy1=sy_SG1;
adx=-3; % mannually shift the center line by adx
sy1_left=flipud(sy1(1:round(L/2)+adx));
sy1_right=sy1(round(L/2)+adx:L);
```

```
mL=min(length(sy1_left),length(sy1_right));
t_mL=0:(mL-1);
sy1_ave=(sy1_left(1:mL)+sy1_right(1:mL))/2;
py1_left=sy1_left(1:mL); % truncate the matrix into the same dimension
py1_right=sy1_right(1:mL);
py1_ave=sy1_ave(1:mL);
% choose background, avoid flame region
x0=1;
x1=40;
x2=120;
xL=L;
t_line=[t(x0:x1) t(x2:xL)];
sy1_line=[sy1(x0:x1); sy1(x2:xL)]';
line_ab = polyfit(t_line,sy1_line,1);
sy0_line=line_ab(1)*t+line_ab(2); % linearly interpolate background signal
Ratio=sy0_line./sy_SG1';
ratio_left=fliplr(Ratio(1:round(L/2)+adx));
ratio_right=Ratio(round(L/2)+adx:L);
ratio_ave=(ratio_left(1:mL)+ratio_right(1:mL))/2;
Ratio_left=ratio_left(1:mL); % truncate the matrix into the same dimension
Ratio_right=ratio_right(1:mL);
Ratio_ave=ratio_ave(1:mL);
x_c=30; % cutoff boundary
res=3.4e-5; % input pixel resolution
lamda=632.8e-9; % laser wavelength
Em=4.9; % refractive index
py=log(Ratio_ave(1:x_c));
LL=length(py);
aby=HDeconv(res,py); % deconvolution
fs=lamda*aby/Em*1e6; % soot volume fraction units in ppm (*1e6)
inte_fs=2*log(Ratio_ave)*lamda/Em*1e6*1e3*res*1e3; % inte fs units in ppm*mm^2
inte_fs(x_c:mL)=0;
Inte_fs=sum(inte_fs);
```

Appendix D. Preliminary Flame Diagnostics

Flame diagnostics were also performed for the preliminary flames (1) and (2). Temperature, soot volume fraction, and velocity were measured for both flames.

Figure D-1 shows measured soot temperatures for both flames. In flame 1, the maximum temperature, 1800 K, was found near the axis where the hydrogen flame crosses. This is lower than the adiabatic hydrogen flame temperature, due to soot radiation. Higher, temperature decreases gradually to 1350 K. In flame 2, temperature is generally lower.

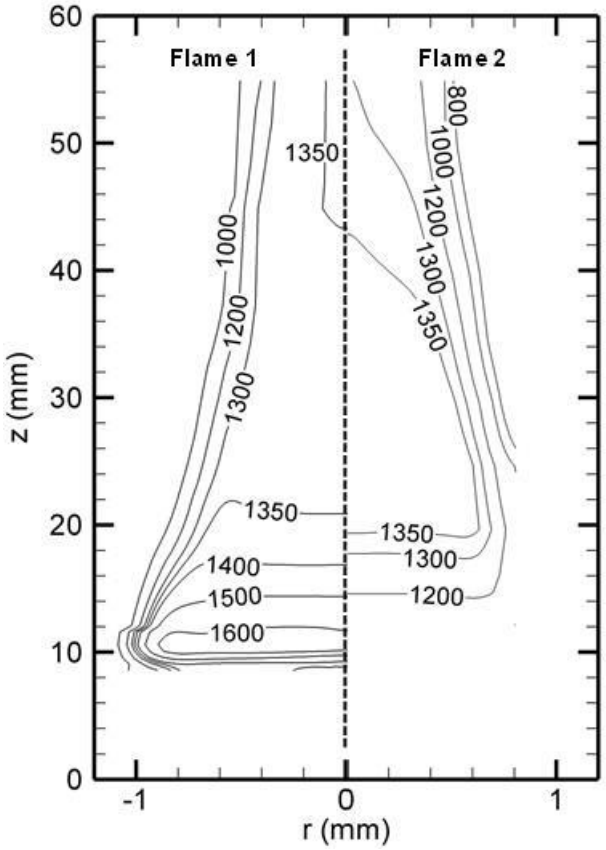

Figure D-1 Contour plot of temperature for preliminary flame (1) and (2).

Figure D-2 shows the measured soot volume fractions for both flames. Soot volume fraction is between 30-70 ppm on centerline. At low heights decreases of soot volume fraction with the flame height were observed. At heights above 20 mm in both flames, the soot volume fraction near the centerline increases with the flame height due to the narrowing of the soot column.

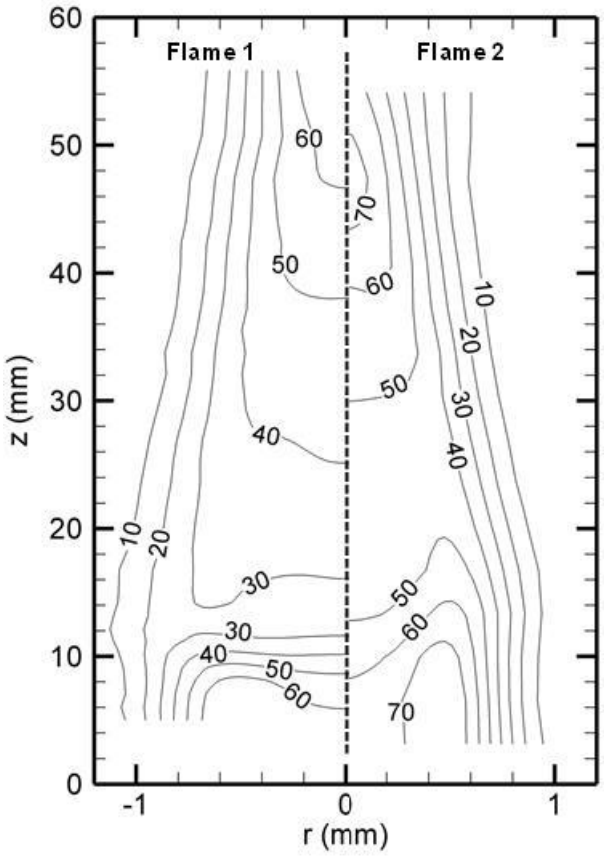

Figure D-2 Contour plot of soot volume fraction for preliminary flame (1) and (2).

Figure D-3 shows the axial soot velocity for both flames. In both flames, speed increases with height due to buoyancy, although the acceleration of flame 1 is greater that of flame 2 owing to the greater buoyancy of the larger hydrogen flame.

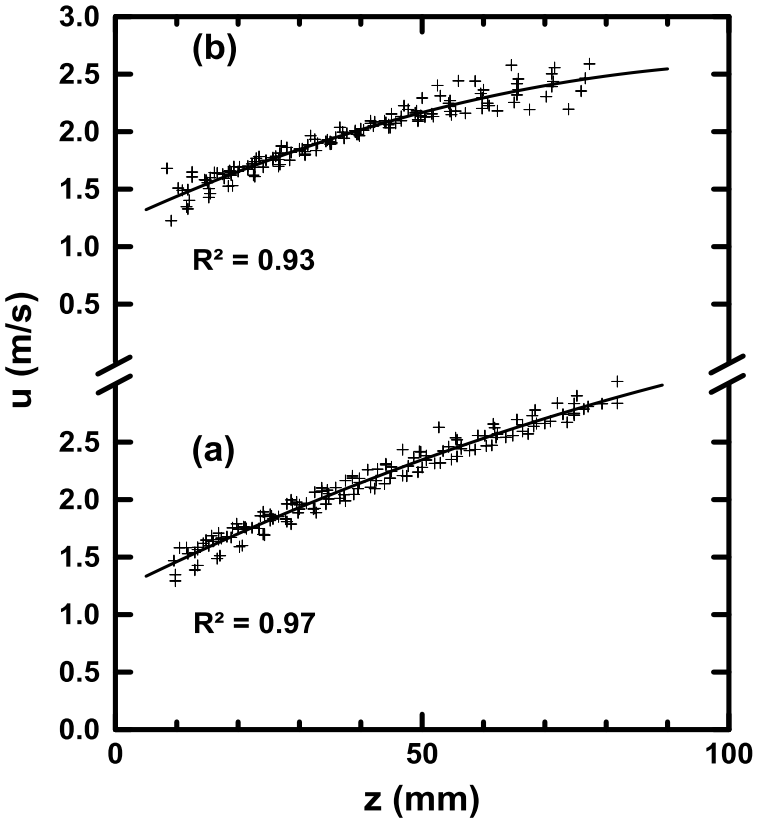

Figure D-3 Measured velocity for preliminary flame 1 (a) and 2 (b) versus height.

The calculated soot flux for both flames is shown in Fig. D-4. In flame (1) where flame temperature is generally higher, soot flux is nearly constant at heights between 15 – 25 mm, indicating that soot oxidation is suppressed within this region. This region corresponds to the rich region inside the hydrogen ring flame. On the contrary, in flame (2) where flame temperature is lower, soot flux continuously decreases, indicating continuous soot oxidation.

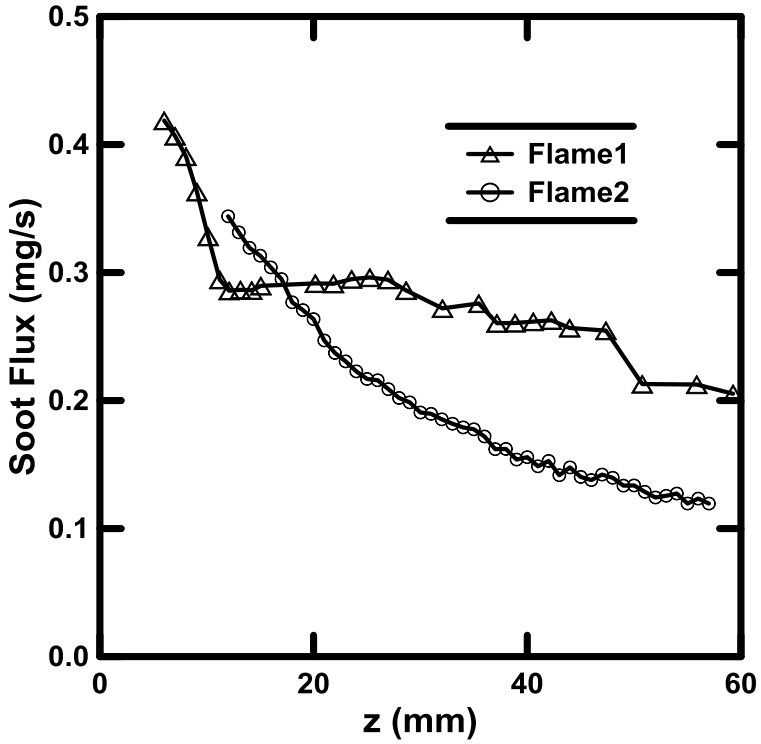

Figure D-4 Measured soot flux for preliminary flame (1) and (2) versus height.

Soot primary particle diameter was only measured for flame (2), where considerable soot oxidation was detected over 50 mm height. The results are shown in Fig. D-4.

The measured soot concentration, soot primary particle diameter, and velocity were used for calculating the soot oxidation as shown in Fig. D-5. The measured soot oxidation rates are between 0.05 – 0.4 g/m^2-s.

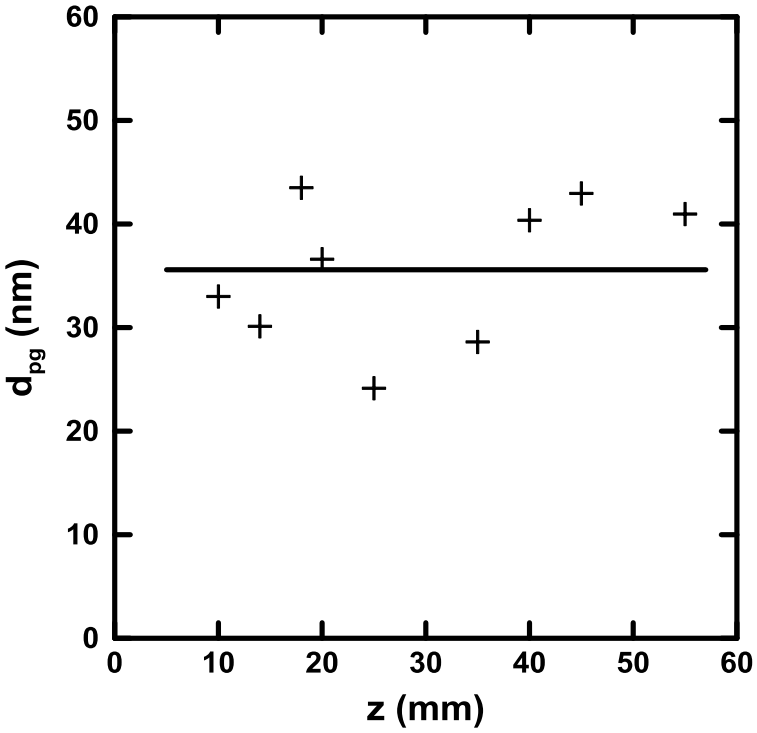

Figure D-5 Measured soot primary particle diameter for flame (2) versus height.

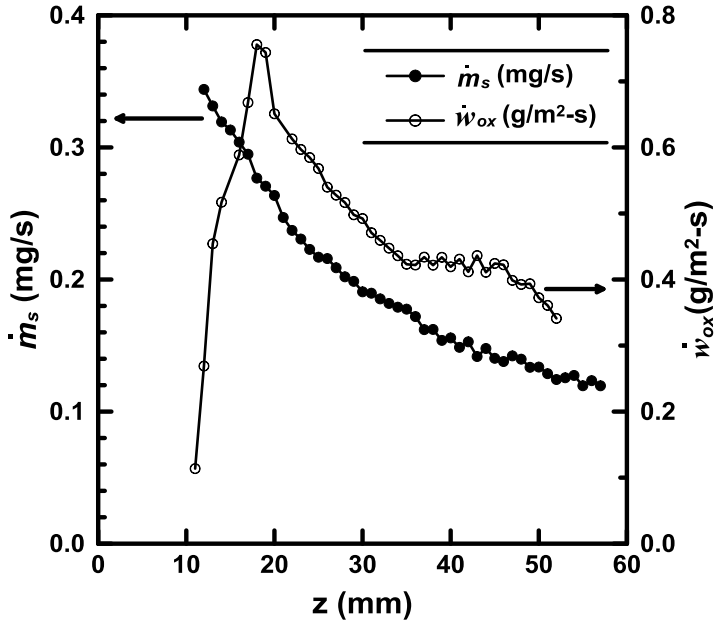

Figure D-6 Measured soot flux and soot oxidation rate for flame (2) versus height.

Appendix E. GC Calibration

The relative concentration of each gaseous compound was calculated by first calibrating the GC with different volumes of gas mixture (Air Liquide). The composition concentrations of the calibration gases were listed in Table E-1.

Table E-1 List of calibration gas and composition concentration.

Mixture	H_2	He	O_2	N_2	CO	CH_4	CO_2
1	0.495	0	0.520	97.963	0.520	0	0.502
2	4.02	71.93	5.01	5.00	5.00	4.02	5.02
3	0	0	0	93.95	3.03	0	3.02
4	0	0	0	70	15	0	15
5	0	0	21.77	78.23	0	0	0
6	25	0	0	75	0	0	0

The calibration results were summarized in Fig. E-1 to E-5. Coefficients of determination (R^2) are all better than 0.99.

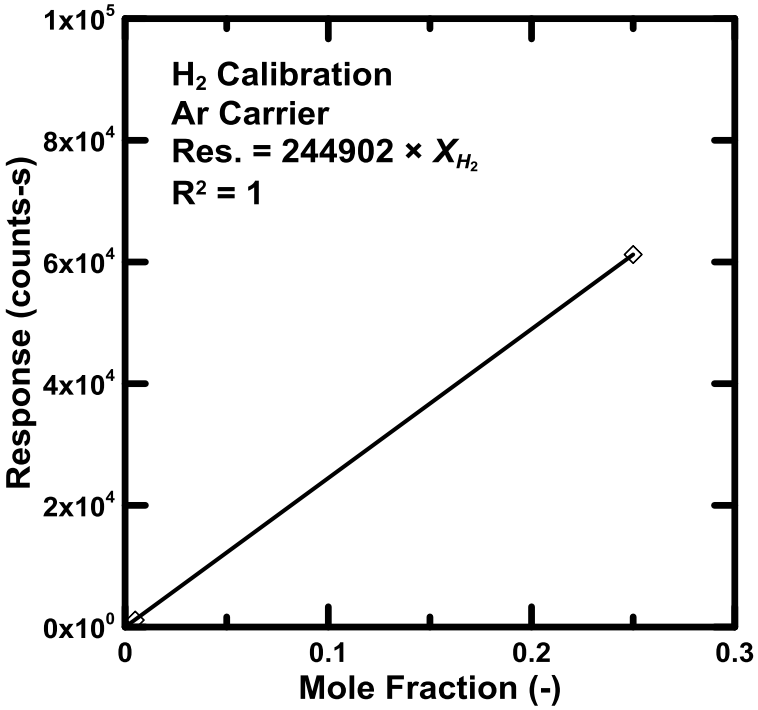

Figure E-1 Calibration curve for H_2.

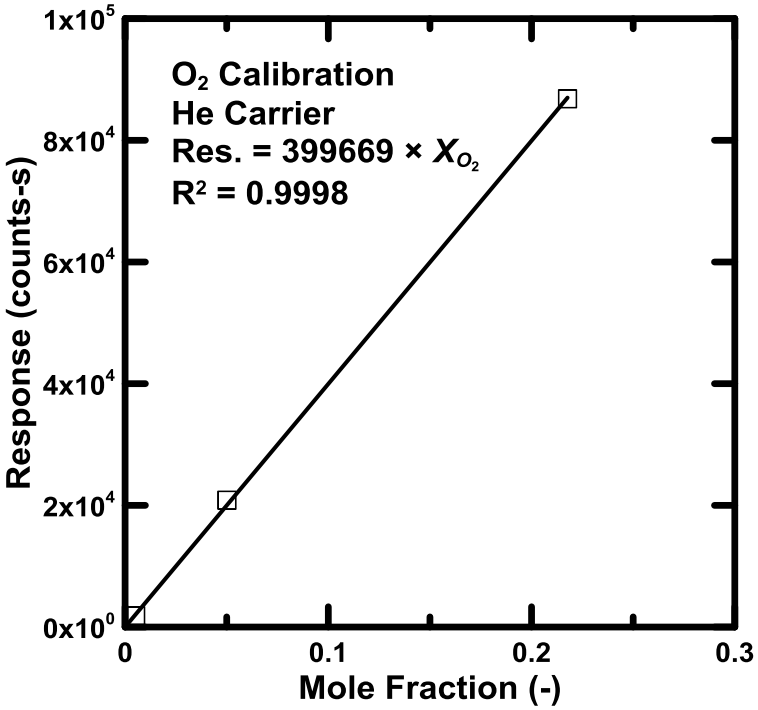

Figure E-2 Calibration curve for O_2.

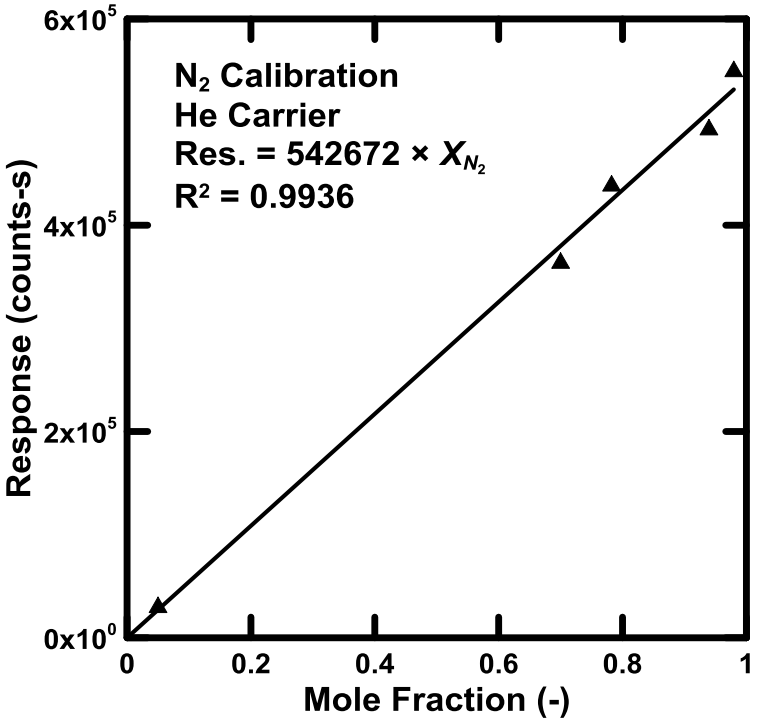

Figure E-3 Calibration curve for N_2.

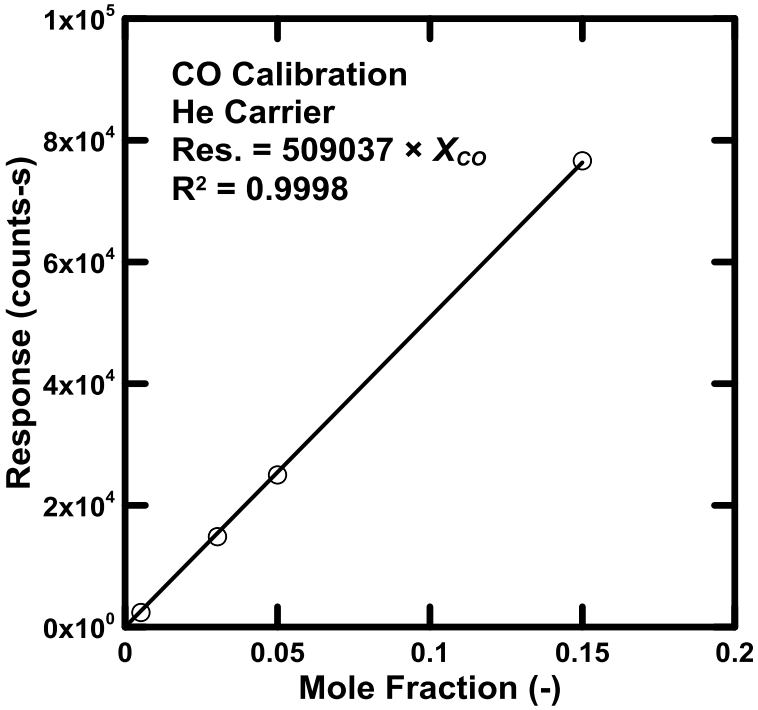

Figure E-4 Calibration curve for CO.

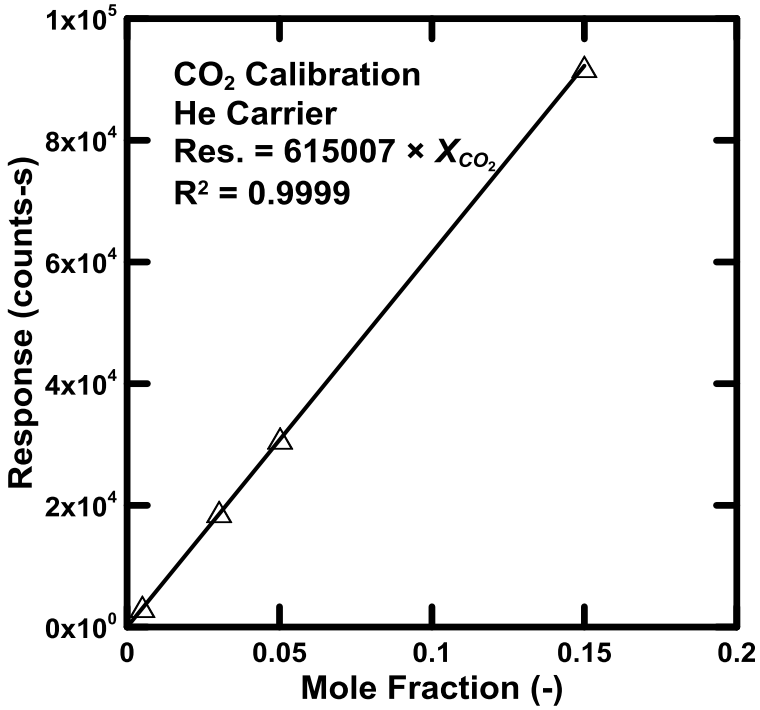

Figure E-5 Calibration curve for CO_2.

Appendix F. Equilibrium Constant

Equilibrium constants for radical (OH, O, and H) calculation in Eqs (5-8) – (5-10), Eqs. (5-13) – (5-15), and Eqs. (5-19) – (5-21) are summarized in Figs. F-1 – F-3.

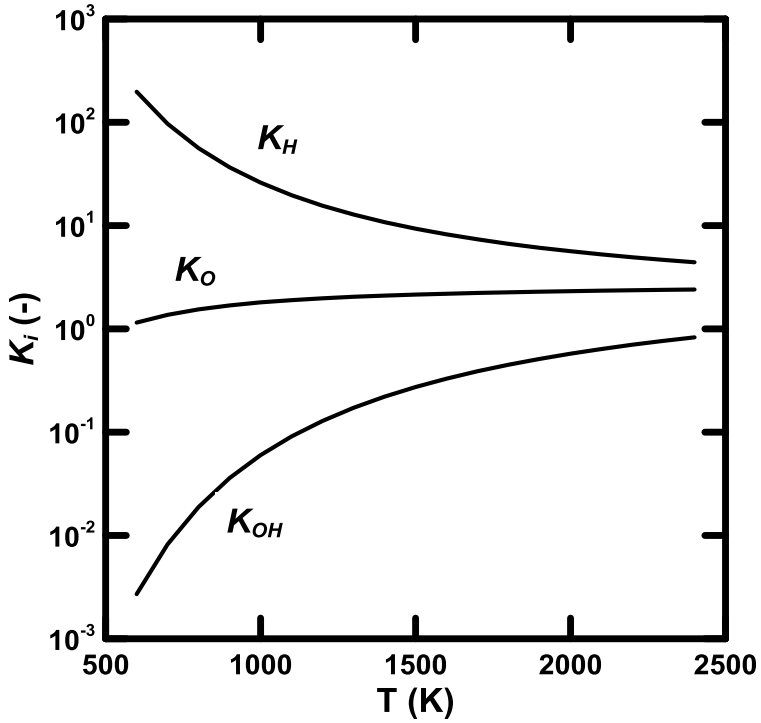

Figure F-1 Equilibrium constants for the three-reaction partial equilibrium.

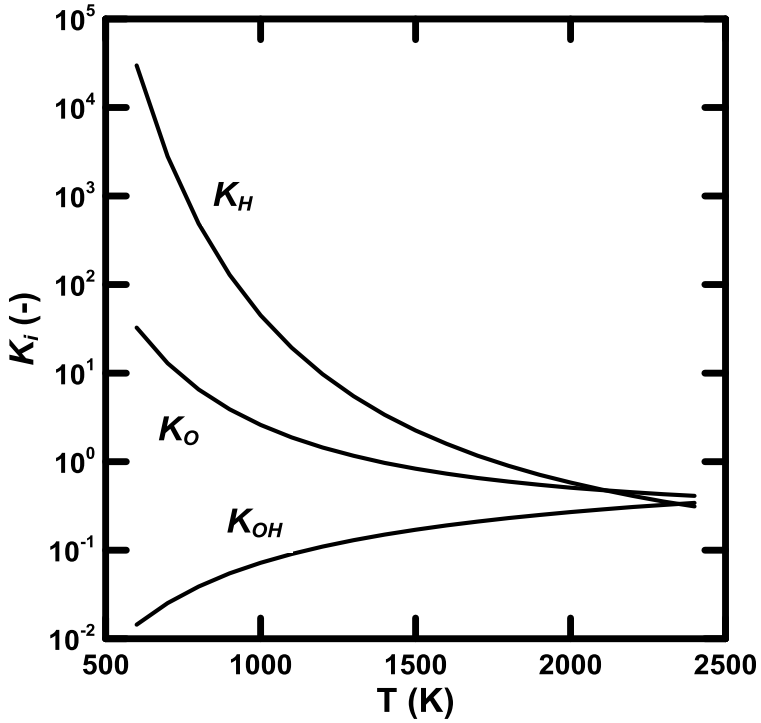

Figure F-2 Equilibrium constants for the four-reaction partial equilibrium.

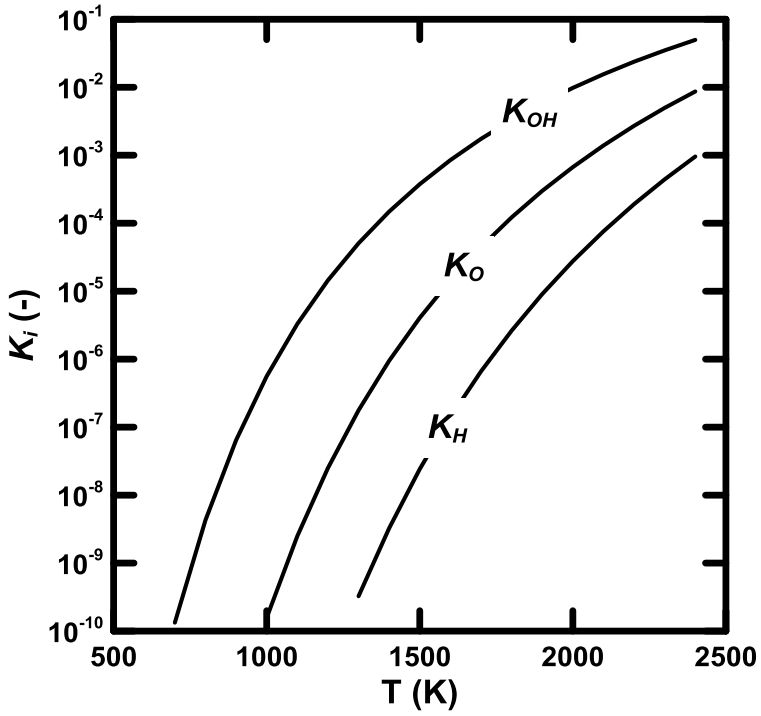

Figure F-3 Equilibrium constants for the catalyzed partial equilibrium.

Appendix G. Dependence of Image Intensity on Object Distance

Incident intensity on the camera sensor (image intensity) depends on the object distance. With the increase of object distance, the incident intensity per pixel also changes following two competing mechanisms: 1, reduced overall irradiance due to a reduced solid angle; 2, increased intensity due to a decreased image area. The resulting overall dependence was analytically discussed and confirmed with a blackbody furnace. This analysis provides useful information for large scale flames where flame size scale is comparable to the object distance, or flame conditions using the same calibration results, but with different objective distances. The analysis and test were all based on a blackbody source for simplicity.

The distance between the camera lens and the blackbody is assumed to be much larger than the blackbody aperture, the energy received by and passing through the camera lens aperture in the duration of t is:

$$e = \frac{EtA_l}{l_o^2} \ , \tag{G-1}$$

where A_l is the area of lens aperture, e is incident energy passing through the camera lens aperture, E is the total power emitted from the blackbody aperture, l_o is object distance, and t is shutter time.

The grayscales detected at the image area will be:

$$\mathrm{GS} = \frac{4K_C EtA_l}{\pi D_i^2 l_o^2} \ , \tag{G-2}$$

where D_i is the diameter of image, and K_c is a conversion coefficient of the detector. The diameter of the image can be related to the diameter of the blackbody aperture using the following equation:

$$D_i = D_k l_i / l_o \ , \tag{G-3}$$

where D_k is the blackbody aperture diameter, and l_i is image distance. The image distance is related to the object distance by following:

$$\frac{1}{l_i} = \frac{1}{l_f} - \frac{1}{l_o} \ , \tag{G-4}$$

where l_f is focal length of the lens. Combining Eqs. (G-2) – (G-4), and rearranging yields:

$$\mathrm{GS} = A_D \left(\frac{1}{l_f} - \frac{1}{l_o} \right)^2 \ , \tag{G-5}$$

where A_D is a combined factor counting for constants and coefficients.

A blackbody test was performed with a fixed focal length of 50 mm without extension ring. GS was plotted against the object distance, as shown in Fig. G-1. Also shown are the calculated results with an appropriately adjusted A_D. The image intensity increases with the object distance. For the current selected lens, image intensity becomes insensitive to the object lens after 200 cm. However, the image size also becomes small. The findings suggest that, for the current optical setup, any fine tune of the object distance requests a new blackbody calibration. For large scale flames, the sensitivity of intensity to flame scale needs to be validated and corrected.

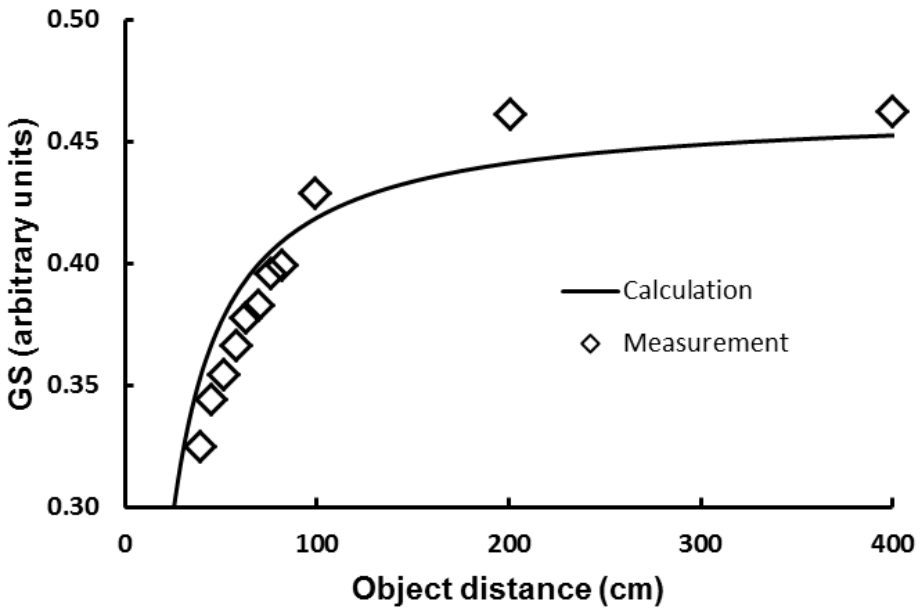

Figure G-1 Sensitivity of the image intensity to the object distance for a *f*/50 camera lens.

Appendix H. Main Script for optimization

```
DATA=load('FIT.txt');
z=DATA(:,1);% height
w_meas=DATA(:,2); % measured rate
C_O2=DATA(:,3); % concentration of O2 (mol/m^3)
u_O2=DATA(:,4); % velocity of O2 (m/s)
C_OH=DATA(:,5); % concentration of OH (mol/m^3)
u_OH=DATA(:,6); % velocity of OH (m/s)
T=DATA(:,7); % temperature (K)

pr1min=0.1; % OH A range
pr1max=0.3;
del1=0.01;
pr2min=3e6; % O2 A range
pr2max=3e7;
del2=1e5;
pr3min=1e5; % O2 E range
pr3max=3e5;
del3=1000;

A_OH=pr1min:del1:pr1max; % collision efficiency of OH
A_O2=pr2min:del2:pr2max; % factor of O2
E_O2=pr3min:del3:pr3max;% activation energy of O2
L=length(z);
L_OH=length(A_OH);
L_A_O2=length(A_O2);
L_E_O2=length(E_O2);
w_OH=(u_OH.*C_OH)*A_OH; % rate due to OH
EE_O2=zeros(L,L_E_O2);
for i=1:L
   EE_O2(i,:)=E_O2(:);
end
TT=zeros(L,L_E_O2);
UC=zeros(L,L_E_O2);
for i=1:L_E_O2
   TT(:,i)=T(:);
   UC(:,i)=u_O2.*C_O2;
end
EXPO=exp(-EE_O2/8.314./TT);

KK_O2=(EXPO.*UC); % rate due to O2
KKK_O2=zeros(L,L_E_O2,L_A_O2);
AAA_O2=zeros(L,L_E_O2,L_A_O2);
```

```
for i=1:L_A_O2
   KKK_O2(:,:,i)=KK_O2;
end

for i=1:L
  for j=1:L_E_O2
      AAA_O2(i,j,:)=A_O2;
  end
end

w_O2=AAA_O2.*KKK_O2; % w_O2=[O2]*u*A*exp(-E/RT)

R2=zeros(L_OH,L_E_O2,L_A_O2);
LOG_ft=log10(w_meas); % fit y=x
for i=1:L_OH
   for j=1:L_E_O2
      for k=1:L_A_O2
         pred=w_OH(:,i)+w_O2(:,j,k);
         LOG_y=log10(pred);
         y_bar=mean(LOG_y);
         SS_tot=sum((LOG_y-y_bar).^2);
         SS_res=sum((LOG_y-LOG_ft).^2);
         R2(i,j,k)=1-SS_res./SS_tot;
      end

   end
end
[row,col,vec] = ind2sub(size(R2),find(R2 == max(R2(:))));
MAX=max(R2(:));

AF_OH=A_OH(row);
EF_O2=E_O2(col);
AF_O2=A_O2(vec);
W_O2=(u_O2.*C_O2)*AF_O2.*exp(-EF_O2/8.314./T);
W_OH=(u_OH.*C_OH)*AF_OH;
W_pred=W_O2+W_OH;
```

Bibliography

[1] K.M. Leung, R.P. Lindstedt, and W.P. Jones, "A simplified reaction mechanism for soot formation in nonpremixed flames," Combust. Flame 87, 289-305 (1991).

[2] Kazakov, H. Wang, and M. Frenklach, "Detailed modeling of soot formation in laminar premixed ethylene flames at a pressure of 10 bar," Combust. Flame 100, 111-120 (1995).

[3] J. Appel, H. Bockhorn, and M. Frenklach, "Kinetic modeling of soot formation with detailed chemistry and physics: laminar premixed flames of C2 hydrocarbons," Combust. Flame 121, 122-136 (2000).

[4] F. Liu, H. Guo, G.J. Smallwood, and O.L. Gulder, "Numerical modelling of soot formation and oxidation in laminar coflow non-smoking and smoking ethylene diffusion flames," Combust. Theor. Model. 7, 301-315 (2003).

[5] R.S. Mehta, D.C. Haworth, and M.F. Modest, "An assessment of gas-phase reaction mechanisms and soot models for laminar atmospheric-pressure ethylene-air flames," Proc. Combust. Inst. 32, 1327-1334 (2009).

[6] J.S. Bhatt, and R.P. Lindstedt, "Analysis of the impact of agglomeration and surface chemistry models on soot formation and oxidation," Proc. Combust. Inst. 32, 713-720 (2009).

[7] M.S. Celnik, M. Sander, A. Raj, R.H. West, and M. Kraft, "Modelling soot formation in a premixed flame using an aromatic-site soot model and an improved oxidation rate," Proc. Combust. Inst. 32, 639-646 (2009).

[8] J.B. Howard, "Carbon addition and oxidation reactions in heterogeneous combustion and soot formation," Proc. Combust. Inst. 23, 1107-1127 (1990).

[9] I.M. Kennedy, "Models of soot formation and oxidation," Prog. Energy Combust. Sci. 23, 95-132 (1997).

[10] B.R. Stanmore, J.F. Brilhac, and P. Gilot, "The oxidation of soot: a review of experiments, mechanisms and models," Carbon 39, 2247-2268 (2001).

[11] J. Nagle, and R.F. Strickland-Constable, "Oxidation of carbon between 1000 C and 2000 C," in Proceedings of the Fifth Conference on Carbon, (Pergamon Press1962), pp. 154-164.

[12] K.G. Neoh, "Soot burnout in flames," Ph.D. Thesis, in Department of Chemistry (M.I.T, 1980).

[13] K.G. Neoh, J.B. Howard, and A.F. Sarofim, "Soot oxidation in flames," in Particulate Carbon, Formation during Combustion, D.C. Siegla, and G.W. Smith, eds. (Plenum Press, 1981), pp. 261-282.

[14] K.G. Neoh, J.B. Howard, and A.F. Sarofim, "Effect of oxidation on the physical structure of soot," Proc. Combust. Inst. 20, 951-957 (1984).

[15] R. Puri, R.J. Santoro, and K.C. Smyth, "The oxidation of soot and carbon monoxide in hydrocarbon diffusion flames," Combust. Flame 97, 125-144 (1994).

[16] R. Puri, R.J. Santoro, and K.C. Smyth, "Erratum," Combust. Flame 102, 226-228 (1995).

[17] C.A. Echavarria, I.C. Jaramillo, A.F. Sarofim, and J.S. Lighty, "Studies of soot oxidation and fragmentation in a two-stage burner under fuel-lean and fuel-rich conditions," Proc. Combust. Inst. 33, 659-666 (2011).

[18] C. Park, and J.P. Appleton, "Shock-tube measurements of soot oxidation rates," Combust. Flame 20, 369-379 (1973).

[19] K.B. Lee, M.W. Thring, and J.M. Beer, "On the rate of combustion of soot in a laminar soot flame," Combust. Flame 6, 137-145 (1962).

[20] M.L. Chan, K.N. Moody, J.R. Mullins, and A. Williams, "Low-temperature oxidation of soot," Fuel 66, 1694-1698 (1987).

[21] K.J. Higgins, H. Jung, D.B. Kittelson, J.T. Roberts, and M.R. Zachariah, "Size-selected nanoparticle chemistry kinetics of soot oxidation," J. Phys. Chem. A 106, 96-103 (2002).

[22] J. Camacho, Y. Tao, and H. Wang, "Kinetics of nascent soot oxidation by molecular oxygen in a flow reactor," Proc. Combust. Inst. 35, 1887-1894 (2015).

[23] J.P. Cain, P.L. Gassman, H. Wang, and A. Laskin, "Micro-FTIR study of soot chemical composition-evidence of aliphatic hydrocarbons on nascent soot surfaces," Phys. Chem. Chem. Phys. 12, 5206-5218 (2010).

[24] I.C. Jaramillo, C.K. Gaddam, R.L. Vander Wal, C.-H. Huang, J.D. Levinthal, and J.S. Lighty, "Soot oxidation kinetics under pressurized conditions," Combust. Flame (2014).

[25] Y. Zhang, and A.L. Boehman, "Oxidation behavior of soot generated from the combustion of methyl 2-butenoate in a co-flow diffusion flame," Combust. Flame 160, 112-119 (2013).

[26] A. Raj, S.Y. Yang, D. Cha, R. Tayouo, and S.H. Chung, "Structural effects on the oxidation of soot particles by O2: Experimental and theoretical study," Combust. Flame 160, 1812-1826 (2013).

[27] A. Raj, R. Tayouo, D. Cha, L. Li, M.A. Ismail, and S.H. Chung, "Thermal fragmentation and deactivation of combustion-generated soot particles," Combust. Flame 161, 2446-2457 (2014).

[28] M. Kalogirou, and Z. Samaras, "Soot oxidation kinetics from TG experiments," J. Therm. Anal. and Calorim. 99, 1005-1010 (2010).

[29] H.N. Sharma, L. Pahalagedara, A. Joshi, S.L. Suib, and A.B. Mhadeshwar, "Experimental study of carbon black and diesel engine soot oxidation kinetics using thermogravimetric analysis," Energy Fuel. 26, 5613-5625 (2012).

[30] C.P. Fenimore, and G.W. Jones, "Oxidation of soot by hydroxyl radicals," J. Phys. Chem. 71, 593-597 (1967).

[31] C.A. Echavarria, I.C. Jaramillo, A.F. Sarofim, and J.S. Lighty, "Burnout of soot particles in a two-stage burner with a JP-8 surrogate fuel," Combust. Flame 159, 2441-2448 (2012).

[32] D.E. Rosner, and H.D. Allendorf, "Comparative studies of the attack of pyrolytic and isotropic graphite by atomic and molecular oxygen at high temperatures," AIAA Journal 6, 650-654 (1968).

[33] F.J. Wright, "The oxidation of soot by O atoms," Proc. Combust. Inst. 15, 1449-1460 (1975).

[34] F. Xu, A.M. El-Leathy, C.H. Kim, and G.M. Faeth, "Soot surface oxidation in hydrocarbon/air diffusion flames at atmospheric pressure," Combust. Flame 132, 43-57 (2003).

[35] P.A. Tesner, and A.M. Tsibulevsky, "Kinetics of dispersed carbon gasification in diffusion flames of hydrocarbons," Combust. Flame 11, 227-233 (1967).

[36] C.Y. Wen, and T.Z. Chaung, "Entrainment coal gasification modeling," Ind. Eng. Chem. Process Des. Dev. 18, 684-695 (1979).

[37] P.A. Libby, and T.R. Blake, "Burning carbon particles in the presence of water vapor," Combust. Flame 41, 123-147 (1981).

[38] P.B. Sunderland, "Soot formation in laminar jet diffusion flames," Ph.D. Thesis, in Aerospace Engineering (The University of Michigan, 1995).

[39] A. Garo, G. Prado, and J. Lahaye, "Chemical aspects of soot particles oxidation in a laminar methane-air diffusion flame," Combust. Flame 79, 226-233 (1990).

[40] C.H. Kim, A.M. El-Leathy, F. Xu, and G.M. Faeth, "Soot surface growth and oxidation in laminar diffusion flames at pressures of 0.1-1.0 atm," Combust. Flame 136, 191-207 (2004).

[41] C.H. Kim, F. Xu, and G.M. Faeth, "Soot surface growth and oxidation at pressures up to 8.0 atm in laminar nonpremixed and partially premixed flames," Combust. Flame 152, 301-316 (2008).

[42] M. Frenklach, and H. Wang, "Detailed modeling of soot particle nucleation and growth," Proc. Combust. Inst. 23, 1559-1566 (1990).

[43] M.B. Colket, and R.J. Hall, "Successes and uncertainties in modeling soot formation in laminar, premixed flames," in Soot formation in combustion, H. Bockhorn, ed. (Springer-Verlag, 1994), pp. 442-469.

[44] C.-Y. Lin, and M.C. Lin, "Kinetics of the C6H5 + O2 reaction," presented at the Eastern States Section of the Combustion Institute Fall Technical Meeting, Gaithersburg, MD, USA 1987.

[45] B.C. Connelly, M.B. Long, M.D. Smooke, R.J. Hall, and M.B. Colket, "Computational and experimental investigation of the interaction of soot and NO in coflow diffusion flames," Proc. Combust. Inst. 32, 777-784 (2009).

[46] P. Roth, O. Brandt, and S. Von Gersum, "High temperature oxidation of suspended soot particles verified by CO and CO2 measurements," Proc. Combust. Inst. 23, 1485-1491 (1990).

[47] P.B. Sunderland, U.O. Koylu, and G.M. Faeth, "Soot formation in weakly buoyant acetylene-fueled laminar jet diffusion flames burning in air," Combust. Flame 100, 310-322 (1995).

[48] P.B. Sunderland, and G.M. Faeth, "Soot formation in hydrocarbon/air laminar jet diffusion flames," Combust. Flame 105, 132-146 (1996).

[49] F. Xu, P.B. Sunderland, and G.M. Faeth, "Soot formation in laminar premixed ethylene/air flames at atmospheric pressure," Combust. Flame 108, 471-493 (1997).

[50] R.J. Santoro, H.G. Semerjian, and R.A. Dobbins, "Soot particle measurements in diffusion flames," Combust. Flame 51, 203-218 (1983).

[51] H.I. Joo, and O.L. Gulder, "Soot formation and temperature field structure in co-flow laminar methane air diffusion flames at pressures from 10 to 60 atm," Proc. Combust. Inst. 32, 769-775 (2009).

[52] P.M. Mandatori, and O.L. Gulder, "Soot formation in laminar ethane diffusion flames at pressures from 0.2 to 3.3 MPa," Proc. Combust. Inst. 33, 577-584 (2011).

[53] D. Snelling, K. Thomson, G. Smallwood, O. Gulder, E. Weckman, and R. Fraser, "Spectrally resolved measurement of flame radiation to determine soot temperature and concentration," AIAA Journal 40, 1789-1795 (2002).

[54] F.J. Diez, C. Aalburg, P.B. Sunderland, D.L. Urban, Z.G. Yuan, and G.M. Faeth, "Soot properties of laminar jet diffusion flames in microgravity," Combust. Flame 156, 1514-1524 (2009).

[55] D.L. Urban, Z.G. Yuan, P.B. Sunderland, G.T. Linteris, J.E. Voss, K.C. Lin, Z. Dai, K. Sun, and G.M. Faeth, "Structure and soot properties of nonbuoyant ethylene/air laminar jet diffusion flames," AIAA Journal 36, 1346-1360 (1998).

[56] B.B. Connelly, S.A. Kaiser, M.D. Smooke, and M.B. Long, "Two-dimensional soot pyrometry with a color digital camera," presented at the Eastern States Section of the Combustion Institute Spring Technical Meeting, Philadelphia, PA, USA 2005.

[57] P.B. Kuhn, B. Ma, B.C. Connelly, M.D. Smooke, and M.B. Long, "Soot and thin-filament pyrometry using a color digital camera," Proc. Combust. Inst. 33, 743-750 (2011).

[58] T. Fu, X. Cheng, and Z. Yang, "Theoretical evaluation of measurement uncertainties of two-color pyrometry applied to optical diagnostics," Appl. Opt. 47, 6112-6123 (2008).

[59] S. De Iuliis, M. Barbini, S. Benecchi, F. Cignoli, and G. Zizak, "Determination of the soot volume fraction in an ethylene diffusion flame by multiwavelength analysis of soot radiation," Combust. Flame 115, 253-261 (1998).

[60] Y. Matsui, T. Kamimoto, and S. Matsuoka, "A study on the time and space resolved measurement of flame temperature and soot concentration in a D.I.Diesel engine by the two color method," SAE Transaction 88, 1808-1822 (1979).

[61] R.J. Santoro, T.T. Yeh, J.J. Horvath, and H.G. Semerjian, "The transport and growth of soot particles in laminar diffusion flames," Combust. Sci. Tech. 53, 89 - 115 (1987).

[62] P.S. Greenberg, and J.C. Ku, "Soot volume fraction imaging," Appl. Opt. 36, 5514-5522 (1997).

[63] C.P. Arana, M. Pontoni, S. Sen, and I.K. Puri, "Field measurements of soot volume fractions in laminar partially premixed coflow ethylene/air flames," Combust. Flame 138, 362-372 (2004).

[64] D.R. Snelling, K.A. Thomson, G.J. Smallwood, and O.L. Guder, "Two-dimensional imaging of soot volume fraction in laminar diffusion flames," Appl. Opt. 38, 2478-2485 (1999).

[65] J.D. Maun, P.B. Sunderland, and D.L. Urban, "Thin-filament pyrometry with a digital still camera," Appl. Opt. 46, 483-488 (2007).

[66] D. Coffin, "Decoding raw digital photos in Linux," http://www.cybercom.net/~dcoffin/dcraw/, accessed 2/1/2015.

[67] P. Elder, T. Jerrick, and J.W. Birkeland, "Determination of the radial profile of absorption and emission coefficients and temperature in cylindrically symmetric sources with self-absorption," Appl. Opt. 4, 589-592 (1965).

[68] S.J. Young, "Iterative Abel inversion of optically thick, cylindrically symmetric radiation sources," J. Quant. Spectrosc. Radiat. Transf. 25, 479-481 (1981).

[69] Y. Wang, P. Ding, and Y. Mu, "A spline approximation of the Abel transformation for use in optically-thick, cylindrically-symmetric plasmas," J. Quant. Spectrosc. Radiat. Transf. 54, 1055-1058 (1995).

[70] Z.G. Yuan, "The filtered Abel transform and its application in combustion diagnostics," presented at the Western States Section of the Combustion Institute Fall Technical Meeting, Stanford, CA, USA 1995.

[71] R. Starke, B. Kock, and P. Roth, "Nano-particle sizing by laser-induced-incandescence (LII) in a shock wave reactor," Shock Waves 12, 351-360 (2003).

[72] D. Allen, H. Krier, and N. Glumac, "Heat transfer effects in nano-aluminum combustion at high temperatures," Combust. Flame 161, 295-302 (2014).

[73] W.H. Dalzell, G.C. Williams, and H.C. Hottel, "A light-scattering method for soot concentration measurements," Combust. Flame 14, 161-169 (1970).

[74] K.C. Smyth, and C.R. Shaddix, "The elusive history of for the refractive index of soot," Combust. Flame 107, 314-320 (1996).

[75] S.C. Lee, and C.L. Tien, "Optical constants of soot in hydrocarbon flames," Symposium (International) on Combustion 18, 1159-1166 (1981).

[76] D. Liu, Q.X. Huang, F. Wang, Y. Chi, K.F. Cen, and J.H. Yan, "Simultaneous measurement of three-dimensional soot temperature and volume fraction fields in axisymmetric or asymmetric small unconfined flames with CCD cameras," J. Heat Transf. 132, 061202 (2010).

[77] H. Guo, J.A. Castillo, and P.B. Sunderland, "Digital camera measurements of soot temperature and soot volume fraction in axisymmetric flames," Appl. Opt. 52, 8040-8047 (2013).

[78] R.A. Dobbins, and C.M. Megaridis, "Morphology of flame-generated soot as determined by thermophoretic sampling," Langmuir 3, 254-259 (1987).

[79] U.O. Koylu, and G.M. Faeth, "Structure of overfire soot in buoyant turbulent diffusion flames at long residence times," Combust. Flame 89, 140-156 (1992).

[80] I. Grishin, K. Thomson, F. Migliorini, and J.J. Sloan, "Application of the Hough transform for the automatic determination of soot aggregate morphology," Appl. Opt. 51, 610-620 (2012).

[81] R.L. Vander Wal, V. Pushkarev, and J.H. Fujiyama-Novak, "Fire signatures of spacecraft materials: Gases and particulates," Combust. Flame 159, 897-904 (2012).

[82] R. Puri, and R.J. Santoro, "The role of soot particle formation on the production of carbon monoxide in fires," presented at the Fire Safety Science - Proceedings of the Third International Symposium (1991), pp. 595-604.

[83] R.E. Mitchell, A.F. Sarofim, and L.A. Clomburg, "Partial equilibrium in the reaction zone of methane-air diffusion flames," Combust. Flame 37, 201-206 (1980).

[84] K.C. Smyth, P.J.H. Tjossem, A. Hamins, and J.H. Miller, "Concentration measurements of OH and equilibrium analysis in a laminar methane-air diffusion flame," Combust. Flame 79, 366-380 (1990).

[85] T.S. Cheng, C.Y. Wu, C.P. Chen, Y.H. Li, Y.C. Chao, T. Yuan, and T.S. Leu, "Detailed measurement and assessment of laminar hydrogen jet diffusion flames," Combust. Flame 146, 268-282 (2006).

[86] T. Aizawa, "Diode-laser wavelength-modulation absorption spectroscopy for quantitative in situ measurements of temperature and OH radical concentration in combustion gases," Appl. Opt. 40, 4894-4903 (2001).

[87] T.N. Anderson, R.P. Lucht, T.R. Meyer, S. Roy, and J.R. Gord, "Diode-laser-based ultraviolet-absorption sensor for high-speed detection of the hydroxyl radical," Opt. Lett. 30, 1321-1323 (2005).

[88] R.E. Mitchell, "Nitrogen oxide formation in laminar methane-air diffusion flames," Ph.D. Thesis, in Department of Chemical Engineering (M.I.T, 1975).

[89] W.C. Reynolds, "The element potential method for chemical equilibrium analysis: implementation in the interactive program STANJAN " (Department of Mechanical Engineering, Stanford University, 1986).

[90] R.J. Kee, F.M. Rupley, and J.A. Miller, "CHEMKIN," (Reaction Design, Inc., 2014).

[91] M.F.R. Mulcahy, and B.C. Young, "The reaction of hydroxyl radicals with carbon at 298 K," Carbon 13, 115-124 (1975).

[92] M.W. Chase, C.A. Davies, J.R. Downey, D.J. Frurip, R.A. McDonald, and A.N. Syverud, "NIST JANAF Thermochemical Tables ver. 1.0," (1985).

[93] A.L. Sanchez, A. Limnan, and F.A. Williams, "A generalized Burke-Schumann formulation for hydrogen-oxygen diffusion flames maintaining partial equilibrium of the shuffle reactions," Combust. Sci. Tech. 123, 317-345 (1997).

[94] I.W. Smith, "The combustion rates of coal chars: A review," Proc. Combust. Inst. 19, 1045-1065 (1982).

[95] H. Guo, "Soot oxidation in hydrocarbon-free flames," Ph.D. Thesis, in Department of Mechanical Engineering (The University of Maryland, 2015).

[96] A.D.H. Clague, J.B. Donnet, T.K. Wang, and J.C.M. Peng, "A comparison of diesel engine soot with carbon black1," Carbon 37, 1553-1565 (1999).

[97] R. Puri, T.F. Richardson, R.J. Santoro, and R.A. Dobbins, "Aerosol dynamic processes of soot aggregates in a laminar ethene diffusion flame," Combust. Flame 92, 320-333 (1993).

[98] P.J. Davis, and P. Rabinowitz, Methods of numerical integration (Academic Press, 1975).

[99] B.J. Hughey, and D.A. Santavicca, "A comparison of techniques for reconstructing axisymmetric reacting flow fields from absorption measurements," Combust. Sci. Tech. 29, 167-190 (1982).

[100] M.M. Khan, and J.L. De Ris, "Operator independent ignition measurements," presented at the Fire Safety Science - Proceedings of the Eighth International Symposium (2005), pp. 163-174.